LASER THERMAL PROCESSING OF NOVEL DOPING SCHEMES IN SILICON

By

MARK H. CLARK

A DISSERTATION PRESENTED TO THE GRADUATE SCHOOL
OF THE UNIVERSITY OF FLORIDA IN PARTIAL FULFILLMENT
OF THE REQUIREMENTS FOR THE DEGREE OF
DOCTOR OF PHILOSOPHY

UNIVERSITY OF FLORIDA

2004

This document is dedicated to Jennifer B. Clark.

ACKNOWLEDGMENTS

Several individuals have provided support and guidance that contributed to the completion of the work within this dissertation. I would like to thank my advisor, Dr. Kevin Jones, for his guidance and patience throughout the duration of this work. I must also thank my cochairman, Dr. Mark Law, for the direction he has provided and his willingness to answer my questions. I am also grateful for the pleasant work environment and the caliber of students they have brought together to create the SWAMP Center. I would also like to thank Dr. Paul Holloway, Dr. Robert DeHoff and Dr. David Norton for their participation on my supervisory committee.

Financial support for this research was provided by the Semiconductor Research Council (SRC). Many individuals contributed to the completion of this work. I am appreciative to Somit Talwar for allowing access to the laser annealing tools at Verdant Technologies and to fellow graduate student Kevin Gable for performing the laser anneals. I would also like to thank Prof. Mike Thompson and Shenzhi Yang of Cornell University for their assistance with initial laser annealing. Additionally, I would like to thank Valentin Craciun of the Major Analytical Instrument Center at the University of Florida for his expertise and assistance in performing high resolution x-ray diffraction, and Mikhail Klimov of the University of Central Florida for performing secondary ion mass spectrometry analysis. Finally, I would like to thank the students within the SWAMP Center for providing the day-to-day support and interaction that made graduate school enjoyable. Of course I never would have gone to college had it not been for the

love and support of my parents, Raoel and Janet Clark. Lastly, I will forever be indebted to my wife and best friend, Jennifer. Without her support and encouragement, I would not have completed this work.

TABLE OF CONTENTS

Page

LIST OF TABLES

LIST OF FIGURES

Abstract of Dissertation Presented to the Graduate School
of the University of Florida in Partial Fulfillment of the
Requirements for the Degree of Doctor of Philosophy

LASER THERMAL PROCESSING OF NOVEL DOPING SCHEMES IN SILICON

By

Mark H. Clark

May 2004

Chair: Kevin S. Jones
Major Department: Materials Science and Engineering

Future semiconductor technology nodes are not achievable with current processing technologies. Shrinking of device dimensions is limited by the ability to fabricate doped junctions that are shallow, abrupt and highly activated. In conventional processing, achieving high activation is at odds with achieving a shallow junction. High activation is generally achieved by high thermal budgets, which diffuse the dopant increasing the final junction depth. In contrast, a low thermal budget limits diffusion of the dopant but yields a low activation. Consequently, new processing techniques need to be developed which are capable of producing device features in compliance with the requirements of future technology nodes.

A potential candidate for reaching future technology nodes is laser thermal processing (LTP). Laser thermal processing offers several advantages over conventional processing techniques: 1) the junction depth is defined by the amorphous/crystalline interface, 2) the amorphous region is regrown by liquid phase epitaxy providing an even distribution of the dopant across that junction, resulting in a box like junction, 3) cooling

is rapid and regrowth is non-equilibrium so dopants can exceed solid solubility, thus producing high activation.

Traditionally, the choice of dopant has been limited to those species with the highest solid solubility. However, LTP is not fundamentally limited by solid solubility. Therefore, it is of interest to evaluate alternate dopants that have previously been excluded due to low equilibrium solid solubility. To this end, alternate dopants of ^{14}N, ^{121}Sb (n-type), ^{27}Al, ^{70}Ga, and ^{115}In (p-type) are compared to conventional dopants of ^{33}As and ^{5}B respectively, after LTP and post-LTP thermal anneals. Experimental results indicate that LTP of alternate dopants increases the active carrier concentrations of Al, Ga, In and Sb above equilibrium solid solubility.

Dopants activated by laser thermal processing above equilibrium solid solubility are metastable and deactivate during subsequent thermal anneals. It is therefore advantageous to reduce any factors that contribute to the deactivation. Specifically, substitutional incorporation of dopant atoms into the silicon lattice introduces an associated strain because the dopant atoms are not the same size as the silicon. For ^{5}B the strain is tensile, while for ^{115}In it is compressive. Co-implantation of ^{5}B and ^{115}In is investigated as a scheme to compensate the strain introduced to the lattice and potentially reduce deactivation of the supersaturated dopants during post-LTP annealing. Experimental results indicate that increasing the dose of co-implanted indium reduces the tensile strain introduced to the silicon lattice by boron. The compensation of strain correlates to a suppression of the sheet resistance measured after post-LTP annealing.

CHAPTER 1
INTRODUCTION

The objective of this document is to describe the electrical and physical characteristics of junctions formed by laser thermal processing of amorphous layers doped with novel dopant species and combinations of dopant species. Chapter 1 presents the motivation for the work by reviewing the trends in scaling and highlights the associated advantages of laser thermal processing. Chapter 2 describes the experimental matrices and explains the basic principles of the analytical techniques used for characterization. Chapter 3 presents the experimental results and discussion. Chapter 4 summarizes the experimental findings of the work. Chapter 5 presents the developmental models used to describe sub-melt laser thermal processing.

Motivation

Faster, smaller, lower cost-per-function electronic devices are made possible, primarily by reducing transistor size. The metal-oxide-semiconductor field-effect-transistor or MOSFET is the basic building block of electronic devices (Figure 1-1). Reducing the feature size of the MOSFET to fit more in the same planar area is termed scaling. Scaling supports the production of faster, smaller and less expensive electronic devices.

Drain Extension Scaling

Scaling requires junction engineering to minimize deleterious short channel effects and parasitic series resistances. A junction in the MOSFET that critically affects electrical performance is the drain extension. The drain extension collectively refers to

the source and drain extensions, which are physically identical. For the purpose of this text, the drain extension is a shallow junction that connects the channel with the deep drain as illustrated in Figure 1-1. Drain extensions are conventionally fabricated by low energy ion implantation, to introduce the dopant into the sample surface, followed by a thermal anneal to electrically activate the implanted dopant.

Increasing the lateral abruptness and decreasing the depth of drain extensions reduce short channel effects. Short channel effects diminish the ability of the gate to control the channel charge. To minimize short channel effects, drain extensions need to have laterally abrupt dopant gradients at the interface with the channel. Abruptness of the dopant gradient is quantified by the number of nanometers required to change one order of magnitude or decade in concentration. As the number of nanometers per decade decreases, the abruptness of the dopant gradient increases. For a fixed gate length, increasing the lateral abruptness of the drain extension reduces the encroachment of the depletion region from the extension into the channel, thus increasing the control of the gate over the channel charge [1]. Encroachment of the drain extension depletion region into the channel is also influenced by the depth of the junction, as illustrated in Figure 1-2. Depending on the transistor bias conditions, reducing the depth of the drain extension, increases the amount of the channel charge that is controlled by the gate [2]. Consequently, as the physical length of the gate is scaled down, it is necessary to increase the lateral abruptness and decrease the depth of the drain extension to maintain the same amount of gate control over the channel.

Drain extensions need to be abrupt and have a high concentration of electrical active dopants to reduce the extension contribution to parasitic resistance. Parasitic

resistance lowers the transistor drive current and increases the resistance/capacitance time delay, which reduce the performance of the device. Parasitic resistance is the series sum of the silicide contact resistance R_{cs}, the deep drain resistance R_{dd}, the drain extension resistance R_{de}, and the drain extension-to-gate overlap resistance R_{ov}, as illustrated in Figure 1-3. Increasing the concentration of electrically active dopants in the junction can reduce resistance of the drain extension. Additionally, theoretical analysis indicates that increased abruptness of the extension doping gradient reduces the extension contribution to parasitic resistance [3].

A fundamental trade-off of junction scaling is the inverse relationship between sheet resistance and junction depth. In physical terms, a deeper junction has a larger volume. Therefore, assuming a constant concentration, a deeper junction can incorporate a larger dose of electrically active carriers than a shallow junction. A larger active dose corresponds to a lower sheet resistance. Under equilibrium conditions, the maximum carrier concentration is determined by the dopant solid solubility limit. Hence, for equilibrium processes limited by solid solubility, a decrease in sheet resistance corresponds to an increase in junction depth, and vice versa.

Scaling Requirements

In 1965, based upon the trends of previous years, G. E. Moore forecast that the number of economically producible transistors per unit area would double approximately every year [4]. Over time, Moore's prediction proved to be qualitatively accurate, and is now commonly referred to as Moore's Law of scaling. A revised and detailed extension of Moore's Law is the International Technology Roadmap for Semiconductors (ITRS), which is a reference for scaling requirements, potential solutions, and their respective timing [5].

The 2002 ITRS predicts that continued device scaling beyond the year 2007 is limited by the inability of current processing technologies. Table 1-1 summarizes the 2002 ITRS scaling trends for MOSFET drain extensions. Numbers within dark gray cells of the table are requirements for which the processing solution is not known. For the 65 nm technology node, drain extensions require a junction depth between 10-17 nm, which, combined with the other extension requirements, is not achievable with conventional processing technologies. Additionally, by 2010 both sheet resistance and lateral abruptness of the drain extension will also exceed the limitations of conventional processing technologies. Hence, processing technologies capable of meeting these future requirements are needed.

Conventional Processing Technologies

Since the paper by Alväger and Hansen [6] in 1962, the doping of semiconductors by ion implantation has become an industry standard [7] by providing improved control of the dopant depth and concentration over that of classical solid source diffusion. A drawback to ion implantation is the damage created by the billiard ball type collisions of the implanted ions with those atoms composing the crystalline substrate. Conventionally, the crystallinity of the implanted layer is restored and the dopant atoms electrically activated by a rapid thermal anneal (RTA). As device dimensions continue to scale down in size there is a necessity of obtaining shallow junction regions with low sheet resistance. However, the process of ion implantation followed by rapid thermal annealing is limited by solid solubility and transient enhanced diffusion (TED) [8-10]. Specifically, the thermal budget of the rapid thermal anneal coupled with the damage introduced by ion implantation produces a transient enhanced diffusion of the dopant [11], which results in a deeper junction with degraded abruptness. Additionally, the

concentration of the dopant that can be incorporated into the silicon lattice is limited by equilibrium solid solubility, thus imposing a barrier to reducing the sheet resistance for a fixed junction depth. Hence, activation of ion implanted dopants by conventional rapid thermal annealing is limited by solid solubility, while the junction depth is increased by enhanced diffusion.

Future Processing Technologies

Solid phase epitaxy regrowth, Vortek flash annealing, Levitor annealing and laser thermal annealing are processing technologies that are being developed to meet drain extension scaling requirements. Solid phase epitaxy regrowth (SPER) involves an amorphous layer in intimate contact with a crystalline layer; when heated to a sufficient temperature, the amorphous layer recrystallizes using the crystalline layer as a seed. Regrowth typically begins at temperatures as low as 400 to 450 ^{o}C [12] on up to temperatures below the melting point of amorphous silicon, with regrowth rates dramatically increasing as a function of increasing temperature. Flash annealing developed by Vortek Industries uses a continuous arc lamp to heat the bulk of the wafer to an intermediate temperature and then discharges a capacitor bank into flash lamps to add additional power that produces an ultra-high temperature anneal of the surface without heating the substrate by more than 50 ^{o}C over the intermediate temperature. The effective time for the flash cycle is approximately $1.0x10^{-3}$ s, allowing ramp-up rates of approximately $1.0x10^{6}$ °C/s, and maximum cool-down rates of 150 °C/s [13]. Levitor annealing developed by ASM uses a gas-bearing system to suspend the wafer between two high thermal mass blocks. Using conduction rather than radiation, the floating wafer is heated at rates up to 900 ºC/s [14]. Laser thermal processing (melt) uses laser

irradiation with pulse duration of approximately $1.0x10^{-9}$ s to melt an amorphous surface layer [15]. All four processing technologies are designed to optimize the thermal cycles to obtain high concentrations of electrically activate dopants while minimizing diffusion. The electrical activation and resulting diffusion for p-type dopants achieved by SPER, Vortek, Levitor and laser thermal processing are plotted in Figure 1-4, in terms of sheet resistance against junction depth. Boxes extending from the base line of the plot illustrate sheet resistance and junction depth requirements forecast for the 130, 90, 65, 45, 32 and 22 nm technology nodes [5]. All four processing technologies offer improvements over conventional rapid thermal annealing, achieving lower sheet resistance values at shallower junction depths. For the plotted data points, laser thermal processing achieves sheet resistance values below the maximum scaling requirements, thus providing a margin to decrease junction depth at the expense of increased sheet resistance while still satisfying the scaling requirements. In terms of junction abruptness laser thermal processing also offers an advantage. Figure 1-5 is a plot of junction abruptness as a function of processing technology [9].[1] Junction abruptness exhibits a trend with processing technology similar to that for sheet resistance and junction depth, with laser thermal processing and SPER achieving the most abrupt junctions.

Laser thermal processing is a processing technology that can potentially achieve the ITRS requirements forecast for drain extensions. Junction depths as shallow as 6 nm with a corresponding sheet resistance less than 400 ohms/sq have been achieved by laser

[1] For drain extensions it is lateral junction abruptness that is most critical. However, it is vertical abruptness that is measured by SIMS depth profiles. Therefore, due to the inability to measure lateral abruptness it is convention to report vertical abruptness under the assumption that the two are proportional. Additionally, achieving a junction abruptness of less than 2 nm/decade is limited by the ability to quantify below this value. The resolution of SIMS is also approximately 2 nm/decade.

thermal processing p-type dopants, thus demonstrating a concomitant decrease of sheet resistance and junction depth [16]. Additionally, laser thermal processing can achieve a junction abruptness of less than 2 nm/decade [17]. Based on sheet resistance, junction depth and abruptness data, laser thermal processing is a promising candidate for achieving the future drain extension scaling requirements predicted by the ITRS roadmap.

Laser Thermal Processing

Laser thermal processing (LTP) is a paradigm shift in the formation of shallow junctions in silicon. The sub-processes of LTP are amorphization, dopant implant, laser irradiation, liquid melt and liquid phase epitaxy. During laser irradiation the amorphous region is liquefied allowing the dopant atoms to distribute homogeneously throughout the melt by diffusion. Upon rapid solidification, the dopants largely retain the even distribution and produce an abrupt junction that is box shaped, with the depth of the junction defined by the position of the amorphizing implant. Additionally, due to rapid conductive cooling, the liquid phase epitaxy is non-equilibrium, resulting in the substitutional incorporation of the dopant atoms into the crystalline lattice in excess of equilibrium solid solubility.

Description

Since the invention of light amplification by stimulated emission of radiation or LASER in 1960, lasers have been used in a variety of ways to process semiconductors. From as early as 1968 lasers were used to modify the electrical resistivity of semiconductors [18]. By 1976 lasers were being used to remove lattice damage caused by ion-implantation and to electrically activate dopants in a process termed laser annealing [19]. In 1978 re-crystallization of an amorphous silicon film was achieved by

irradiation with a single laser pulse [20, 21]. More recently lasers have been used to melt doped amorphous layers to define the depth of electrically active junctions [15]. For the current text, the process of laser irradiating a doped amorphous layer to achieve full melt and subsequent epitaxial re-growth resulting in the depth of the electrical junction being defined by the original amorphous layer thickness is termed laser thermal processing. The following five sections further describe laser thermal processing in terms of amorphization, dopant implantation, laser irradiation, liquid melt and liquid phase epitaxy.

Amorphizing implant

Depth of the amorphous layer controls the depth of the melt. Implanting the substrate with a high dose of a low energy, high mass ion, forms a shallow amorphous layer. Amorphization is a result of the damage introduced to the crystalline lattice during ion implantation [22]. For crystalline silicon, amorphization requires displacement of approximately 10 – 12 % of the lattice atoms. Formation of an amorphous layer progresses gradually, as damage to the crystal lattice is accumulated with each ion that is implanted. The number of ions per unit area required to amorphize a layer is referred to as the threshold dose. Amorphizing implants must have an implant dose higher than the threshold dose. The threshold dose for an ion with low mass is larger than that for ions with a high mass. The depth of the amorphous layer is determined by the energy of the implant ion. Ions with low implant energy do not travel as deep into the substrate as high-energy implants; subsequently, low energy implants result in shallower amorphization depths.

Dopant implant

The dopant is implanted into the amorphous surface layer at a low energy and high dose. Implantation of the dopant is consistent with conventional ion implantation [23]. The implant energy of the dopant ions needs to be sufficiently low to confine the dopant to the amorphous layer, thus maintaining an electrical junction defined by the amorphous depth. Additionally, the dose of the dopant needs to be high in order to provide sufficient population of carriers to achieve a low sheet resistance.

Laser irradiation

Lasers provided a high-power-density energy source that is both monochromatic and coherent, which can be controlled to achieve nanosecond pulsed durations. For laser thermal processing several types of lasers have been used, differing primarily in wavelength (e.g., XeCl 308 [15, 16, 24], frequency doubled Nd-YAG 532 [25] and Nd-YAG 1064 nm). Wavelength of the laser affects the optical properties of the material, specifically reflectivity, absorption and absorbance. Reflectivity is the amount of incident energy that is reflected from the surface of the material relative to the incident intensity. Absorption determines degree to which the amplitude of the radiation is damped as a function of distance into the sample. Absorbance is the inverse of the penetration depth at which the intensity of the laser has decreased to 37 % of the original value. Laser wavelength can be chosen to alter the interaction with the sample material. For example, in crystalline silicon, laser wavelengths of 308 and 532 nm correspond to penetration depths of approximately 67 and 1000 Å, respectively. In contrast, crystalline silicon is effectively transparent at a wavelength of 1064 nm. As described in the experimental chapter, a 308 nm laser wavelength is used in the current study. The temporal distribution of the laser irradiation is a Gaussian shaped pulse. Duration of the

pulse is measured and reported as the full-width-half-maximum (FWHM) of the Gaussian distribution as illustrated in Figure 1-6.

Output from the 308 nm XeCl excimer laser is directed through optics that homogenize, focus and define the cross-sectional area of the laser irradiation. In the irradiated area of the sample, absorption of laser energy by the silicon may result in emission of phonons that are expressed as thermal heating [26]. Absorption occurs when a light quantum hits an electron and the electron absorbs the energy and as a consequence moves into a higher energy state. The electron can transition between energy bands by a direct transition or indirect transition. A direct transition produces a photon that is reflected, while an indirect transition produces a photon and a phonon. It is the phonon that produces the effect of heating. For amorphous silicon, the transition mechanism is predominately indirect, thus resulting in phonon induced lattice heating.

Liquid melt

Heating from the laser provides the thermal budget for melting, diffusion and electrical activation. Amorphous silicon melts at approximately 200 ± 50 K lower than that of the crystalline silicon [27]. Laser thermal processing utilizes this melting point difference to establish a process window. As the laser energy density is increased, a threshold is reached at which the amorphous silicon begins to melt. Further increase in the laser energy density increases the melt depth, until the entire amorphous layer is melted and the original amorphous/crystalline interface is reached. The melt does not proceed into the crystalline material until sufficient thermal energy is added to raise the liquefied amorphous silicon temperature to the melting point of crystalline silicon. The difference in laser energy density required to completely melt the amorphous layer and

the laser energy density required to begin melting the crystalline silicon is termed the process window [25].

Dopants distribute homogeneously throughout the liquid melt. The diffusion coefficient of dopant atoms in liquid silicon is approximately eight orders of magnitude greater than in crystalline silicon. For example the diffusion coefficient of boron in liquid silicon is $3.3 \pm 0.4 \times 10^{-4}$ cm^2/s [28], while the diffusion coefficient in crystalline silicon is approximately 1.0×10^{-15} cm^2/s. The large diffusivity of the dopant atoms in the liquid region results in a rapid redistribution that tends to homogenize the dopant distribution throughout the melt. In contrast, the amount of diffusion that occurs in the solid is negligible in comparison; thus in terms of dopant distribution, an abrupt box-like junction is formed at the maximum melt depth [24].

Liquid phase epitaxy

Liquid phase epitaxy (LPE) is the commensurate growth of a solid from a liquid, based on the crystal structure of the seed or substrate material. The process of Liquid phase epitaxy begins as one atom, in order to minimize free energy, attaches itself to a metastable lattice site on the surface of the seed material. Subsequently, other atoms attach to the ledge or kink site formed by the original atom making it more stable. Atoms continue to attach to the newly formed ledge sites until an atomic layer is formed. This process continues until the liquid phase has been completely regrown.

In order for liquid phase epitaxy to occur, the melt induced by the laser needs to be in contact with a crystalline surface to provide a seed for regrowth. If the melt extends into crystalline material, regrowth may occur by LPE resulting in a single crystal [29]. If no epitaxy seed is provided at the liquid solid interface, the regrown solid is polycrystalline in structure. Polycrystalline regrowth results when the laser induced melt

does not extend beyond the amorphous region [29]. Additionally, polycrystalline regrowth can also occur even when liquid melt is in contact with the crystalline surface provided there is a steep thermal gradient at the interface, resulting in interface regrowth velocities that are too high to maintain crystalline regrowth [30, 31].

Liquid phase epitaxy results in the incorporation and re-distribution of dopant atoms, as the melt solidifies. For a laser pulse durations of less than 18 ns, the melting and solidification times are less than 100 ns in silicon, resulting in rapid regrowth of the melt. Rapid regrowth is driven by the large thermal gradient that exists in the wafer due to the surface being at the melting temperature of amorphous silicon (1480 ± 50 K [27]), while the back side of the wafer is at ambient temperature (~298 K). This thermal gradient drives liquid phase epitaxy of the silicon with melt front velocities of 2 m/s [32] to 4.5 m/s [33]. Large regrowth velocities can increase the segregation coefficient ($k = C_s/C_l$) of dopants by several orders of magnitude above equilibrium values. Figure 1-7 shows the non-equilibrium segregation coefficient of several dopants in silicon as a function of regrowth velocity. The segregation coefficient increases as the regrowth velocity exceeds the diffusion velocity of the dopant impurities in the liquid. The increase in the segregation coefficient results in a higher concentration of dopants incorporated into the solid. Hence, high regrowth velocities achieve higher dopant concentrations. Laser thermal processing utilizes high regrowth velocities to produce junctions that are highly doped with correspondingly low sheet resistance values.

Integration Issues

Laser thermal annealing of patterned wafers is non-uniform due to geometry and structural effects. A patterned wafer is constructed of multi-material structures that change in geometry and density as a function of position. Changes in material alter the

optical and thermal constants, thus altering the amount of energy that is absorbed and how it is transported [34]. Additionally, changes in geometry and the density of repetitive structures alter the interaction of the laser with the wafer, resulting in macroscopic spatial differences for energy absorbed. Attempts have been made to reduce spatial non-uniformities by using absorber layers and alternate device structures [8]. Geometry and structural effects are not addressed in the current study.

Post-LTP anneals degrade the improvements in junction activation, depth control and abruptness achieved by laser thermal processing. Anneals that occur subsequent to laser thermal processing, such as those to form silicides, remove implant damage [35] or activate dopants are collectively referred to as post-LTP anneals in the current document. In conventional process flows, after extension formation, the two highest thermal budget processes are the deep source/drain anneal and the second silicide anneal. Deep source/drain anneals are commonly performed by rapid thermal annealing at temperatures above 1000 ^{o}C for times less than 30 s, while silicides anneals can vary from minutes at 800 ^{o}C for titanium silicides to 30 s at 800 ^{o}C for cobalt or 450 ^{o}C for nickel silicides.

Post-LTP anneals provided the thermal budget for dopant diffusion and deactivation. Diffusion of dopant atoms during post-LTP annealing results in deeper, less abrupt junctions. The average length a dopant atom diffuses during a post-LTP anneal is dependent on the temperature and the anneal duration, as expressed by the diffusion length L

$$L = \sqrt{D(T) \cdot t} \qquad \text{Eqn. 1.1}$$

where $D(T)$ is the temperature dependant diffusivity of the dopant and t is time. Diffusivity has an Arrhenius temperature relation resulting in increased diffusivity at

higher temperatures. Consequently, both higher temperatures and longer annealing times increase dopant diffusion. Diffusion is also dependant on the distribution of defects and other atomic species in the lattice. Defects in the lattice can enhance the diffusion of dopants by providing a low-energy diffusion pathway. As observed by Packan and Plummer the diffusivity of boron in silicon is enhanced as a function of the interstitial defect concentration in a process termed transient enhanced diffusion [36]. An interstitial defect is an extra atom between atomic lattice sites. The diffusivity enhancement of boron D_B is proportional to the interstitial defect concentration [37] as described by

$$D_B = D_B^* \frac{C_I}{C_I^*} \qquad \text{Eqn. 1.2}$$

where D_B* is the boron intrinsic diffusivity, C_I* is the intrinsic concentration of interstitials and C_I is the concentration of interstitials from processing related defects. Defects are introduced to laser thermal annealed junctions by amorphization, dopant implantation and poor quality epitaxial re-growth. Specifically, the formation of the amorphous layer produces a large concentration of defects beyond the amorphous region known as the end-of-range damage [38], which provides a defect source for transient enhanced diffusion during post-LTP annealing.

Post-LTP anneals provide the thermal budget for dopant deactivation. Dopants activated above equilibrium solid solubility by laser thermal annealing are metastable. Consequently, during post-LTP anneals the supersaturated concentration of dopants incorporated in the silicon lattice deactivate by precipitating or clustering out of solution [39, 40], which results in an increase in the junction sheet resistance.

In order to maintain the advantages achieved by laser thermal processing it is necessary to reduce the subsequent deactivation and diffusion of metastable dopants,

which occur during conventional post-LTP anneals. The following sections introduce concepts pertinent to diffusion and deactivation, and propose novel schemes for reducing these deleterious effects.

Alternate Dopants

Conventionally, the choice of dopant has been restricted to those III-V species of the periodic table with the highest solid solubility in silicon in order to achieve the highest possible concentration of electrically active carriers. In contrast to traditional thermal processing technologies, the concentration of carriers activated by laser thermal processing is not strictly limited by equilibrium solid solubility. Consequently, dopant species that have previously been excluded due to low solid solubility may be activated by laser thermal processing to concentrations comparable to conventional dopants, thus providing alternative dopant species to those conventionally used.

Solid Solubility

A homogeneous mixture of two or more atomic species in the solid state is termed a solid solution. Solid solutions are composed of a solvent and solute, where the solute is the less abundant species dissolved in the more abundant solvent. The concentrations of the solute and solvent species can be varied within fixed limits without separation occurring. Solid solutions occur as substitutional or interstitial solid solutions, with the physical distinction being that substitutional solute atoms occupy solvent atom positions and interstitial solute atoms occupy gaps between solvent atoms. As it pertains to doping of semiconductors, dopant atoms must be substitutional in order to be electrically active.

Under equilibrium conditions, the maximum concentration of solute atoms that can be incorporated into the solvent is limited by solid solubility. Solute atoms in excess of the solid solubility limit are rejected from the lattice. Solid solubility changes with

respect to solute species and temperature. Figure 1-8 is a plot of the equilibrium solid solubility limits for solute species of arsenic, boron, antimony, gallium, aluminum, indium and nitrogen in silicon. By comparison, boron and arsenic have higher solid solubility limits than other group III and V species, respectively. Increased solid solubility corresponds to increased carrier concentration; thus arsenic and boron are preferentially selected as dopant species.

Activation

Laser thermal processing can activate dopants to concentrations in excess of equilibrium solid solubility in silicon. Even though the maximum solid solubility limit of boron in silicon under equilibrium conditions is approximately $2.2\text{x}10^{20}$ /cm^3 at 1150 ^{o}C [41], active boron concentrations as high as $1.0\text{x}10^{21}$ /cm^2 have been achieved by laser thermal processing [24]. Similarly, other dopant species have been incorporated into the silicon lattice at concentrations in excess of equilibrium solid solubility by LTP. As measured by Rutherford backscattering, White et al., reported achieving substitutional concentrations of gallium, indium, arsenic, antimony and bismuth above equilibrium solid solubility by LTP [42]. The population of the substitutionally incorporated dopants is not equal to the electrically active population. The active population is a fraction of the substitutional population, being a function of the species ionization energy, the temperature and the Fermi energy. For a p-type dopant the substitutional population N_A is related to active population N_A^+ by the following equation,

$$N_A^+ = \frac{N_A}{1 + 4 \cdot \exp\left(\frac{E_A - E_f}{k \cdot T}\right)} \qquad \text{Eqn. 1.3}$$

where E_A is the ionization energy of the acceptor, E_F is the Fermi energy of the doped silicon, k is the Boltzman constant and T is the temperature. Likewise, for n-type dopants the relationship between substitutional and active populations is expressed by

$$N_D^+ = \frac{N_D}{1 + 2 \cdot \exp\left(\frac{E_f - E_D}{k \cdot T}\right)} \qquad \text{Eqn. 1.4}$$

where E_D is the ionization energy of the acceptor. The exponential prefactors of 4 and 2 in Eqn. 1.3 and Eqn. 1.4 account for degeneracy in the valence and conduction bands, respectively. Based on Eqn. 1.4, a decrease in E_D for n-type dopants decreases N_D^+. Inversely, a decrease in E_A for the p-type dopants increases N_A^+. Calculation of the active population is complicated by the interdependence of the Fermi energy and the active population. Hence, the active population cannot be explicitly solved using Eqn. 1.3 or Eqn. 1.4, because both the Fermi energy and the active population are unknown. To calculate the active population it is necessary to solve the charge neutrality equation iteratively. Eqn. 1.5 is the charge neutrality equation for nondegenerate n- type extrinsic semiconductor

$$N_C \cdot e^{(E_f - E_c)/k_B \cdot T} = N_v \cdot e^{(E_v - E_f)/k_B \cdot T} - N_A + \frac{N_D}{1 + 2 \cdot \exp^{(E_f - E_D)/k_B \cdot T}} \qquad \text{Eqn. 1.5}$$

where N_C and N_V are the effective density of states in the conduction and valence bands, respectively. Additionally, E_C is the energy level of the conduction band, E_A is the ionization energy of the acceptor impurity, while k_B is the Boltzman constant and T is the temperature (298 K). For silicon the values of N'_C and N'_V are 2.75×10^{19} and 128×10^{19} /cm^3, respectively. For an n-type impurity in an p-type bulk, N_A is the background doping concentration, which is defined as 1.0×10^{17} /cm^3. At doping concentrations

greater than $1.0x10^{19}$ /cm^3 the semiconductor becomes degenerate, resulting in narrowing of band gap. To account for the narrowing of the band gap with high doping concentrations it is necessary to adjust E_C as function of acceptor impurity density N_D

$$E_C = 1.1 - 0.009 \cdot \left(\ln\left(N_D / 1.0x10^{17} \right) + \sqrt{\ln\left(N_D / 1.0x10^{17} \right)^2 + 0.5} \right) \quad \text{Eqn. 1.6}$$

Substituting Eqn. 1.6 into Eqn. 1.5 for E_C, the values of N_D and E_f can be calculated simultaneously by iteratively solving Eqn. 3.8 for a value of zero. Similarly, for a p-type the values can be solved by using the charge neutrality equation expressed in Eqn. 3.8. Based on the respective ionization energies [43], and substitutional concentrations achieved by laser thermal processing of gallium, indium, arsenic, antimony and bismuth reported by White et al., the electrically active concentrations calculated by iteratively solving the charge neutrality equation are above the respective solid solubility limits as reported in Table 1-2. Hence, low solid solubility dopant species activated by laser thermal processing may activate above solid solubility and provide an alternative to conventional dopants.

Species Deactivation

Dopants activated by laser thermal processing deactivate during subsequent post-LTP anneals. LTP can achieve concentrations of activate dopants in excess of equilibrium solid solubility [24, 44-46]. However, these super-saturated concentrations exist in a metastable state, and deactivate during post-LTP anneals [39, 40, 45, 47, 48]. The mechanism of deactivation differs with respect to the dopant species. Rousseau et al. proposed that arsenic in silicon deactivates by forming small clusters of various sizes around a vacancy, injecting an associated interstitial into the bulk [47]. In contrast, Takamurra et al. proposed that boron deactivates by the formation of inactive precipitates

[39]. Since the mechanism of deactivation is species dependant, alternate dopant species may exhibit favorable deactivation kinetics, thus making them a favorable alternative to conventional dopants.

Co-Implants

High concentrations of electrically active carriers achieved by laser thermal processing are metastable and deactivate during post-LTP anneals. Deactivation of the metastable carriers is driven in part by the supersaturation of carriers, with higher concentrations deactivating at lower annealing temperatures and with increased rate [40]. One source of the increased instability with supersaturation is lattice strain induced by the substitutional dopant. Hence, reducing the strain may reduce the amount of deactivation that occurs during post-LTP anneals.

Hume-Rothery/Solid Solublity

Hume-Rothery solubility criteria are based on atomic properties of the solute relative to the solvent. Solid solubility requires that the solvent and solute impurity have the same valence, crystal structure, and similar electronegativity. Additionally, solid solubility is limited by the size difference between the solute and solvent atoms. Hume-Rothery observed that extensive solid solubility of an atom species in another occurs only if the respective diameters of the atoms differ by less than 15% [49]. This criterion for solubility is termed the size factor. The underlying principle of the size factor is strain introduced by the solute atom. Solute atom species that differ in size from the solvent atoms distort the lattice when incorporated; this distortion is termed strain. Strain ε is defined according to

$$\varepsilon = \frac{\Delta l}{l} \qquad \text{Eqn. 1.7}$$

in which Δl is the change in length or dimension, and l is the original length. Strain is not self sustaining, but occurs with an associated stress. Stress σ is a force per unit area and is related to strain by Hooke's law

$$\sigma = E \cdot \varepsilon \qquad \text{Eqn. 1.8}$$

where E is the modulus of elasticity or Young's modulus. Hence, incorporation of a larger concentration of solute results in a net increase in the stress, providing a driving force for minimizing the concentration of solute. In contrast, if the strain could be reduced by a secondary mechanism, the size factor criteria could be relaxed, thus lowering the driving force for rejecting the solute impurity from the lattice.

Strain Compensation

Substitutional incorporation of dopants into crystalline silicon strains the lattice. Due to size mismatch between the dopant and the silicon atoms, a doped layer is strained compared to the underlying substrate. Incorporation of an atomic species with a covalent radius smaller than silicon, like boron, introduces a tensile strain to the crystalline lattice [50, 51]. In contrast, species with a larger covalent radius introduced a compressive strain. In the range of purely elastic deformation, the strain ε associated with the doped layer linearly depends on the substitutional concentration of the dopant C_{dopant}

$$\varepsilon = \beta_{dopant} \cdot C_{dopant} \qquad \text{Eqn. 1.9}$$

and the lattice contraction coefficient β. Using a linear model, the lattice contraction coefficient is calculated by

$$\beta = \left[1 - \frac{r_{dopant}}{r_{Si}}\right] \cdot N^{-1} \qquad \text{Eqn. 1.10}$$

where r_{dopant} and r_{Si} are the covalent radii of the dopant and silicon atoms, respectively, and N is the atomic density of the silicon. The sign of β is positive for a dopant species

with a covalent radius smaller than silicon, and negative for dopant species that are larger. Therefore, incorporation of two dopant species with lattice contraction coefficients of opposite sign should theoretically reduce the net strain. Based on this concept of opposing lattice contraction coefficients, Herzog et al. successfully demonstrated compensation of strain by simultaneously incorporating boron and germanium into epitaxial silicon [52], which has since been reproduced [53-58]. For a strained layer, the concentration of an impurity required to compensate the strain depends on the magnitude of the lattice contraction coefficient, with a large magnitude requiring less of a concentration to produce an equivalent strain or strain compensation. Strain introduced to the silicon lattice by an impurity can be reduced by incorporation of a second species of opposite strain. Hence, reducing the strain by co-implantation may relax the size criteria for solid solubility and thus reduce the deactivation of supersaturated dopants during post-LTP anneals.

Hypothesis

Activation of conventional dopants by laser thermal processing is not strictly limited to equilibrium solid solubility. Therefore it may be possible to activate unconventional dopants in excess of solubility, providing a viable alternative to conventional dopant species. Dopants activated by laser thermal processing above solid solubility are metastable and deactivate during post-LTP anneals. The deactivation mechanisms are dependant on dopant species. Therefore, in comparison to conventional dopants, alternate dopant species may prove less susceptible to deactivation during post-LTP anneals.

Conventional dopant species activated by laser thermal processing are metastable and deactivate during subsequent anneals. Dopants introduce strain to the sample, which

is potential driving force for deactivation. High doping concentrations, like those achieved by laser thermal processing, increase the strain. Reducing the strain in laser thermal processed samples may diminish the driving force for deactivation. Strain introduce by one dopant species may be reduced by an opposing strain from a second dopant species. Therefore, co-implantation of two dopant species with opposing strains may produce a net strain compensating effect that diminishes the driving force for deactivation.

Table 1-1 Abbreviated 2002 ITRS Doping Technology Requirements [5].

Year of Production	**2001**	**2004**	**2007**	**2010**	**2013**	**2016**
Technology Node (nm)	130	90	65	45	32	22
MPU, Functions per chip (Gbits)	0.54	1.07	4.29	8.59	34.36	68.72
Physical Gate Length (nm)	65	37	25	18	13	9
Contact X_j (nm)	48-95	27-45	18-37	13-26	10-19	7-13
Drain extension X_j (nm)	27-45	15-25	10-17	7-12	5-9	4-6
Max Drain extension R_S (PMOS) (Ω/sq.)	400	660	760	830	940	1210
Max Drain extension R_S (NMOS) (Ω/sq.)	190	310	360	390	440	570
Extension lateral abruptness (nm/decade)	7.2	4.1	2.8	2.0	1.4	1.0

White-Manufacturing Solution Exists, and Are Being Optimized

Light gray-Manufacturing Solutions are Known

Dark gray-Manufacturing Solutions are NOT Known

Table 1-2 Active carrier population calculated from the substitutional concentration and ionization energy.

Dopant	***E* (eV)**	***N* (/cm^3)**	**Max Solid Solubility (/cm^3)**	***N*$^+$ (/cm^3)**	**Activation (%)**
Gallium	0.072	$3x10^{20}$	$4x10^{19}$	$6.7x10^{19}$	22
Indium	0.16	$5x10^{19}$	$8x10^{17}$	$5.4x10^{18}$	10
Arsenic	1.066	$5x10^{21}$	$1x10^{21}$	$3.4x10^{21}$	68
Antimony	1.081	$6x10^{20}$	$6x10^{19}$	$5.2x10^{20}$	87
Bismuth	1.051	$7x10^{20}$	$8x10^{17}$	$4.8x10^{20}$	69

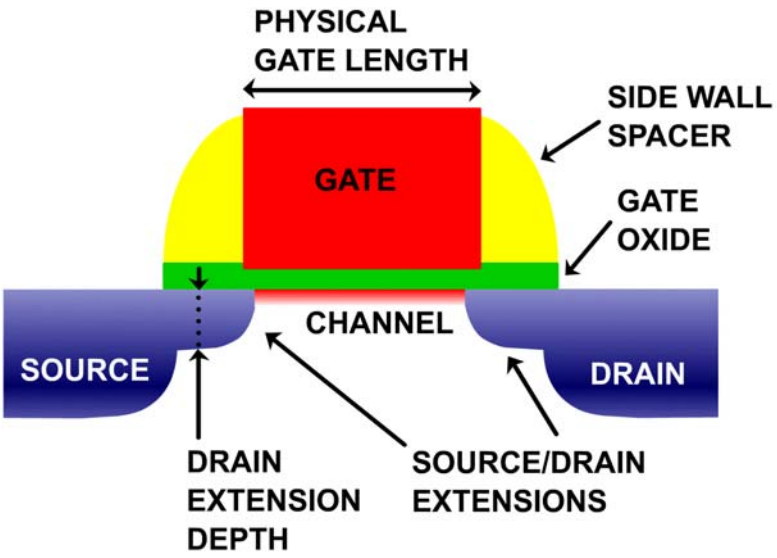

Figure 1-1. Cross-sectional schematic of a MOSFET.

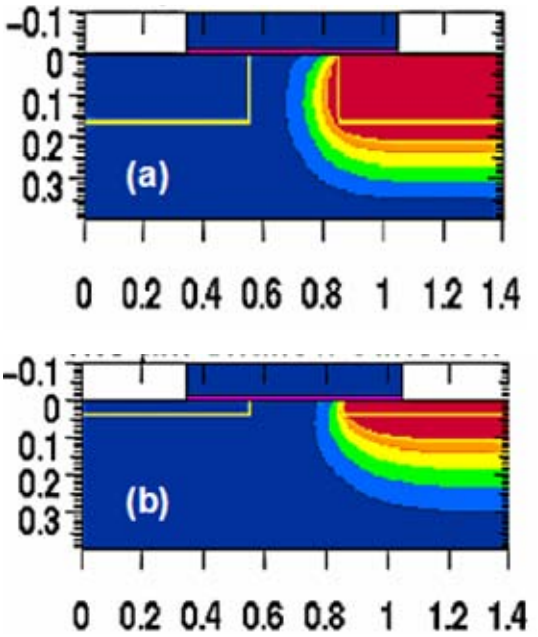

Figure 1-2. Simulation of depletion potential contours for devices biased in an off-state condition (a) 30 nm shallow junction and (b) 150 nm deep junction [2].

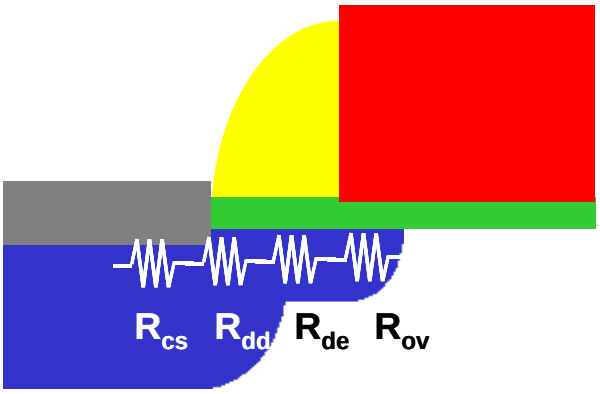

Figure 1-3. Illustration of MOSFET front-end parasitic resistance components: silicide contact resistance R_{cs}, deep drain resistance R_{dd}, drain extension resistance R_{de}, and the drain extension-to-gate overlap resistance R_{ov}.

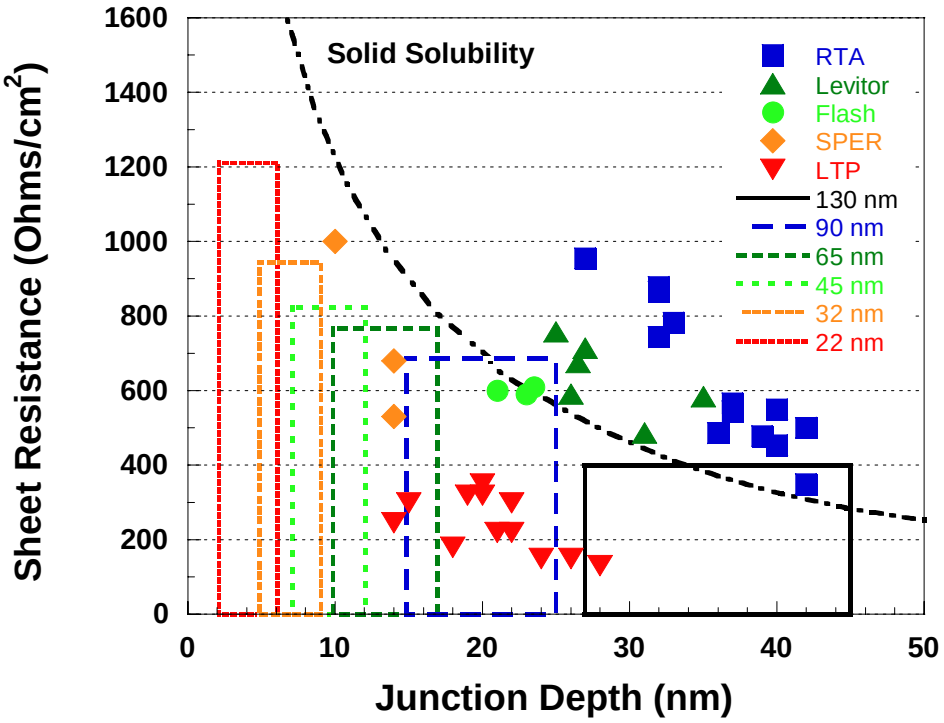

Figure 1-4. Sheet resistance versus junction depth for p-type dopants activated by rapid thermal annealing, Levitor, Flash, SPER and LTP [9]. The solid solubility line represents an impurity concentration of 2.0×10^{20} /cm^3, which is obtained at a temperature of 1050 ^{o}C for boron.

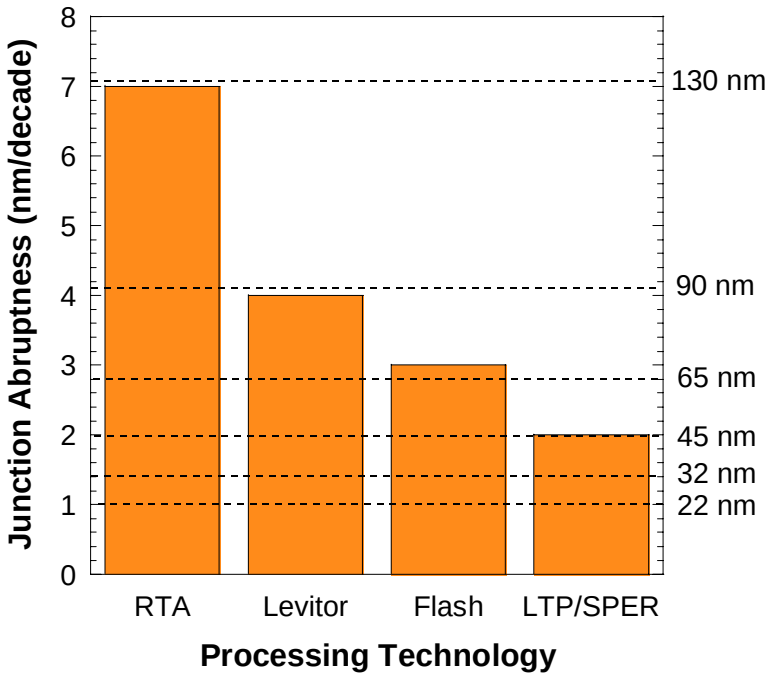

Figure 1-5 Vertical junction abruptness for p-type dopant gradients achieved by rapid thermal annealing, Levitor, Flash, SPER and LTP [9]. An abruptness of 2 nm/decade is the resolution of secondary ion mass spectrometry.

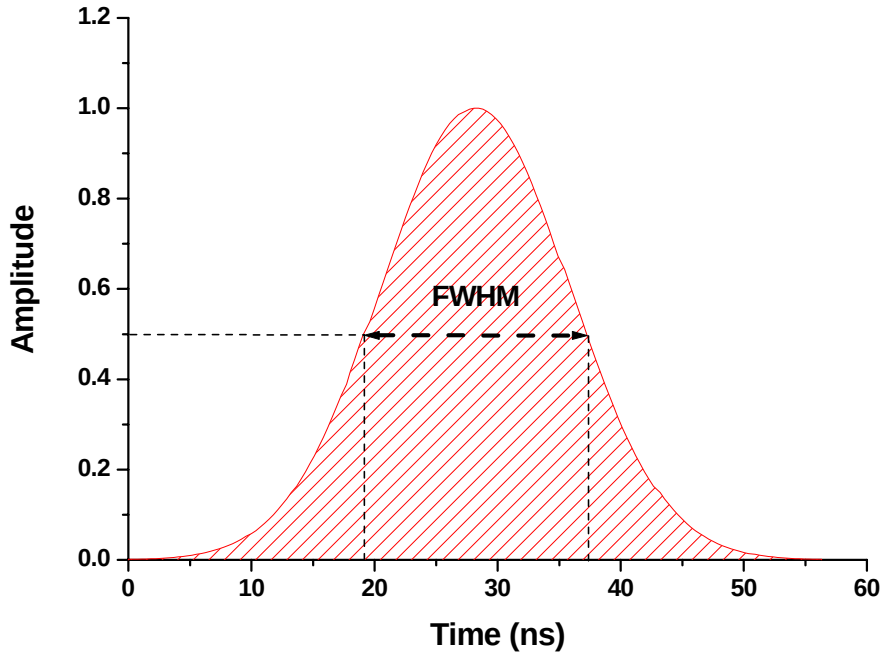

Figure 1-6 Gaussian distribution of laser intensity with respect to time with a FWHM of 18 ns.

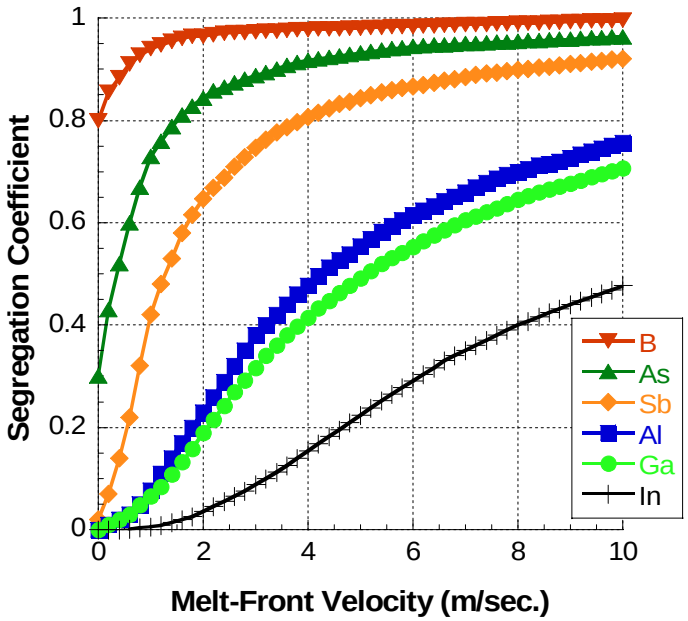

Figure 1-7 Non-equilibrium segregation coefficients for dopants in silicon [59].

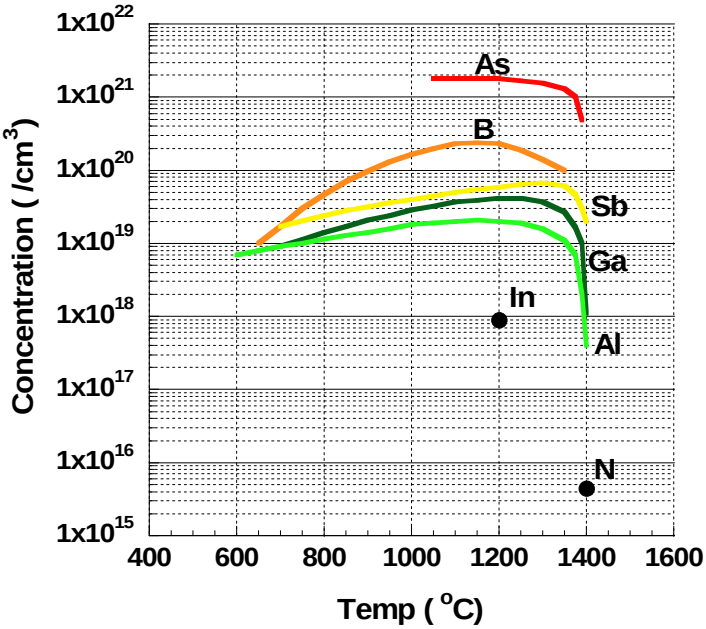

Figure 1-8 Equilibrium solid solubility limits for impurities in silicon [41].

CHAPTER 2
EXPERIMENTAL METHODS

The purpose of the current chapter is to describe the processing of the samples under test and to explain the analytical techniques used to characterize the samples.

Test Matrices

The experimental matrices are designed to test the hypotheses by means of measurement and characterization of the junctions formed by melt laser thermal processing of alternate dopant species and co-implants. In both alternate dopant and co-implant matrices, processing begins with silicon wafers, which are amorphized by silicon self implants to a depth of approximately 400 Å. The amorphous layers are implanted with the respective dopant species at sufficiently low energies to confine the dopants to the amorphous region (Table 2-1 & Table 2-2). After implantation, the doped amorphous layers are irradiated with a laser at six separate energy densities. Finally, the processed areas of the wafers are characterized both before and after post-LTP annealing to determine activation and deactivation behavior of the respective dopant species. Figure 2-1 is a cartoon depicting the processing flow for the alternate dopant and co-implant experiments.

Alternate Dopants

The alternate dopant test matrix is designed to test the hypothesis that laser thermal processing of alternate dopant species may achieve electrical activation and deactivation that is favorable to conventional dopants. The term “alternate dopants” includes elements from both groups IIIA and VA of the periodic table (Figure 2-2) but is restricted to the

elements of nitrogen (14N), aluminum (27Al), gallium (70Ga), indium (115In) and antimony (209Sb), which are shaded in light gray. Arsenic (33As) and boron (5B) are included in the experimental matrix as controls for the respective alternate dopant species of same carrier type.

In the alternate dopant experimental matrix, <100> Czochralski grown silicon wafers of n- and p-type are implanted with 15 keV 28Si+ at a dose of 1x1015 /cm2 to create an amorphous layer of approximately 300Å in depth. Utilizing TRansport of Ions in Matter (TRIM) software the energies necessary to confine dopant implants of 28N2+, 27Al+, 70Ga+, 75As+, 115In+ and 209Sb+ to the amorphous layer are simulated (lighter elements necessitate lower implant energies). With the exception of boron and nitrogen, which require an implant energy of 2.5 keV to confine the implanted ions to the amorphous layer, all other dopant species are implanted with at 5 keV. Using the energies predicted by TRIM, each dopant species is implanted at doses of 1.0x1014, 5.0x1014 and 1.0x1015 /cm2 into the respective amorphous surface layers (Table 2-1). The background doping of each bulk silicon wafer is of opposite type to that of the implant species.

LTP processing is performed utilizing a 308 nm laser pulse of approximately 18 ns duration. The laser energy density is stepped in 0.04 J/cm^2 increments from approximately 0.68 to 0.80 J/cm^2, which spans the processing window for melting a 200-350 Å amorphous silicon layer [25, 60]. The pulse to pulse repeatability in the laser energy density is ±0.02 J/cm^2 [61]. For post-LTP annealing, the junctions formed by LTP receive an RTA at 900^{o}C for durations as short as a 1 s and up to 300 s in an ambient of nitrogen.

Co-Implants

The co-implant test matrix is designed to test the hypothesis that dopant species activated by laser thermal processing can be stabilized against deactivation that occurs during post-LTP anneals by strain compensation. Specifically, boron which introduces a tensile strain to the silicon lattice is implanted at a fixed dose, while indium which produces a compressive strain is co-implanted at multiple doses.

In the co-implant experimental matrix, 200 mm <100> Czochralski grown silicon wafers of n-type are implanted with 15 keV $^{28}Si^{+}$ at a $1.0x10^{15}$ /cm^2 dose to create an amorphous layer of approximately 300 Å in depth. The amorphous layer is subsequently implanted $^{5}B^{+}$ at 1 keV with a $3x10^{15}$ /cm^2 dose. To this point in the processing all wafers are identical. Implants of $^{49}In^{+}$ at 5 keV split the process flow as a function of indium dose as follows: $0.0x10^{0}$ (control), $1.0x10^{14}$, $5x10^{14}$, $1.5x10^{15}$ and $3.0x10^{15}$ /cm^2. Table 2-2 contains the implant conditions for the co-implant experimental matrix.

LTP is performed using a 308 nm laser pulse of approximately 18 ns duration. The laser energy density is varied from 0.66 to 0.74 J/cm^2, with a step size of 0.04 J/cm^2. For post-LTP annealing, the junctions formed by LTP receive an RTA at 900 ^{o}C for durations as short as a 1 s and up to 600 s in an ambient of nitrogen.

Annealing Conditions

Two distinct types of thermal anneals are performed in the course of the study. Laser thermal anneals are used to homogenize the dopant distribution and to activate the dopant species. Rapid thermal anneals are used to reproduce the thermal budget effects of post-LTA anneals, such as a deep source/drain anneal or the formation of a salicide.

Laser Thermal Processing

Laser thermal processing is performed with a 308 nm wavelength XeCl excimer laser at Verdant Technologies in Santa Clara, California. The laser pulse as a function of time is Gaussian in shape with a full-width-half-maximum duration of approximately 18 ns (Figure 1-6). Each exposure location is irradiated with a single pulse. Energy densities are determined by fitting a third-order polynomial calibration curve associated with the melting temperature of an intrinsic silicon wafer, which is determined by plotting the surface reflectivity as a function of the system attenuator angle that controls the power output set point [62]. Thermal ramp rates are on the order of 1.0×10^{15} ^{o}C/s [63]. The area irradiated by the laser pulse is a 5 mm x 5 mm. Subsequent to laser thermal processing the irradiated areas are diced into 4 mm x 4 mm samples to reduce the measurement error associated with roll-off of the laser intensity near the perimeter edges [64].

Rapid Thermal Annealing

Rapid thermal annealing of the samples after laser thermal processing (i.e., post-LTP anneal), is performed with an AG Associates Heatpulse 610 located at the SWAMP Group laboratories at the University of Florida. The system uses top and bottom halogen-lamp arrays to heat the wafer by radiative energy transfer. Temperature of the wafer is measured either by a thermocouple for peak temperatures below 700 ^{o}C or by a pyrometer for peak temperatures above 700 ^{o}C. The temperature is increased at a rate of 120 ^{o}C/s, while the rate at which the wafer cools is less than 80 ^{o}C/s. Hence, the thermal budget for rapid thermal anneal is dominated by the cooling rate of the wafer. During annealing, a nitrogen gas flow of 2 slpm is maintained in the chamber to provide a non-oxidizing ambient.

Analytical Techniques

To study the effects of using alternate dopants and co-implants in junctions activated by laser thermal processing a variety of analytical techniques are employed. Four-Point Probe and Hall Effect Measurement are used to quantify sheet resistance, with Hall Effect also used to measure the sheet number and calculate the carrier mobility. Secondary Ion Mass Spectrometry is used to profile the dopant concentration as a function of depth. Transmission Electron Microscopy is used in both plan-view and cross-section orientations, with cross-section used to image the depth of the amorphous layer and plan-view used to image the defect population and crystallinity of the junction. High Resolution X-Ray Diffraction is used to measure the lattice parameters and extract strain induced by doping. Additionally, Ultraviolet-Visible Spectrometry is used to elucidate the effect of ion implantation conditions on the optical interaction of the laser with the silicon samples. All of the above techniques are briefly discussed in the following sub-sections, with more detail given to concepts that are critical to understanding of the experimental results.

Secondary Ion Mass Spectroscopy

Dynamic Secondary Ion Mass Spectrometry, commonly referred to as SIMS, is used to quantify the concentration of elemental impurities as a function of depth $C(x)$. SIMS is a destructive technique that uses a focused ion beam to eject neutral and charged particles from the sample surface. Ionized particles ejected/sputtered from the sample surface compose the secondary ion beam, which is directed through a mass spectrometer that separates the ions according to their mass/charge ratio. The number of ions of a selected mass/charge ratio is quantified as they strike a detector, thus providing chemical

analysis of a small volume. With time, each analysis volume advances deeper into the sample resulting in a depth profile of the impurity.

The focused ion beam or primary beam transfers energy and momentum through direct or indirect collisions with the sample surface. In addition to sputtering particles, interaction of the primary ion beam with the sample surface creates a mixing zone consisting of implanted primary ions and displaced sample atoms. The depth of the mixing zone, which limits the depth resolution, is a function of primary ion energy, angle of incidence, mass and sample material. The rate at which the mixing zone advances into the sample is termed the erosion rate. Erosion rate is increased by increasing the primary ion beam current density, increasing the primary ion atomic mass or energy, or by decreasing the angle of incidence.

SIMS only measures the ionized impurities, not the neutral impurities, thus the detection limit of an element is determined by how efficiently it is ionized by the primary beam. The more elemental ions produced per incident ion, the lower (better) the resulting detection limit for that element. The ionization efficiency is termed ion yield. Ion yield is determined by the intrinsic tendency of an element to be ionized, which is referred to as ionization potential for positive ions or electron affinity for negative ions. For example, boron has a higher ionization potential than does fluorine, and therefore has a higher positive ion yield. Conversely, fluorine has a higher electron affinity than boron does and therefore has a greater tendency to gain an electron and form a negative ion. The primary ion beam is chosen to optimize the ionization yield as a function of impurity species. The primary ion beam can consist of oxygen (O_2^+ or O^-), cesium (Cs^+), or argon

(Ar^+) ions. The use of an oxygen ion beam can increase the number of positive ions produced, while the use of cesium can increase the production of negative ions [65].

Depth profiles for the boron, aluminum, gallium, indium and antimony implants are performed with a 2 keV O_2^+ primary beam, 50 nA primary current and 250 mm raster using an ADEPT 1010 Dynamic SIMS System by PHI. Depth profiles for nitrogen and arsenic implants are performed similarly with the exception that the primary beam is Cs^+.

A typical SIMS depth profile is collected as secondary ion counts per second versus sputter time and converted to concentration versus depth by using element standards and by measuring the sputtered crater depth. The concentration scale is determined by using calibrated implantation standards in silicon resulting in an absolute error of 20 % and relative error of 10 %. The depth scale is directly proportional to the depth of the crater, which is measured by a profilometer (ex-situ). Absolute error of the depth measurement is less than 5%, assuming a constant erosion rate.

Four-Point Probe

Sheet resistance provides a quick method to quantify the resistance and approximate the carrier concentration of an electrical layer. To understand the measurement, consider a rectangular layer of doped silicon of length *l*, width *w*, and thickness *t*. The resistance measured between the parallel faces of width *w* and thickness *t* is described by

$$R = \frac{\rho(t)}{t}\frac{l}{w} \qquad \text{Eqn. 2.1}$$

where $\rho(t)$ is the specific resistivity of the measured layer in units of ohm distance (ohms·cm) and varies with thickness *t*. Eqn. 2.1 may be rewritten as

$$R = R_S \frac{l}{w} \qquad \text{Eqn. 2.2}$$

where R_s is defined as the sheet resistance of the layer in units of ohms. If the layer takes the form of a square sheet, the resistance is reported by R_s, independent of the actual dimensions. Hence, the sheet resistance is often reported in units of ohms per square (ohms/sq).

The carrier concentration can be approximated from sheet resistance and junction depth x_j. For a junction with a high concentration of electrically active carriers the sheet resistance is defined by

$$R_S = \frac{1}{q\int_0^{xj} \mu(C) \cdot C(x) \cdot dx} \qquad \text{Eqn. 2.3}$$

where, $\mu(x)$ is the mobility of the majority carrier in the layer and is a function of the carrier concentration at a given depth, and $C(x)$ is the carrier concentration as a function of depth. For a known doping profile, x_j is defined as the depth at which the doping concentration is equal to 1.0×10^{18} /cm^3 (background doping), and the mobility is approximated from tabulated values based on the average dopant concentration. With x_j and μ known, Eqn. 2.3 can be solved for the carrier concentration.

Sheet resistance is measured with a four-point system manufactured by Jandel Engineering Ltd. The probe head contains four linearly placed tungsten-carbide probes, as illustrated in Figure 2-3, which are used to contact the surface of the test sample. Current I is made to flow between the two outer probes, and voltage V is measured between the two inner probes. For a semi-infinite sample, and equal probe spacing s, sheet resistance R_S is calculated by

$$R_S = \frac{\rho}{t} = \frac{2 \cdot \pi \cdot s \cdot \frac{V}{I}}{t} \qquad \text{Eqn. 2.4}$$

where, ρ is resistivity and t is the thickness of the electrical junction. Practical samples, however, are of finite size. Therefore, the right hand side of Eqn. 2.4 needs to be multiplied by a correction factor [66].

$$R_S = \frac{\rho}{t} = \frac{V}{I} \cdot CF \qquad \text{Eqn. 2.5}$$

CF is a correction factor accounting for the physical dimensions of the sample and the probe spacing. The correction factor for 4 mm x 4 mm square samples used in this study is 3.0723 [67].

For the Jandel multi-position wafer probe, the physical probe spacing (S_1=S_2=S_3) between the probes is 1.016 mm (Figure 2-3), and the probe loading is 60+ g per probe of 100 μm radius. The reported sheet resistance values are the average of four measurements, two of which are parallel to the sample edges and two of which are diagonal. Error is reported in percentage difference between the four measurements.

Hall Effect Measurement

Hall Effect in the van der Pauw orientation provides a direct measure of the electrically active carrier concentration and the sheet resistance, which allow the calculation of the carrier mobility. The basic physical principle underlying Hall Effect is the Lorentz force. When a carrier in an electric field moves in direction perpendicular to an applied magnetic field, it experiences a force acting normal to both directions and moves in response to this force. Carriers subject to the Lorentz force initially drift away from the current path towards the edge of the sample, resulting in an excess surface electrical charge on the side of the sample. This charge results in a voltage due to the

potential drop across the two sides of the sample. This transverse voltage is the Hall voltage V_H and its magnitude is described by,

$$V_H = \frac{I \cdot B}{q \cdot n \cdot d} \qquad \text{Eqn. 2.6}$$

where I is the current, B is the magnetic field, d is the sample thickness, and q is the elementary charge (1.602×10^{-19} C). Sign of the Hall voltage is opposite for *n*-type and *p*-type semiconductors, the actual sign depends on specific orientation of I and B in set up of the measurement apparatus.

It is convenient to quantify the carrier population using sheet number n_s,

$$n_s = n \cdot d \qquad \text{Eqn. 2.7}$$

instead of bulk density n. Substituting Eqn. 2.7 into Eqn. 2.6 and solving for n_s produces,

$$n_s = \frac{I \cdot B}{q \cdot |V_H|} \qquad \text{Eqn. 2.8}$$

Thus, by measuring V_H for known values of I, B, and a constant q, the sheet density of electrical carriers is known. The units of sheet density are carriers per area, not per unit volume, which are the units for bulk density.

Sheet resistance R_S of the semiconductor can be conveniently determined by use of the van der Pauw resistivity measurement technique. Since sheet resistance includes both sheet number n_s and mobility μ,

$$R_S = \frac{1}{q \cdot \mu \cdot n_s} \qquad \text{Eqn. 2.9}$$

Hall mobility can be calculated by substituting Eqn. 2.8 for the sheet number into Eqn. 2.9 and solving for μ.

$$\mu = \frac{|V_H|}{R_S \cdot I \cdot B} = \frac{1}{q \cdot n_s \cdot R_S} \qquad \text{Eqn. 2.10}$$

Van der Pauw demonstrated that there are actually two characteristic resistances R_A and R_B, associated with the corresponding terminals shown in Figure 2-4. R_A and R_B are related to the sheet resistance R_S through the van der Pauw equation

$$\exp\left(\frac{-\pi \cdot R_A}{R_S}\right) + \exp\left(\frac{-\pi \cdot R_B}{R_S}\right) = 1 \qquad \text{Eqn. 2.11}$$

which is solved numerically for R_S.

The two characteristic resistances are obtained by applying a dc current I into contact 1 and out of contact 2 while measuring the voltage V_{43} from contact 4 to contact 3 as shown in Figure 2-4. Next, the current I is applied into contact 2 and out of contact 3 while measuring the voltage V_{14} from contact 1 to contact 4. R_A and R_B are calculated using the expressions,

$$R_A = \frac{V_{43}}{I_{12}} \quad and \quad R_B = \frac{V_{14}}{I_{23}} \qquad \text{Eqn. 2.12}$$

The objective of the Hall measurement in the van der Pauw orientation is to determine the sheet number n_s by measuring the Hall voltage V_H. The Hall voltage measurement consists of a series of voltage measurements with a constant current I and a constant magnetic field B applied perpendicular to the plane of the sample. Conveniently, the same sample as used for sheet resistance measurement, shown in Figure 2-5, can also be used for the Hall measurement. To measure the Hall voltage V_H, a current I is forced through the opposing pair of contacts 1 and 3 and the Hall voltage V_H (= V_{24}) is measured across the remaining pair of contacts 2 and 4. Using the measured Hall voltage V_H, the sheet number n_s is calculated by using Eqn. 2.8.

The Hall and van der Pauw software (Hall and van der Pauw Measurement System Software Package v. 2.0) defaults to a current based on 85% of the minimum current between any pair of contacts when the potential is maintained at 1.5 V. Ohmic contacts are formed by pressing indium metal onto the corners of the 4 mm x 4 mm samples. The magnetic field is fixed at 3000 G, and measurements are taken at room temperature.

Hall Effect measurements are performed using a system manufactured by MMR Technologies that includes the M-50 bench top electromagnet, MPS-50 programmable magnet power supply, K-20 programmable temperature controller, and H-50 Hall, van der Pauw controller. The system is located in the SWAMP Group laboratories at the University of Florida.

Transmission Electron Microscopy

Transmission Electron Microscopy (TEM) is used to quantify amorphous layer depth and qualify the crystallinity of laser thermal processed samples. Cross-sectional TEM or XTEM is used to image the amorphous layer on edge. XTEM specimens are prepared by cutting 0.5 mm strips of the sample perpendicular to the surface. Six strips are adhered together on edge with a thermally activated epoxy-resin. The center two strips are oriented with the surfaces of interest mating together. Mechanical polishing with silicon carbide abrasive papers thins the multi-strip specimen to approximately 0.2 mm. Disks of 3 mm diameter are cut from the thinned specimen using an ultra-sonic disc cutter. The disks are concentrically dimpled until the center region is thin enough to allow light transmission. An ion mill further thins the specimen until it will transmit electrons. Micrographs of the amorphous layer are taken parallel to the [111] zone-axis (parallel to the surface of the sample) under bright field conditions at a 100,000 magnification.

Crystallinity of the regrown amorphous layer after laser thermal processing is determined by comparisons of plain-view TEM (PTEM) diffraction patterns and defect micrographs. PTEM diffraction patterns and defect micrographs for a sample are obtained from the same TEM specimen. The PTEM specimens are prepared by coring 3 mm disks from the sample using an ultrasonic disk cutter. Mechanical polishing with silicon carbide abrasive papers thins the specimen to approximately 0.2 mm. Chemical etching of the back surface of the specimen with a 25:75 % hydrofluoric (HF) nitric acid (HNO_3) mixture produces a hole with edges that allow electron transmission. Before etching, the surface of interest and the perimeter of the back face are coated with paraffin wax to prevent etching. Diffraction patterns are obtained parallel to the [001] zone axis (perpendicular to the surface of the sample) at a camera length of 82 mm and with a number 3 selected area aperture. Defects are imaged at a 50,000 magnification in a $\mathbf{g}.3\mathbf{g}$ centered weak-beam dark-field (WBDF) condition. The condition is achieved by selecting the $\mathbf{g}_{220}$ reflection of the [001] zone axis with a number 4 objective aperture in dark-field mode and translating the reflection to the location of the primary beam in bright field, thus establishing a condition for high contrast intensity.

The diffraction pattern of crystalline silicon perpendicular to the [001] zone axis is a symmetric square pattern. Figure 2-6 is a cartoon of the standard indexed diffraction of a face-center-cubic (fcc) crystal in the [001] beam direction. The crystal structure of silicon is variant of the face-centered-cubic structure termed diamond cubic, which consist of two interpenetrating fcc structures. Consequently, the diffraction pattern of silicon is different from that of that depicted for the standard fcc pattern. For silicon, the

{200} and {420} families of diffraction spots are forbidden, resulting in the pattern of black spots depicted in Figure 2-6.

Diffraction patterns for polycrystalline silicon are nested rings concentric about the transmitted beam. For polycrystalline silicon the orientation of the grains with respect to the beam is not confined to the [001] direction, thus allowing additional diffraction conditions. Specifically, for the [011] and [112] beam directions the diffraction of the (111 family of planes occur. Additionally, the random orientation of the poly grains result in the effective rotation of the diffraction spot patterns about the transmitted spot, resulting in nested rings (Figure 2-7).

TEM analysis is performed using a JOEL 200CX at the Major Analytical Instrument Center (MAIC) at the University of Florida. All TEM analysis is performed at an accelerating voltage of 200 keV.

High-Resolution X-Ray Diffraction

High Resolution X-Ray Diffraction (HR-XRD) rocking curve analysis is used to measure the lattice parameter of dopant implanted silicon layers. Changes in the out-of-plane, $a_{\perp}$, lattice spacing due to doped layers are measured by performing 2θ-ω scans symmetrically about the (004) silicon reflection.

In basic structure the HR-XRD system consist of an x-ray tube, primary optics, goniometer, secondary optics and detector. X-rays are generated in the x-ray tube or source by an electron accelerating voltage of 45 kV at a current of 40 mA. The orientation of the source is fixed in space. X-rays exit the source through the primary optics. The primary optics setup consists of a ½ ^{o} divergence slit and a hybrid monochromator. Divergence slits control the equatorial divergence of the incident beam.

The hybrid monochromator consists of a parabolic graded multi-layer mirror and a channel-cut Ge crystal, which deliver an intense parallel beam of Cu-$K_{\alpha 1}$ radiation (λ = 1.540597 Å), suppressing the $K_{\alpha 2}$ component to a level below 0.1 %. X-rays conditioned by the primary optics are incident on the sample, which is mounted on the goniometer. The goniometer articulates the sample with four-circle rotation and three-dimensional translation. Axes of the four-circle rotations are phi, chi, omega and two-theta. Phi is the rotation of the sample about the axis perpendicular to the surface. Chi is the rotation of the sample about the axis parallel to the sample surface and in line with the beam path. Omega is the rotation of the sample about the axis parallel to the surface of the sample and perpendicular to the beam path. Two-theta is the rotation of the sample about the omega axis times two. Two-theta is also changed by the azimuthally motion of the detector at a fixed radius about the omega axis. X-rays diffracted by the sample are selected by the secondary optics. In triple axis mode the secondary optics consist of an analyzer crystal. The analyzer crystal is a channel cut Ge crystal, which causes the diffracted beam to undergo two (220) reflections before entering the detector. The acceptance angle of the analyzer crystal is 12 arc sec. The detector quantifies the angle selected x-rays in units of counts per second.

Values reported for two-theta are absolute. Alignment of two-theta is performed by removing the sample from the beam path and incrementally stepping the detector position to obtain the maximum number of counts. The position of detector with respect to the source at which maximum counts occurs is set at the zero position. For HR-XRD rocking curve optics the maximum counts at the zero position without a sample in the beam path is approximately five million, and the two-theta full-width-half-maximum of the peak is

0.0168 degrees (Figure 2-8). All HR-XRD rocking curve analysis is performed using a Philips X'pert MRD diffraction system at the Major Analytical Instrument Center (MAIC) at the University of Florida.

Ultraviolet-Visible Spectrometer

Ultraviolet-Visible Spectrometer (UV/Vis) is used to quantify the relative reflectance of implanted silicon wafers. Changes in reflectance alter the energy density that is transferred to irradiated sample by the laser during LTP.

The UV/Vis spectrometer consists of a deuterium light source, an integrating sphere and a diode-array detector (Figure 2-8). The deuterium light source provides ultra-violet light from 180 to 400 nm in wavelength. The light source is split into reference and sample beams prior to the integrating sphere. Four sample ports are positioned on the perimeter of the integrating sphere, with the detector centered on the inside of the lower hemisphere. With respect to the reference and sample beams, the four ports are positioned so that beams enter the sphere through two ports (transmittance) and are internally incident on the other two ports respectively (reflectance). For the comparison method of measuring the total reflectance, a sample and a standard are mounted in the two reflectance ports. To measure total reflectance, which is the sum of specular and diffuse reflectance, the port that the sample beam is incident on is angled at eight degrees to the sphere tangent. For the comparison method there is no substitution error, but two scans are required, a blank and run scan. For the bank scan the sample is placed in the reference beam port and the standard in the sample beam port. Positions are reversed between the sample and standard for the run scan.

Reflectance measured by the comparison method is not the actual reflectance of the sample. The actual reflectance is calculated by multiplying the measured reflectance by

the standard. The mirror used as the standard has a calibrated reflectance of 0.957, consequently, the actual reflectance is calculated by,

$$R_{actual} = R_{measured} \cdot 0.957 \qquad \text{Eqn. 2.1}$$

All scans are performed using the same method. Scans start at a wavelength of 400 and end at 200 nm with a 1 nm step between data points. The integration time is 0.20 s, with the slit size is set to a value of two.

UV/Vis analysis is performed using a Perkin-Elmer Lambda 800 with a Labsphere 150 mm integrating sphere at the Particle Engineering Research Center (PERC) at the University of Florida.

Table 2-1 Implant energy and dose for alternate dopant experimental matrix.

Dopant	**Energy (keV)**	**Dose 1 (ions/cm^2)**	**Dose 2 (ions/cm^2)**	**Dose 3 (ions/cm^2)**
^{7}Nitrogen	2.5	$1.0x10^{14}$	$5.0x10^{14}$	$1.5x10^{15}$
^{5}Boron	2.5	$1.0x10^{14}$	$5.0x10^{14}$	$1.5x10^{15}$
^{13}Aluminum	5.0	$1.0x10^{14}$	$5.0x10^{14}$	$1.5x10^{15}$
^{31}Gallium	5.0	$1.0x10^{14}$	$5.0x10^{14}$	$1.5x10^{15}$
^{33}Arsenic	5.0	$1.0x10^{14}$	$5.0x10^{14}$	$1.5x10^{15}$
^{49}Indium	5.0	$1.0x10^{14}$	$5.0x10^{14}$	$1.5x10^{15}$
^{51}Antimony	5.0	$1.0x10^{14}$	$5.0x10^{14}$	$1.5x10^{15}$

Table 2-2 Implant energy and dose for boron-indium co-implant experimental matrix.

Implant	**Energy (keV)**	**Dose 0 (ions/cm^2)**	**Dose 1 (ions/cm^2)**	**Dose 2 (ions/cm^2)**	**Dose 3 (ions/cm^2)**	**Dose 4 (ions/cm^2)**
^{14}Silicon	15	$1.0x10^{15}$	$1.0x10^{15}$	$1.0x10^{15}$	$1.0x10^{15}$	$1.0x10^{15}$
^{5}Boron	1.0	$3.0x10^{15}$	$3.0x10^{15}$	$3.0x10^{15}$	$3.0x10^{15}$	$3.0x10^{15}$
^{49}Indium	5.0	NA	$1.0x10^{14}$	$5.0x10^{14}$	$1.5x10^{15}$	$3.0x10^{15}$

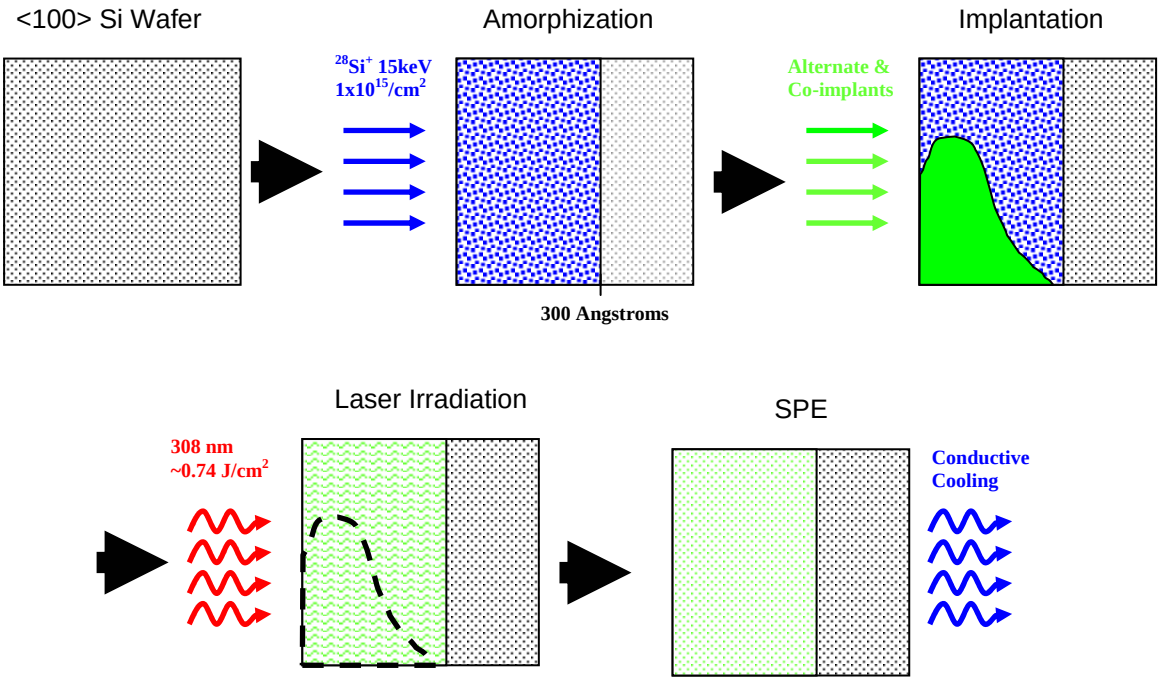

Figure 2-1 Cartoon of the generic process flow for alternate dopant and co-implant studies.

IIIA	IVA	VA	
5 10.811 tet **B** *82* 2.04 $[He]2s^2p^1$ **Boron**	**6** 12.011 hex **C** *77* 2.55 $[He]2s^2p^2$ **Carbon**	**7** 14.007 hex **N** *75* 3.04 $[He]2s^2p^3$ **Nitrogen**	
13 26.981 fcc **Al** *118* 1.61 $[Ne]3s^2p^1$ **Aluminum**	**14** 28.085 fcc **Si** *111* 1.90 $[He]3s^2p^2$ **Silicon**	**15** 30.974 cub **P** *106* 2.19 $[He]3s^2p^3$ **Phosphorus**	
31 69.732 orh **Ga** *126* 1.81 $[Ar]3d^{10}4s^2p^1$ **Gallium**	**32** 72.61 fcc **Ge** *122* 2.01 $[Ar]3d^{10}4s^2p^2$ **Germanium**	**33** 74.922 rhm **As** *119* 2.18 $[Ar]3d^{10}4s^2p^3$ **Arsenic**	
49 114.818 tet **In** *144* 1.78 $[Kr]4d^{10}5s^2p^1$ **Indium**	**50** 118.710 fcc **Sn** *141* 1.96 $[Kr]4d^{10}5s^2p^2$ **Tin**	**51** 121.757 rhm **Sb** *138* 2.05 $[Kr]4d^{10}5s^2p^3$ **Antimony**	
81 204.383 hcp **Tl** *148* 2.04 $[Xe]4f^{14}5d^{10}6s^2p^1$ **Thallium**	**82** 207.2 fcc **Pb** *147* 2.33 $[Xe]4f^{14}5d^{10}6s^2p^2$ **Lead**	**83** 208.980 rhm **Bi** *146* 2.02 $[Xe]4f^{14}5d^{10}6s^2p^3$ **Bismuth**	**atomic #** atomic weight crystal structure **symbol** *covalent radius* electroneg. elec. config. **name**

Figure 2-2 Groups IIIA, IVA and VA from the periodic table of elements.

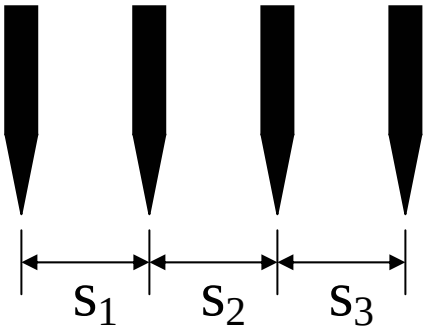

Figure 2-3 Schematic of probe spacing for a Four-Point Probe system.

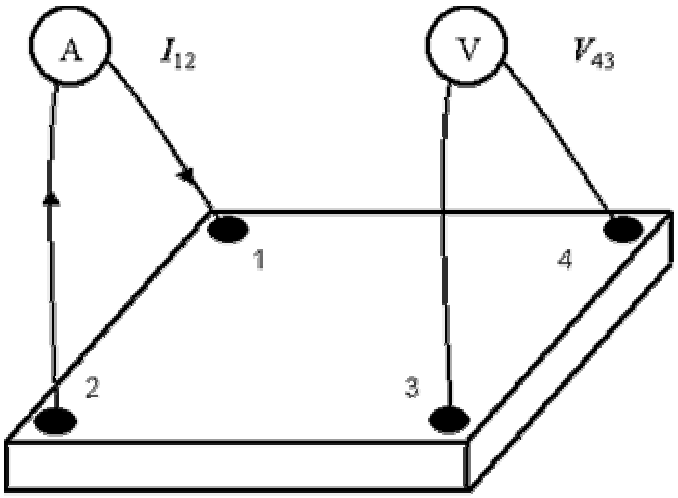

Figure 2-4 Schematic of sheet resistance measurement in van der Pauw orientation.

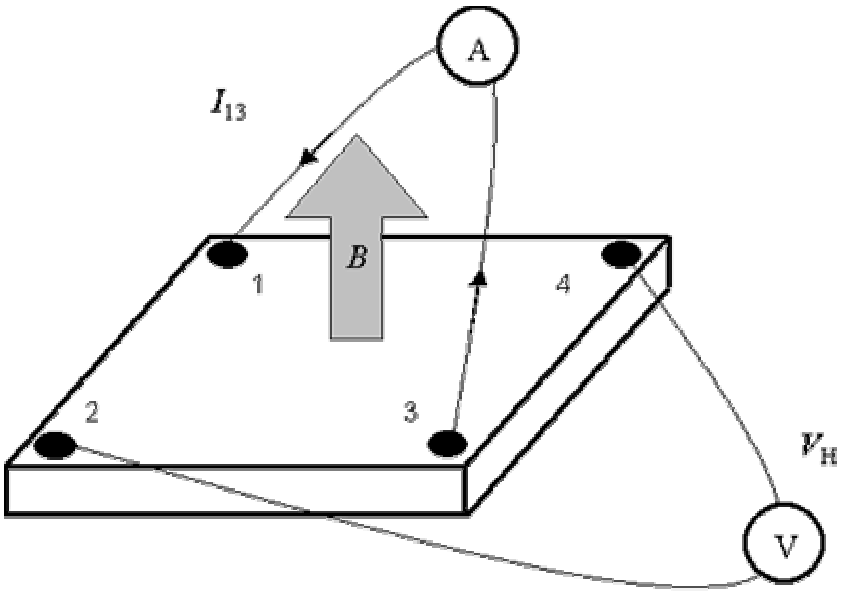

Figure 2-5 Schematic of Hall voltage measurement in van der Pauw orientation.

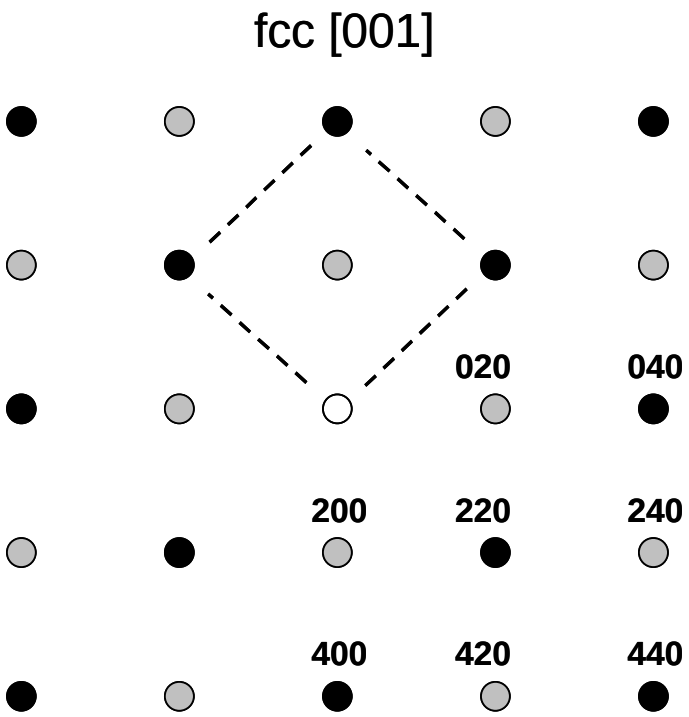

Figure 2-6 Standard index diffraction pattern for a face-centered-cubic crystal in the [001] beam direction.

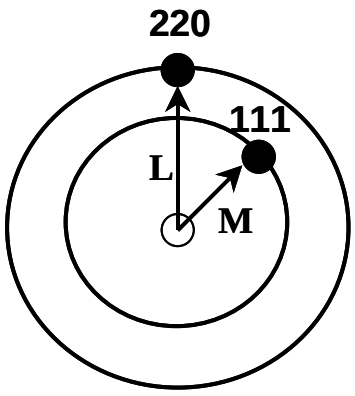

L/M = 1.633

Figure 2-7 Simplified schematic of the diffraction pattern for polycrystalline silicon.

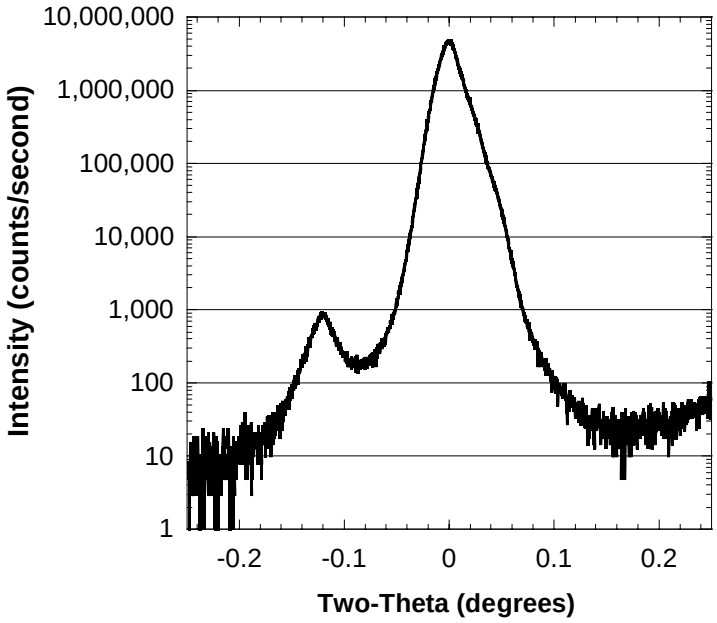

Figure 2-8 HR-XRD two-theta alignment scan without a sample in the beam path.

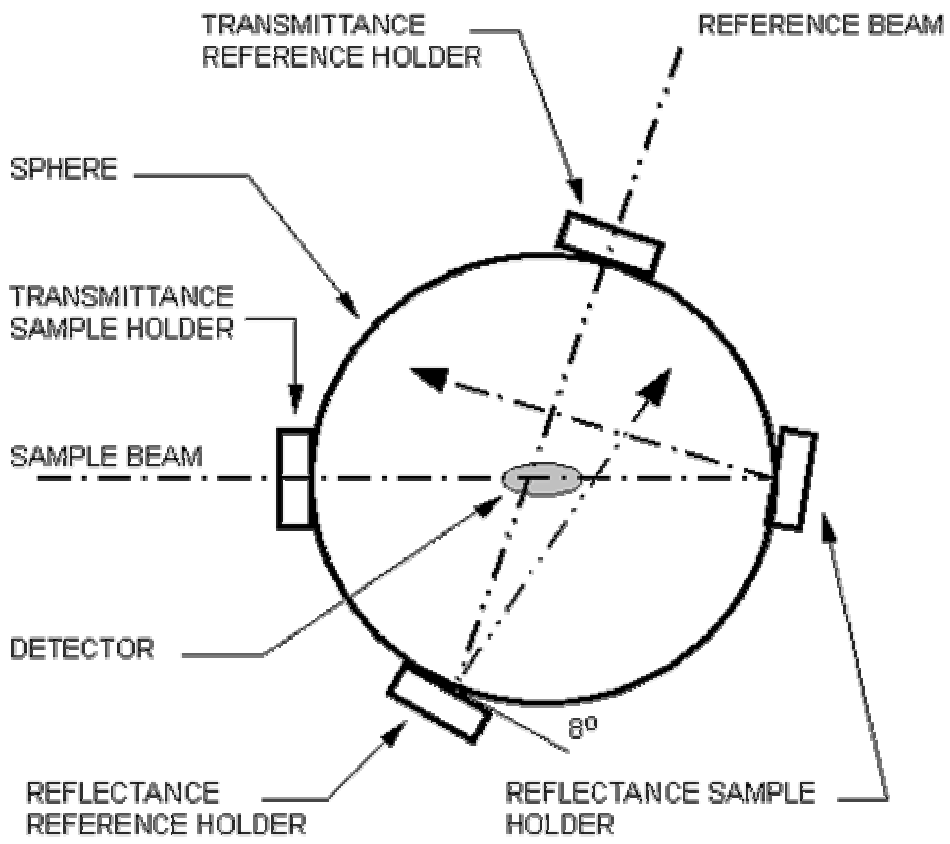

Figure 2-9 Schematic of beams and sample holders in the UV/Vis system.

CHAPTER 3
EXPERIMENTAL RESULTS AND DISCUSSION

The following sections present the experimental findings for alternate dopants and co-implant studies.

Alternate Dopants

The findings presented in the alternate dopant section elucidate whether unconventional dopant species activated by laser thermal processing are viable alternatives to conventional dopants. Beginning with the comparison of LTP activated alternate dopant species to conventional controls and continuing with the same species comparison for a subsequent post-LTP anneal. Comparison between alternate dopant species and the controls is based primarily on the electrical measurements of sheet resistance and sheet number made by Hall Effect measurement systems. Sheet resistance measurements are also made by Four-Point Probe. Details of the measurement techniques and methodologies are found in the analytical technique section within the experimental methods chapter of this work.

Implant Dose Effect on Process Window

The laser energy required to completely melt an amorphous layer changes with material and laser properties. Amorphous silicon has a melting temperature that is approximately 200 K less than crystalline silicon, thus melting an amorphous silicon layer with a laser does not require as high an energy density as does melting crystalline silicon. For an amorphous silicon layer on a crystalline substrate, the span in laser energy density from which the amorphous layer is completely melted to the onset of melting

crystalline silicon is termed the process window. The process window is determined by properties of both the material and the laser. Depth of the amorphous layer alters the laser energy density necessary to reach the lower limit of the process window as it relates to the thermal volume. A large amorphous volume requires a larger energy density to melt than does a smaller volume. The process window is also affected by the wavelength of the laser. The optical properties of absorbance and reflectivity change with respect to wavelength, and alter the amount and distribution of energy imparted by the laser to the silicon. Absorbance is the fraction of energy absorbed per unit of distance traveled in the material, and reflectivity is the fraction of incident energy reflected from the surface. In the visible to infrared regime, an increase in laser wavelength decreases the absorbance and reflectivity for amorphous silicon, thus altering the process window [68, 69]. For a constant laser wavelength the onset of melting can also be affected by changes in the optical constants due to changes in material composition. Addition of 2 at.% gallium to amorphous silicon lowers the onset of the process window to one-half that of amorphous silicon without gallium [70]. Compositional changes may also potentially alter the process window through differences in thermal constants and melting temperature.

Dose of the dopant implant into the amorphous layer alters the process window. For identical preamorphizing implants (15 keV silicon $1.0x10^{15}$ /cm^2) and laser energy densities (0.68 J/cm^2), the crystallinity and defect population of laser thermal processed samples change with respect to dose of the dopant implant. Figure 3-1 contains plan-view TEM diffraction patterns and micrographs of 5 keV indium implants at doses of $1.0x10^{14}$, $5.0x10^{14}$ and $1.5x10^{15}$ /cm^2. Despite the same preamorphizing implants and laser exposures, the diffraction patterns located in the upper right corners transition from

crystalline to polycrystalline silicon with decreasing indium dose. The transition from crystalline to polycrystalline silicon is marked by appearance of the {111} family of reflections, which appear as an annular series of spots or a ring that are radially located approximately 0.6 of the distance from the center of the transmitted spot to the {220} family of reflections (Figure 2-7). The occurrence polycrystalline silicon is indicative of a laser energy density that is too low to fully melt the amorphous layer and initiate liquid phase epitaxy from the crystalline substrate. The absence of an amorphous halo within the diffraction patterns is due to the explosive recrystallization [27]. Explosive recrystallization of amorphous silicon occurs from the polycrystalline amorphous interface due to the latent heat evolved during solidification, which is sufficient to produce a self-sustaining melt that perpetuates into the amorphous silicon not melted by the laser pulse. Explosive recrystallization is quenchable before complete consumption of the amorphous silicon, but for the current conditions it terminates at the amorphous crystalline interface resulting in a continuous polycrystalline layer. In terms of the process window, the transition from crystalline to polycrystalline silicon signifies falling below the process window, thus decreasing the indium dose has the effect of decreasing the laser energy density. Consequently, for a fixed laser energy density of 0.68 J/cm^2 only the highest indium dose of 1.5x10^{15} /cm^2 is within the process window.

The effect of the dopant dose on the process window can also be observed at the upper end of the process window in terms of the defect population. Figure 3-2 consists of plan-view TEM micrographs and diffraction patterns for samples preamorphized with silicon and implanted with indium as previously described, but laser annealed at a higher energy density. For the higher laser energy density of 0.76 J/cm^2, there is not a

distinguishable difference in the diffraction patterns as a function of implant dose. The diffraction patterns for all doses are representative of crystalline silicon, no polycrystalline rings are visible. However, dose still has a noticeable effect on the process window, but in terms of the defect population. With increasing dose the defect population in the micrographs becomes less course and dense. The reduction in the defect population is indicative of the melt extending into the crystalline substrate and exceeding the upper limit of the process window. Specifically, once the melt reaches the crystalline interface it can be regrown by liquid phase epitaxy that is seeded by the substrate. If there is sufficient energy to exceed the melting temperature of crystalline silicon the melt will continue. As the melt begins to progress into the crystalline substrate the interface becomes smoother reducing the number of dynamic interfaces that when coincident result in regrowth related defects [71]. Further progression of the melt front consumes end-of-range damage produced by the amorphizing implant. The farther the melt progresses the fewer defects result, until no defects are visible. Reduction in the defect population is indicative of an increase in the laser energy density, which allows the melt to extend deeper into the crystalline substrate. In terms of the process window, the reduction in the defect population signifies that the upper limit of the process window has been exceeded. Similarly, increasing the indium dose decreases the defect population and has the effect of increasing the laser energy density. Consequently, for a fixed laser energy density of 0.76 J/cm^2 increasing the indium dose from 1.0x10^{14} /cm^2, which is in the process window, to 1.5x10^{15} /cm^2 results in a dose induced over-melt of the crystalline substrate, which correlates to exceeding the process window (Figure 3-2).

The dose effect on the process window is not exclusive to indium, occurring for all other dopant species in the study. Figure 3-3 through Figure 3-8 are plan-view TEM micrographs and diffraction patterns for silicon preamorphized wafers implant with boron, aluminum, gallium, nitrogen, arsenic and antimony at the same doses as the indium samples ($1.0x10^{14}$, $5.0x10^{14}$ and $1.5x10^{15}$ /cm^2) and laser annealed at an energy density of 0.76 J/cm^2. Similar to doping with indium, increasing the dopant dose of each species has the effect of increasing the laser energy density.

Since the laser conditions are fixed, the root cause of the dose effect on the process window must be due to changes in the material as a function of dopant dose. Increasing the dopant dose may alter the depth, the thermal properties and or the optical properties of the amorphous layer. When observed by previous researchers for boron [72] and gallium [70], the dose effect was attributed to changes in the optical absorbance[2] and depression of the melting temperature. However, these two phenomena do not constitute the entire source of the dose effect.

Dose of the dopant implant does not alter the depth of the amorphous layer. An increase in the amorphous depth corresponds to an increase in the amorphous volume, which requires a large energy density to melt. Therefore, a dopant dose induced increase in the amorphous depth could account for the process window shift with increasing implant dose. Amorphization of silicon results from lattice damage introduced by ion implantation. In the current study, the bulk silicon is amorphized by a 15 keV implant of silicon at a dose of $1.0x10^{15}$ /cm^2. Silicon can also by amorphized by other species such

[2] In the current work the term absorbance has been used in place of absorption coefficient originally used by Bean et al. [70]. The choice to change the terminology is based on the accepted usage of the two terms. Specifically, the values are reported in units of one over distance, which are the units of absorbance not the absorption coefficient that is unitless [73].

as those used in the study if implanted with sufficiently high doses. However, the damage cascades created by the low energy implants in the alternate dopant study are too shallow to increase the depth of the amorphous layer. This statement is supported by cross-sectional transmission electron microscopy images of amorphous layers implanted with indium at 5 keV. Figure 3-9 contains XTEM micrographs of amorphous layers produced by identical amorphizing implants, but with different indium doses. Micrograph (a) in Figure 3-9 is the amorphous layer of the control, which is not implanted with indium. Micrographs (b), (c) and (d) are of sample implanted with indium doses of $1.0x10^{14}$, $5.0x10^{14}$ and $1.5x10^{15}$ /cm^2, respectively. Visual contrasts near both interfaces of the amorphous layer change between micrographs due to oxide and sample thickness effects. To aid in the quantification, arrows are added to the micrographs to define the thickness of the amorphous layer. Measuring the amorphous layer thickness as the distance spanned by the inserted vertical arrows, yields a thickness of approximately 35-40 nm (350-400 Å) for all samples. A lack of any increase in the amorphous layer depths confirms that junction depth is not increased by additional implant damage resulting from the dopant implant prior to LTP. Thus, the effect of implant dose on the junction depth can not be accounted for in terms of changes in the amorphous layer thickness.

Based on equilibrium phase diagrams, an alloy induced depression in the melting temperature is possible for boron and arsenic dopant species only at high concentrations. As depicted in Figure 3-10 and Figure 3-11 respectively, the addition of boron or arsenic to pure silicon, which melts at 1414 ^{o}C, lowers the melting temperature with increasing atomic percent of the dopant until the eutectic temperature is reached [74]. Appreciably

lowering the melting temperature requires a large concentration of the dopant. In contrast the highest dose used in the current study is $1.5x10^{15}$ /cm^2, which when distributed uniformly across a 350 Å junction results in an atomic concentration of less than one percent. According to the phase diagrams a one percent change in concentration would result in no more than a 10 ^{o}C depression of the melting temperature. Considering that the dose effect depicted in Figure 3-2 spans the melting of the crystalline substrate, a temperature difference of approximately 200 ^{o}C, it is not reasonable for a 10 ^{o}C depression in melting temperature to account for the entirety of the dose effect, even when non-equilibrium considerations are taken into account [75]. The argument for melting temperature depression by alloying is even less valid for the alternate dopant species of aluminum, gallium, indium, nitrogen and antimony. Alternate dopant species are not soluble in silicon to concentrations high enough to produce a melting temperature depression greater than 1 ^{o}C.

Dose of the dopant affects the optical properties of laser irradiated samples. As Bean et al. reported, the addition of 2 % gallium to an amorphous silicon layer results in a 2.5 times enhancement of the absorbance[2] over that of pure amorphous silicon measured at a wavelength of 1064 μm. Absorbance is the sum of the intensity loss internal to the sample through mechanisms of scattering and phonon generation. Generally scattering is assumed to be negligible, consequently, an increase in absorbance would result in increased heating through phonon generation and a shift of the process window to lower energy densities with increasing gallium does.

Increasing the dopant dose in the amorphous layer decreases the optical reflectivity. The reflectivity or reflectance is measured using a UV-Vis spectrometer. Reflectivity has

a specular and diffuse component. Specular reflectivity is the ideal component that occurs from a mirror, while diffuse reflectivity is the scattering of light in all directions of the hemisphere uniformly. Both components combine to yield the total reflectivity. Figure 3-12 is the total reflectivity measured as a function of wavelength for an n-type wafer, an amorphized n-type wafer and n-type amorphized wafers implanted with 5 keV gallium at doses of $1.0x10^{14}$, $5.0x10^{15}$ and $1.5x10^{15}$ /cm^2. All of the amorphized samples have a similar decreasing response with increasing wavelength. However, the non-amorphized wafer exhibits three peaks in the reflectivity as a function of wavelength. The three peaks indicated by arrows in Figure 3-12 are due to inter or intra-band transitions of carriers. Inter-band describes carrier transitions that occur between bands, while intra-band transitions occur between partially filled energy levels within a band. In comparison, intra-band transitions occur at lower energies, which correspond to higher wavelengths, than do inter-band transitions. The peaks exhibited by the non-amorphized n-type wafer are inter-band transitions for crystalline silicon [76]. For the amorphized samples no inter-band transitions are exhibited over the measured wavelength range. The lack of inter-band transitions over the wavelength range of 200 to 400 nm for amorphous silicon is reasonable considering that the band gap for amorphous silicon is approximately 1.7 eV, which is equivalent to a wavelength of 730 nm, well outside the measured range. The amorphized samples do, however, exhibit a relative decrease in reflectivity as a function of increasing dose of the dopant, with the reflectivity of the lowest dose ($1.0x10^{14}$ /cm^2) being similar to that of the amorphized sample without a dopant implant (N-PAI). A similar effect of dose on reflectivity is also observed for the other dopant species[3] and is summarized in Figure 3-13 for a wavelength of 308 nm. On

[3] No UV-Vis data is reported for the dopant species of boron because there are no sample pieces large

average, the maximum change in reflectivity across the dose range is approximately 6 % for all dopant species, an amount that for an incident laser energy density of 0.76 J/cm^2 would result in approximately 0.05 J/cm^2 difference in the energy density due to reflection. A 0.05 J/cm^2 difference in the energy density available for heating/melting of the sample is significant, considering that the energy difference associated with the transition between melting amorphous silicon to melting crystalline silicon is 0.04 J/cm^2 [72]. Consequently, the change in reflectivity as a function of dose does alter the energy density available for heating/melting sufficiently to account for the shift in limits of the process window as depicted in Figure 3-1 and Figure 3-2.

The change in reflectivity as a function of implant dose does not change proportionally with respect to dopant species. For the lowest dose of 1.0x10^{14} /cm^2, all species measure a reflectivity similar to that of the amorphized wafer without a dopant implant, which is approximately 37.5 % at a wavelength of 308 nm. In contrast, with increasing dose the reflectivity does not decrease proportionally for all dopant species, with arsenic exhibiting the most substantial decrease and antimony the least. The relative difference in reflectivity between arsenic and antimony is in agreement with the post-LTP defect populations imaged in Figure 3-7b and Figure 3-8b, respectively. For an implant dose of 1.5x10^{15} /cm^2 and laser energy density of 0.76 J/cm^2, arsenic has fewer defects than does antimony, implying that arsenic is receiving a higher energy density. The higher energy density for arsenic is explained by the reduction in reflectivity over that of antimony. However, this explanation does not apply as aptly for a 1.5x10^{15} /cm^2 dose of indium, which has a defect population (Figure 3-2a) similar to that of arsenic, but exhibits

---

enough for analysis. Despite the lack of reflectivity data for boron, the PTEM data implies that the reflectivity findings would be similar to the other species measured.

a change in reflectivity that is smaller than antimony (Figure 3-13). With respect to dopant species, the reflectivity data does not entirely explain the differences in defect populations, suggesting there may be additional contributing factors to the dose effect.

Correlation of the dose effect to reflectivity does not negate the findings of previous researchers. The dose effect may be the combined result of several phenomena. Specifically, while the depression of melting temperature by alloying can not account for the dose effect by itself, none of the results presented can definitively exclude it from making a contribution. In the case of absorbance there is not a direct unambiguous relation to reflectivity. Consequently, it is not unreasonable to concede that both optical properties may be altered by the addition of a dopant and dose, allowing both to contribute to the dose effect on the process window.

Increase of the reflectivity with dopant dose is explained by an increase in scattering. Prior to the alternate dopant implants the samples are physically the same. All samples are amorphized with an identical 15 keV, 1.0×10^{15} /cm^2 silicon implant, resulting in an amorphous layer that is approximately 350 Å thick. Additionally, on the surface of each sample is a native oxide, approximately 20 Å thick.[4] However, the implantation of the dopant atoms introduces additional damage. In the case of the alternate dopant implants, the energies are too low to increase the amorphous depth, but the amorphous layer is still altered by the implantation of the dopants. Neglecting the damage cascades generated by the implanted dopant atoms, the implant atoms alone introduce an additional interstitial population equivalent to the dose of the implant. The implanted atoms disrupt the periodicity of the lattice, which increases the probability that

[4] The reflectivity of the oxide is different from that of the amorphous silicon, however, because the thickness of the oxide is equivalent between samples its contribution to reflectivity is a constant.

the linear path of the incident radiation is altered (scattered). In the course of traversing the sample the radiation may transfer energy to the sample. For silicon, which is an indirect semiconductor, the energy of the incident radiation can excite an electron to a higher energy level through an inter-band process that produces both a photon (re-emission) and a phonon (lattice heating). Additionally, for lower energies, electrons may also be excited to higher energy levels within the same band through an intra-band process that also produces a phonon. Incident radiation that is transformed into phonons results in heating of the sample. In contrast, re-emitted or scattered photons that successfully traverse back through the sample to the surface are measured as reflected intensity. Scattering increases the path length that the photon traverses back to the surface, thus increasing the probability that the photon will undergo additional interactions with the sample that generate phonons and result in the eventual extinction of the photon. Hence, a large population of implanted atoms increase scattering, which decreases the probability that the radiation escape the sample surface as reflected intensity.

Process Window

To compensate for the dopant dose effect the laser energy densities are adjusted for each dose to achieve the process window. To provide a common ground for dopant comparison, the same laser energy density is used for all dopant species of a specific implant dose. For the implant doses of $1.0x10^{14}$, $5.0x10^{15}$ and $1.5x10^{15}$ /cm^2, the laser energy densities of 0.80, 0.72 and 0.68 J/cm^2 are respectively used for laser thermal processing of both the alternate dopant species and their respective controls. The laser energy density used for each dose is a median process window value, producing the least

amount of amorphous under melt and crystalline over melt considering all dopant species.

LTP Activation

Within the current section electrical junctions formed by laser thermal processing of p- (i.e., aluminum, gallium and indium) and n-type (nitrogen and antimony) alternate dopant species are compared to control species of boron and arsenic respectively. The electrical junctions are formed by laser irradiating a doped amorphous silicon layer that is approximately 350 Å thick. The laser irradiation is 308 nm in wavelength, and with respect to time is a Gaussian shaped pulse of approximately 18 ns duration. Details pertaining to the formation of junctions are found in the test matrix section within the experimental methods chapter of this work.

Sheet resistance values measured by Hall Effect after LTP differ with respect to the implant dose and dopant species. Figure 3-14 is a plot of the sheet resistance measured after LTP for p-type dopant species implanted at doses of $1.0x10^{14}$, $5.0x10^{14}$ and $1.5x10^{15}$ /cm^2. For the measurable samples[5], the sheet resistance values decrease with increasing implant dose, implying an increase in the concentration or mobility of the active carriers. Similarly, the n-type dopants of arsenic and antimony plotted in Figure 3-15 also exhibit a decrease in sheet resistance with increasing implant dose. In addition to the change in sheet resistance as a function of dose the sheet resistance also differs between species with equivalent doses. For equivalent doses the respective p- and n-type alternate dopant controls of boron and arsenic result in the lowest measurable sheet resistance.

[5] For the lower doses of aluminum and indium and all doses of nitrogen the sheet resistance values are not reproducible or do not differ from that of the bulk wafer. In these cases no sheet resistance values are reported.

For simplicity the remainder of the alternate dopant data presented focuses on the highest implant does of $1.5x10^{15}$ /cm^2. It is the highest dose that will potentially achieve the largest activation and subsequent deactivation, thus making an effect of dopant species more pronounced than for the lower doses. Additionally, for aluminum, indium and nitrogen electrical data is not obtainable for the lower doses, so comparison would be incomplete. The laser energy density that achieves the process window for the $1.5x10^{15}$ /cm^2 dose is approximately 0.68 J/cm^2.

Differences in sheet resistance values between dopant species, with a common implant dose, are a function of both the number of electrically active carriers present after LTP and their mobility. In Figure 3-16 and Figure 3-17, the number of electrically active carriers or sheet number is plotted against dopant species for the implant dose of $1.5x10^{15}$ /cm^2. For n and p-type dopant species, an increase in the sheet number corresponds to a decrease in sheet resistance. Specifically, boron exhibits a higher sheet number than that measured for gallium; consequently with more carriers available for conduction, boron implanted silicon has a lower sheet resistance than that of gallium or other p-type dopants. Similarly for the n-type dopants, arsenic has a higher sheet number than does antimony, which corresponds to a lower sheet resistance. The inverse relationship of the sheet number n_s data to sheet resistance R_S is describe by Eqn. 2.9 for a constant carrier charge q and a carrier mobility μ.

Despite having the same implanted dose the sheet number changes with respect to dopant species. Fundamentally, the number of electrically active carriers is a function of the quantity of dopant atoms implanted, the fraction of the dopant atoms that are located substitutionally in the lattice and the probability that the substitutional atoms are ionized.

The quantity of dopant atoms implanted is the dose, which is controlled during ion implantation. For equilibrium processes the fraction of dopant atoms that are substitutional is dependant on the species solid solubility. Thus, for doses in excess of solid solubility the species with a higher solid solubility occupy a larger number of substitutional sites in the lattice. Of the substitutional dopant atoms, the probability that they are electrically active is a function of the species ionization energy. An ionization energy closer to the respective conduction or valence band corresponds to an increase probability of being active. Consequently, the amount of the $1.0x10^{15}$ /cm^2 implanted dose that is electrically active changes with respect to dopant species. Figure 3-18 plots the sheet number as a function of the respective species maximum equilibrium solid solubility. Despite being a non-equilibrium process, the population of dopants activated by LTP exhibits a dependence on the solid solubility. Specifically, a decrease in the maximum equilibrium solid solubility corresponds to a decrease in the sheet number. Thus, as a function of the dopant species' solid solubility, the sheet resistance increases due to a decrease in the sheet number.

Laser thermal processing of alternate dopant species does not achieve sheet resistance values that are lower than that of their respective controls. However, LTP does activate alternate dopant species to concentrations in excess of their respective equilibrium solid solubility limits. Table 3-1 contains the maximum solid solubility and active carrier concentration for alternate dopant species of aluminum, gallium, indium, nitrogen and antimony. With the exception of nitrogen all alternate dopant species activated by LTP achieve carrier concentrations in excess to their respective maximum equilibrium solid solubility limits. Additionally, for gallium, indium and antimony the

activation is in excess of the solid solubility by more than a one half of an order of magnitude.

Post-LTP Anneal Deactivation

Post-LTP anneals like those required for activation of deep source/drains or silicide formation result in deactivation of carriers. In the previous section, activation of alternate dopant species by LTP did not achieve sheet resistances lower than that of their respective controls. As continuation, the current section studies deactivation during post-LTP anneals to determine if the alternate dopants deactivate less than their respective controls and thus achieve a lower final sheet resistance. The post-LTP anneal is performed at 900 ^{o}C in a nitrogen ambient for durations up to 300 s. Details of the annealing conditions and procedure are found in the experimental methods chapter of this work.

Annealing after activation by LTP deactivates carries for both alternate dopants and their respective controls. The number of p-type dopants activated by LTP is reduced by deactivation occurring during a post-LTP anneal. As plotted in Figure 3-19 the sheet number for all p-type dopant species decreases after a 900 ^{o}C/300 s post-LTP anneal. The reduction in the sheet number or carrier population is due to deactivation. Deactivation of the p-type carriers by the post-LTP anneal differs with dopant species. With respect to the number of carriers activated by LTP, the post-LTP anneal reduces the population by 99 % for aluminum, 96 % for gallium, 94 % for indium, and 75 % for the boron control. For the n-type dopants the post-LTP anneal also reduces the number of carriers, resulting in an 83 % deactivation for antimony, and 72 % for the arsenic control (Figure 3-20). For an implant dose of $1.5x10^{15}$ /cm^{2}, the controls of boron and arsenic

achieve larger sheet number values after LTP and experience less deactivation than the respective p- and n-type alternate dopants during the post-LTP anneal.

Deactivation of the carriers during the post-LTP anneal increases the sheet resistance for all dopant species. Figure 3-21 plots the sheet resistance measured for the p-type dopant species after LTP and again after the post-LTP anneal. For the p-type alternate dopants the post-LTP anneal increases the measured sheet resistance of indium and aluminum by one half an order of magnitude and gallium by more than a factor of two, while the control of boron increases in sheet resistance less than a factor of two. For the n-type dopants the post-LTP anneal increases the sheet resistance of antimony by a factor of 1.5, while the control of arsenic increases by less than a factor of 1.1 (Figure 3-22). After the post-LTP anneal the p- and n-type controls of boron and arsenic measure the lowest relative increase in sheet resistance and the lowest absolute sheet resistance with respect to the alternate dopant species of the same type.

Sheet resistance measured for alternate dopant species increases with duration of the 900 ^{o}C post-LTP anneal and varies in magnitude with respect to species. Figure 3-23[6] and Figure 3-24 plot the sheet resistance values for p- and n-type dopants implanted at a $1.5x10^{15}$ /cm^2 dose as a function of post-LTP annealing time at 900 ^{o}C. For both p- and n- type dopants the sheet resistance increases more dramatically within the initial thirty seconds of annealing corresponding to the deactivation of the metastable carrier population activated by LTP above solid solubility. For subsequent annealing times the

[6] There is some disparity between the sheet resistance values measured by Hall Effect and Four Point Probe, most noticeable for species of aluminum and indium. However, in relationship to the magnitude of the value the disparity is small and will not be given further consideration. The source of the disparity is attributed to small size of the samples in combination with difference in the probe geometry between the two techniques.

sheet resistances measured for boron, aluminum, gallium, arsenic and antimony continue to increase as a result of continued deactivation, but at a reduced rate. Within error, the sheet resistances measured for indium is stagnant for increased annealing duration. For both p- and n-type dopant species, the magnitude of the measured sheet resistance for a single annealing time differs with dopant species, being lowest for the respective controls of boron and arsenic.

Not all alternate dopant species were sufficiently activated by LTP to allow for electrical comparison. Despite no meaningful electrical data for nitrogen, the n-type alternate dopant is present in the silicon after LTP and the subsequent post-LTP anneal. Figure 3-25 plots the nitrogen concentration versus depth as measured by SIMS. Integration of the LTP nitrogen profile results in a retained dose of approximately $1.4x10^{15}$ /cm^2, which is less than the implanted dose of $1.5x10^{15}$ /cm^2. Additionally, after the post-LTP anneal the retained dose diminishes further to $1.2x10^{15}$ /cm^2. Nitrogen dose is lost due to surface out gassing during LTP and the subsequent anneal. However, the dose loss is not sufficient to account for the lack of electrical data, implying that for the current conditions nitrogen is not substitutional or is clustered, such that it is not active to a measurable amount. In agreement, previous researchers found that nitrogen in silicon prefers to form pairs that are displaced by 1.1±0.1 Å from lattice sites along the <100> [77, 78]. Nitrogen is present in silicon after LTP and the post-LTP anneal, but it is not sufficiently active to measure electrically different from the bulk silicon substrate. Consequently, nitrogen does not provide a viable alternative to the control of arsenic.

Non-conventional dopants activated by LTP are not electrically viable alternatives to conventional dopants. Both p- and n-type alternate dopant species activated by LTP

measure a higher sheet resistance than their respective controls. Post-LTP annealing at 900 ^{o}C deactivates a higher percentage of carriers for alternate dopants than for controls, resulting in a higher sheet resistance for the alternate dopant species[7]. Despite the ability of LTP to activate alternate dopants above solid solubility the process is still fundamentally linked to solid solubility. Consequently, even for LTP a lower solid solubility translates to less activation and higher sheet resistance. Activation of p- (i.e., aluminum, gallium, and indium) and n-type (nitrogen and antimony) alternate dopants by LTP does not offer an electrical advantage to that of conventional dopant species (i.e., boron and arsenic respectively).

Co-Implants

The Co-Implant section empirically tests the assertion that combinations of implants can reduce the deleterious effect of deactivation that occurs during post-LTP annealing. As demonstrated in the previous section, boron remains the superior choice for p-type dopants. However, like other dopant species activated by LTP above solid solubility, boron is metastable and deactivates during subsequent anneals. To retain the superior activation achieved by LTP it is necessary to reduce the deactivation that occurs during subsequent post-LTP anneals.

The metastable nature of the dopants activated by LTP is due to supersaturation of the dopants above equilibrium solid solubility limit. The solid solubility limit is in part a function of the strain that results from mismatch between the dopant atom and the lattice, with increasing strain reducing the solid solubility. Consequently, reducing the strain

[7] Deactivation data is only presented for an annealing temperature of 900 ^{o}C. Previous work by Takamura et. al. found an annealing temperature effect on the deactivation [40]. Hence the deactivation trends observed at 900 ^{o}C do not necessary extend to other temperatures.

introduced by the dopant may reduce the driving force for deactivation. With respect to crystalline silicon, dopant atoms or impurities that have a large covalent radius introduce a compressive strain to the lattice; in contrast smaller atoms introduce a tensile strain. The current section explores the co-implantation of two atomic species that are opposite in strain with respect to silicon, in an attempt to compensate the lattice strain. Specifically, indium is co-implanted into silicon to compensate the tensile strain introduced to the lattice by a boron implant; potentially diminishing the driving force for deactivation during post-LTP anneals. Based on the relative differences in covalent bonding radius between boron-silicon (-0.29 Å) and indium-silicon (0.33 Å), the dose of indium necessary to compensate the strain introduce to the silicon lattice by a $3.0x10^{15}$ /cm^2 dose of boron is approximately $2.6x10^{15}$ /cm^2. Doses of indium less than the boron doses should result in only partial compensation of the stain.

Process Window

The process window is defined as the range of laser energy densities at which the amorphous layer is completely melted without melting the crystalline substrate. Amorphous silicon melts at approximately 200 ± 50 ^{o}C lower than that of the crystalline silicon [27]. Due to the lower melting temperature, amorphous silicon melts at a lower laser energy density than crystalline silicon. In contrast, the crystalline silicon remains solid until the sufficient energy is added to raise the temperature to the crystalline melting point. The disparity in laser energy density necessary to fully melt the amorphous silicon and that to begin melting the crystalline silicon is termed the process window [61, 79, 80]. The process window allows for minor variations in the laser energy without altering the depth of the junction.

For identical laser energy densities, the crystallinity of the regrown layers is improved with dose of the indium co-implant. Crystallinity may be used to determine when the process widow is not achieved. Transmission electron microscopy is used to observe the crystallinity of the silicon samples. Plan-view transmission electron microscopy defect micrographs and diffraction patterns are pictured in Figure 3-26 through Figure 3-30 as a function of the indium dose for laser energy densities of 0.66, 0.70 and 0.74 J/cm^2. All samples have been amorphized by a 15 keV silicon implant with a 1.0x10^{15} /cm^2 dose and doped with a 1 keV boron implant to a dose of 3.0x10^{15}/cm^2. For a laser energy density of 0.66 J/cm^2, increasing the 5 keV indium co-implant dose from 1.0x10^{14} to 3.0x10^{15} /cm^2 affects both the diffraction patterns and defect micrographs, as observed from Figure 3-31. Diffraction patterns located in the upper right quadrant of the figures are obtained parallel to the silicon [001] zone axis at a camera length of 82 cm from a selected area defined by a number three aperture. The diffraction pattern for the [001] beam direction of crystalline silicon is that of a face-centered-cubic system minus the non-allowed {020} reflections (Figure 2-6). The resulting diffraction pattern appears as a symmetrical placement of spots in a square pattern. For the diffraction patterns of the samples, a pointer is placed over the transmitted beam. In crystalline silicon the spots nearest to the transmitted beam are the family of {220} reflections, while the next nearest spots are the {400} family of reflections. Occurrence of a series of spots or ring that are approximately 0.6 of the distance measured from the center of the transmitted spot to the {220} family of reflections are the {111} reflections. The {111} reflections are indicative of polycrystalline silicon (Figure 2-7), as this reflection is not allowed for crystalline silicon

in the [001] beam direction. Polycrystalline silicon consists of crystalline grains that are not strictly oriented with respect to another. Hence, the orientation of the beam is not necessarily parallel to the silicon [001] zone axis, which changes the allowed diffraction planes. It is the diffraction occurring from miss-oriented grains that produces the contribution from the {111} family of planes for polycrystalline silicon.

The presence of polycrystalline silicon after the laser exposure implies that the primary melt front did not entirely melt the amorphous layer to reach the underlying crystalline silicon. When the entire amorphous layer is not melted by the primary melt, there is no crystalline seed for epitaxy and the regrowth results in polycrystalline silicon. Additionally, the remaining un-melted amorphous layer is also transformed to polycrystalline silicon by explosive recrystallization [27, 81]. Based on the diffraction patterns for samples processed with a fixed laser energy density of 0.66 J/cm^2 (Figure 3-31), increasing the dose of co-implanted indium has the effect of increasing the laser energy density, as indicated by the transition from polycrystalline to crystalline silicon. The indium co-implant dose also has an affect on the defect population.

Reduction in the defect population implies that the primary melt extended beyond the amorphous layer into the crystalline bulk. For a fixed laser energy density of 0.74 J/cm^2, increasing the indium co-implant dose reduces the defect population as observed in Figure 3-32. The defects present after laser thermal processing are primarily from two sources, regrowth related defects and end-of-range defects. Regrowth related defects occur during liquid phase epitaxy, and vary in density with respect to the regrowth velocity and epitaxial seed quality. End-of-range defects occur in the crystalline substrate in near proximity to the original amorphous/crystalline interface as a result of

damage introduced to the lattice by the preamorphizing implant. In general, the defect population decreases with increasing laser energy density, being most noticeable when the process window is exceed and the regrowth defects no longer form and the end-of-range damage is consumed by the melt. Based on the reduction of the defect population, increasing the indium co-implant dose again has the effect of increasing the laser energy density.

For a common preamorphization and dopant implant, the dose of co-implanted indium alters the range of the process window. Shifts in the process window as a function of dopant dose for single implant have been observed by Bean [70] and Gable [72], as well as in the alternate dopant study of the current work. The range of the process window as described by not entirely melting the amorphous layer and over melting the crystalline substrate can be quantified by means plan-view transmission electron microscopy. The process window as described by Kuryliw begins at the laser energy density at which the PTEM diffraction pattern no loner exhibits a polycrystalline ring, and ends at the energy density prior to reduction in the regrowth related defect population [61]. In other words, the process window begins at the lowest energy density capable of melting the entire amorphous layer, thus seeding epitaxial regrowth from the crystalline substrate, and ends at the highest energy density that does not melt the crystalline substrate. Using this definition the process window is determined with respect to indium co-implant dose. For the low indium dose of $1.0x10^{14}$ /cm^2, laser energy densities of 0.70 J/cm^2 or less, result in heavily defected material with the associated diffraction pattern exhibiting a polycrystalline ring pattern (Figure 3-27). Increasing the indium dose to $5.0x10^{14}$ /cm^2, results in heavily defected material for all energy densities,

but with the polycrystalline ring being present only for the lowest laser energy density of 0.66 J/cm^2 (Figure 3-28). Further increase of the indium dose to 1.5x10^{15} /cm^2, results in no polycrystalline rings for any of the laser energy densities, and at the highest energy density the defect population is significantly reduced (Figure 3-29). For the highest indium dose of 3.0x10^{15}/cm^2, the samples are crystalline and nearly free of defects for all laser energy densities (Figure 3-30). Based on crystallinity and defect populations, the laser energy densities closest to the center of the process window for indium co-implant doses of 0.0x10^0, 1.0x10^{14}, 5.0x10^{14}, 1.5x10^{15} and 3.0x10^{15} /cm^2 are 0.74, 0.74, 0.74, 0.70 and 0.66 J/cm^2, respectively. Table 3-2 summarizes the LTP process window for the co-implantation of boron and indium as a function of indium dose, with laser energy densities closest to the center of the process window shaded in gray.

Comparison between co-implant samples in the following sections is made at identical laser energy densities. In the preceding paragraphs, dose of the indium co-implant is found to shift the range of the process window. Therefore, despite receiving the same laser energy density, samples implanted with different indium dose are not necessarily comparable in terms of the process window. Changes in the process window with respect to dose make a straight forward comparison across all indium co-implant doses difficult. Specifically, choosing to adjust the laser energy density to compensate for a shift in the process window may negate some effects of the co-implant indium dose, while not compensating may introduce effects from being outside or at the edges of the process window. Since it is not possible to decouple the effect of the indium co-implant dose from shifting the process window, the following sections compare samples and data between common laser energy densities, with attention paid to identifying and elucidating

those effects associated with shifts in the process window. The LTP Activation section presents data for all laser energy densities, but makes the primary comparisons in the text for like laser energy densities. In the Post-LTP Anneal Deactivation section, comparison of the co-implant indium dose is restricted to the laser energy density of 0.74 J/cm^2, but distinguishes between the low indium doses of $0.0x10^0$, $1.0x10^{14}$ and $5.0x10^{14}$ /cm^2, which are in the process window and high doses of $1.5x10^{15}$ and $3.0x10^{15}$ /cm^2 that exceed the process window. Additionally, the section concludes with a comparison of indium co-implant dose, using laser energy densities adjusted to achieve the respective process windows.

LTP Activation

Melt laser thermal processing incorporates dopants into the lattice during liquid phase epitaxy. The concentration of the dopants incorporated substitutionally is primarily a function of solid solubility and liquid phase epitaxy regrowth velocity, as the later affects the segregation coefficient. Of the substitutional concentration, only a fraction is electrically active. The active concentration is a function of the ionization potential of the dopant. Additionally, the mobility of the carriers, resulting from the ionization of the dopants, is a function of both the concentration of carriers and the crystalline quality of the doped layer. In short, the electrical properties of the junction are a function of the laser thermal processing conditions and the dopant species.

Electrical properties of the junctions change with respect to laser energy density. Increasing the laser energy density decreases the sheet resistance. Figure 3-33 is a plot of sheet resistance measured by Four-Point Probe after laser thermal processing at energy densities of 0.66, 0.70 and 0.74 J/cm^2. Each sample is preamorphized with a 15 keV, $1.0x10^{15}$ /cm^2 silicon implant, doped with a 1 keV, $3.0x10^{15}$ /cm^2 boron implant and co-

implanted at 5 keV with indium doses of $1.0x10^{14}$, $5.0x10^{14}$, $1.5x10^{15}$, $3.0x10^{15}$ /cm^2. As a control, one sample receives the same preamorphizing and boron implant, but no indium co-implant. For each of the four doses of indium, increasing the laser energy density decrease the sheet resistance. In the case of the control sample with no co-implanted indium, the sheet resistance values are not available for the lower laser energy densities of 0.66 and 0.70 J/cm^2.[8] Despite the lack of data, a similar trend of decreasing sheet resistance with increasing laser energy density would likely be observed for the control, as this trend is an energy density induced change in the physical properties of the junction, not a co-implantation effect. The decrease in the sheet resistance observed with increasing laser energy density is due to an increase in the carrier sheet number and or mobility. Figure 3-34 and Figure 3-35 are plots of the sheet number and mobility measured by Hall Effect after laser thermal processing at energy densities of 0.66, 0.70 and 0.74 J/cm^2. For each respective co-implant indium dose, both the sheet number and mobility increase with increasing laser energy density, resulting in a lower sheet resistance. The changes in the sheet resistance as a function of laser energy density are indicative of physical changes in the junction, and can be used as indicators of the process window [80]. At low energy densities, below the process window, the primary melt does not consume the entire amorphous layer, resulting in polycrystalline silicon. In this regime, the sheet resistance decreases dramatically with increasing energy density, due to increase in activation within increasing penetration of the melt into the doped

[8] No sheet resistance values for boron without indium are reported for the laser energy densities of 0.66 and 0.70 J/cm^2. Due to a shortage of material the lower energy densities for were bypasses in favor of the higher energy density to achieve the process window. Further comparison between the implant conditions is made primarily for the laser energy density of 0.74 J/cm^2, thus mitigating the lack of the lower energy densities.

amorphous layer. For laser energy densities that achieve the process window, the dopant dose is largely active and increasing the laser energy density results in only a small reduction in the sheet resistance. Further increasing the laser energy density improves the crystallinity [29] and eventually increasing the depth of the electrical junction, both of which continue to lower the sheet resistance due to increased carrier mobility [10, 24, 25, 60]. While electrical properties may be used as indicators of the process window, in the following analysis they are primarily used to compare the effects of indium co-implantation rather than the process window.

Electrical properties change with respect to dose of co-implanted indium. For identical laser energy densities, preamorphizing implants and boron implants, increasing the dose of the indium co-implant increases the sheet resistance. Specifically, in Figure 3-33, which is a plot of the sheet resistance as a function of indium co-implant dose after laser thermal processing, the sheet resistance increases with increasing indium dose for each respective laser energy density.[9] The increase in sheet resistance is due in part to a decrease active dopant population or sheet number. Figure 3-34 is plot of the sheet number as a function of indium dose for the three laser energy densities. An increase in the indium dose corresponds to a decrease in the sheet number. Similarly, a change in the electrical properties as a function of dose is also reported for the alternate dopants in the current work (Figure 3-14 and Figure 3-15). However, in the case of the alternate dopants, an increasing dose produces a decrease in the sheet resistance, which is congruent with a larger dopant population resulting from the increase in dose. For co-

[9] The $1.5x10^{15}$ /cm^2 dose of indium irradiated with a laser energy density of 0.66 J/cm^2 exhibits a sheet resistance much higher than the established trend in the plot. As indicated by the error bar, this high value is not due to one data flyer, but is representative of the population. The source of the phenomena is unconfirmed, but is likely due to a lower than recorded laser energy density.

implanted boron and indium, the relationship between sheet resistance and indium dose is opposite to that observed for individual implants in the alternate dopant study.

Disparity in the effect of dose on sheet resistance between alternate dopants and co-implant studies is due to the co-implantation of indium. For alternate dopants there is only one dopant species, thus an increase in dose produces a corresponding increase in sheet number, which according to Eqn. 2.9 lowers the sheet resistance. In contrast for the co-implant study, both boron and indium are implanted into the silicon wafer. As reported in the alternate dopant study, activation of a $1.5x10^{15}$ /cm^2 dose of boron by LTP results in sheet number that is two orders of magnitude greater than that for an equivalent dose of indium. Consequently, in the presence of a fixed boron dose of $3.0x10^{15}$ /cm^2, it is unlikely that increasing the indium co-implant dose to $3.0x10^{15}$ /cm^2 makes a significant contribution to the sheet number. Alternatively, while increasing the dose of indium does not contribute noticeably to the sheet number, it may change the electrical properties of the junction by reducing the activation and or mobility of boron, which would in turn lower the sheet resistance.

Increasing the indium co-implant dose increases the melt depth and the subsequent junction depth. As demonstrated in the alternate dopant section, increasing the implant dose effectively increases the laser energy density by decreasing the reflectivity (Figure 3-13). At the upper end of the process window increasing the laser energy density results in an over-melt of the crystalline substrate, which translates to a deeper junction. The depth to which the dopants are distributed after LTP is indicative of the melt depth. Depth profiles of the dopants are measured by secondary ion mass spectrometry (SIMS). Figure 3-36 is a plot of boron depth profiles measured by SIMS as a function of indium

dose after LTP at an energy density of 0.74 J/cm^2. For the control and two lower doses of indium ($0x10^0$, $1.0x10^{14}$ and $5.0x10^{14}$ /cm^2), the boron depth profiles are very similar in shape and depth distribution. Defining the junction depth at a boron concentration of $1.0x10^{18}$ /cm^3, the control and two lower doses of indium each have depths of approximately 50 nm. In contrast, increasing the indium dose to $1.5x10^{15}$ /cm^2 increases the junction depth by approximately 5 nm, while increasing the dose to $3.0x10^{15}$ /cm^2 increases the junction depth by an additional 10 nm. For the same samples, a similar trend of increasing junction depth is also observed for indium depth profiles, as plotted in Figure 3-37.[10] While different in shape than those of boron, the relative depths of the indium profiles support the finding that increasing the indium co-implant dose increases the melt depth and subsequent junction depth.

Increase in the junction depth due to over-melt does not decrease the sheet resistance. As previously reported, increasing the indium co-implant dose results in a higher sheet resistance for each respective laser energy density (Figure 3-34). In contrast, the over-melt results in a deeper junctions as measured by SIMS depth profiles of boron (Figure 3-36) with fewer defects viewable by PTEM (Figure 3-32), which should increase the carrier mobility and decrease the resulting sheet resistance. In agreement with the over-melt occurring at a laser energy density of 0.74 J/cm^2, the carrier mobility plotted in Figure 3-35 is larger for the two highest indium co-implant doses of $1.5x10^{15}$ and $3.0x10^{15}$ /cm^2 than for the lower doses. However, the increase in the mobility with increasing indium dose is over shadowed by the reduction in sheet number (Figure 3-34). Therefore, despite an increase in the junction depth and associated increase in mobility

[10] For the control sample there is not an indium SIMS depth profile in the plot. The control is not implanted with indium and therefore no indium depth profile is obtainable.

the sheet resistance increases due to a reduction in the sheet number. Based on the SIMS depth profiles in Figure 3-36 the reduction in the sheet resistance could be explained by the reduction in the plateau concentration. Assuming that boron is active up to the plateau concentrations, thus neglecting the boron in the surface peak, the integrated dose decreases from approximately $3.0x10^{15}$ /cm^2 for the control and two low indium doses to $2.0x10^{15}$ /cm^2 for the highest indium dose. Hence, the increase in sheet resistance with increasing indium dose may be due to a corresponding reduction in the plateau concentration.

The decrease in the plateau concentration and integrated dose implies that the boron pile-up at the surface increases with indium dose. As plotted in Figure 3-36, there is a distinct difference in the shape of the boron depth profiles between the low and high doses of co-implanted indium. For the control and two lower doses of indium ($0x10^0$, $1.0x10^{14}$ and $5.0x10^{14}$ /cm^2), the boron depth profiles are approximately identical, exhibiting plateau concentrations of approximately $1.0x10^{21}$ /cm^3. In contrast, the two higher co-implant indium doses of $1.5x10^{15}$ and $3.0x10^{15}$ /cm^2 exhibit lower plateau concentrations of $7.0x10^{20}$ and $5.0x10^{20}$ /cm^3, respectively. The reduction in the boron plateau concentration with increasing indium dose could be explained by the corresponding increase in the melt depth. Assuming uniform incorporation of the dopant dose, a deeper junction would result in a lower concentration. However, the increase in the junction depth is not sufficient to account for the reduction in the plateau concentration. Additionally, the boron is not uniformly distributed across the junction. For the control and two low doses of co-implant indium, the boron depth profiles gradually roll off towards the surface to a lower concentration between 4.0 and $5.0x10^{20}$

/cm^3. In contrast, the boron depth profiles for the two higher indium doses of 1.5x10^{15} and 3.0x10^{15} /cm^2 rise precipitously in concentration at the surface. The increase in the concentration at the surface for the high dose indium samples and the decrease in the concentration at the surface for the low dose indium samples are related to the respective plateau concentrations. Independent of the increasing indium dose, each sample is implanted with a fixed boron dose of 3.0x10^{15} /cm^2, which assuming conservation of the dose must be contained within the silicon sample. Incorporation of the implanted dopant atoms into the lattice occurs during liquid phase epitaxy that initiates at the internal liquid-solid interface and propagates back to the surface of the sample. Higher plateau concentration translates to an increase in the number of dopant atoms that are incorporated as a function of depth. Hence, incorporation of the dopant into the solid at high concentrations may consume the entire dose prior to the solidification front reaching the surface. With none or very little dose remaining in the melt, the concentration of the dopant incorporated into the solidifying silicon rolls off towards the surface due to depletion of the dose. In contrast, at a low plateau concentration the dose may not be entirely incorporated into the solid at the point the solidification front comes in close proximity of the surface. Therefore, in order to incorporate the surplus dose the concentration rises precipitously resulting in a pile-up at the surface. For the co-implant samples, the disparity between plateau concentrations with indium dose is indicative of a change in the segregation coefficient that may be related to the regrowth velocity.

Changes in the regrowth velocity alter the segregation coefficient and the corresponding plateau concentration. The equilibrium segregation coefficient k_o, is

defined as the ratio of the concentrations of an impurity in solution in the solid C_s and the liquid C_l phases

$$k_o = C_S / C_l \qquad \text{Eqn. 3.1}$$

as determined from the equilibrium phase diagram. In terms of equilibrium regrowth, a k_o value less than one, results in the advancing solid- liquid interface rejecting the impurity from the solid into the liquid. Hence, under equilibrium conditions a lower k_o results in a lower concentration of impurities incorporated into the solid phase or in relative terms a lower dopant plateau concentration. For a melt initiated by laser thermal processing, the regrowth by liquid phase epitaxy is not an equilibrium process, resulting in a non-equilibrium segregation coefficient *k'*. Increasing the regrowth velocity increases the segregation coefficient from the equilibrium value [32, 42, 59, 82]. Figure 1-7 plots *k'* as a function of regrowth velocity for several dopant species in silicon. In the regime of 0.0 to 1.5 m/s a slight change in the regrowth velocity results in a pronounced change in the *k'* for boron with only a slight change in the already low value of indium. Hence, in this regime a decrease in the regrowth velocity could account for the reduction in boron plateau concentrations (Figure 3-36). Additionally, within this same velocity regime the low *k'* value for indium explains the low concentrations of initial incorporation and the eventual pile-up of indium towards the surface (Figure 3-37).

Increasing the laser energy density decreases the regrowth velocity. Regrowth velocity is primarily dependant on the laser pulse duration, energy density and substrate temperature. For a similar laser pulse duration and substrate temperature Baeri et al. reported that an increase in laser energy density decreases the regrowth velocity of the melted amorphous silicon layer [83, 84]. The increase in the laser energy density

increases the melt temperature thereby reducing the super cooling and the regrowth velocity driving force. As observed in the alternate dopant section of the current work, increasing the indium dose decreases the optical reflectivity of the amorphous layer (Figure 3-13), effectively increasing the laser energy density by reducing the intensity lost to reflection. Similarly, based on PTEM analysis, increasing the dose of co-implanted indium in the presence of a fixed boron dose also effectively increases the laser energy density. The increase in the effective laser energy density with increasing dose of indium may, like observed by Baeri et al., decrease the regrowth velocity, which would correspond to a decrease in the boron plateau concentration (Figure 3-36). Ascribing a reduction in regrowth velocity to increased indium co-implant dose supports the reduction in the boron plateau concentrations measured by SIMS depth profiles, and the reduction in sheet number measured by Hall Effect.[11]

Post-LTP Anneal Deactivation

Increase in the dose of co-implanted indium suppresses the rise in sheet resistance that occurs during the post-LTP anneal. As reported in the previous section, increasing the dose of co-implanted indium results in a lower sheet number and higher sheet resistance immediately after laser thermal processing. In contrast, after a post-LTP anneal this same increase in indium dose results in a suppression of the sheet resistance. Figure 3-38 is a plot of the sheet resistance measured by Four-Point Probe for indium co-implant doses of $0.0x10^{0}$, $1.0x10^{14}$, $5.0x10^{14}$, $1.5x10^{15}$ and $3.0x10^{15}$ /cm^2 as function of annealing time at 900 ^{o}C in an ambient of nitrogen. In addition to the indium, each

[11] The effect of implant dose on the regrowth velocity and subsequent sheet number should occur for single implants discussed in the alternate dopant section. However, effect of dose on the incorporation of the dopant is not necessarily noticeable because unlike the co-implant case the sheet number is dominated by the contribution from the increasing dose.

sample is amorphized with a 15 keV, $1.0x10^{15}$ /cm^2 silicon implant, doped with a 1 keV, $3.0x10^{15}$ /cm^2 boron implant and laser annealed with an energy density of 0.74 J/cm^2. For all doses of co-implanted indium, the sheet resistance increases with annealing time. As plotted in Figure 3-39 for the control with no indium, the general increase in sheet resistance with post-LTP annealing time is due to deactivation of the carrier population, which is measured by Hall Effect as a reduction in the sheet number. The relative amount of deactivation that occurs as a function of post-LTP annealing time is reduced with increasing indium co-implant dose. Increasing the indium co-implant dose from $0.0x10^{0}$ for the control to $3.0x10^{15}$ /cm^2 corresponds to a 54 % suppression of the sheet resistance at the final post-LTP annealing time of 600 s (Figure 3-38).

Suppression of the increase in sheet resistance with increasing dose of co-implanted indium may be due to several possible sources including: electrical contribution from the indium dose, increase in junction depth, improved crystallinity, strain compensation or some combination. Increase in the dose of co-implanted indium may contribute to the suppression of the sheet resistance. As observed in the alternated dopant section, an increase in the dose of the dopant correlates to lower sheet resistance values (Figure 3-14 and Figure 3-15). The increase in the indium co-implant dose may contribution to the sheet number, thus lowering the sheet resistance. Alternatively, an increase in the junction depth may also suppress the sheet resistance. Assuming that the active dose is constant, an increase in the junction depth corresponds to a large volume over which the dopant population is distributed. A large distribution volume corresponds to a lower dopant concentration as a function of depth. A lower concentration equates to an increase in the mobility due to a reduction in scattering from the ionized impurities.

Additionally, an increase in junction depth due to over-melt can decrease the defect population, which may also increase the carrier mobility. Hence, deeper junctions may have higher carrier mobility and correspondingly lower sheet resistance values. Finally, the suppression of the sheet resistance increase with post-LTP annealing duration may be due to strain compensation. Reduction in the strain may diminish the driving force for deactivation, thus suppressing the rise in sheet resistance by maintaining a larger population of electrically active dopants.

Suppression of sheet resistance during the post-LTP anneal with increasing indium co-implant dose can not be accounted for by a contribution from electrically active indium. In the alternate dopant study, indium is implanted at 5 keV into a silicon wafer that is amorphized by a 15 keV, $1.0x10^{15}$ /cm^2 silicon implant. With no accompanying boron implant, the $1.5x10^{15}$ /cm^2 dose of indium activated by LTP results in a sheet resistance value no less than 30,000 ohms/sq during the entirety of the 300 s post-LTP anneal at 900 ^{o}C (Figure 3-23). In contrast, for a $3.0x10^{15}$ /cm^2 dose of boron, co-implantation of indium coincides with a reduction in the sheet resistance from approximately 500 ohms/sq for no indium to 200 ohms/sq for an indium dose of a $3.0x10^{15}$ /cm^2 (Figure 3-38). In terms of sheet number values, the 30,000 ohms/sq sheet resistance measured in the alternate dopant study for indium corresponds to a value of approximately $2x10^{12}$ /cm^2, which means that less than 0.2 percent of the $1.5x10^{15}$ /cm^2 implanted dose is electrically active. Assuming a similar active fraction of indium in the co-implant case, the estimated contribution to the sheet number from the $3.0x10^{15}$ /cm^2 indium dose is approximately $4x10^{12}$ /cm^2. In contrast, the difference in sheet number measured between the control ($0.0x10^{0}$ /cm^2) and the $3.0x10^{15}$ /cm^2 co-implant dose of

indium is a value of $3.3x10^{14}$ /cm^2, which is approximately two orders of magnitude greater than the contribution extrapolated from the alternate dopant data. Base on the electrical activation data for indium from the alternate dopant study, it is unlikely that increasing the indium dose to $3.0x10^{15}$ /cm^2 in the co-implant study makes a significant contribution to the boron dominated sheet number and therefore can not account for suppression of the sheet resistance occurring during the post-LTP anneal.

The depth of the junction increases with dose of the indium co-implant due to over-melt. As reported in the co-implant activation section of the current work, increasing the indium co-implant dose increases the melt depth and subsequent junction depth as measured by SIMS depth profiles of both boron and indium (Figure 3-36 and Figure 3-37). For a laser energy density of 0.74 J/cm^2, the junction depths are identical for the control and the two lower indium co-implant doses of, $1.0x10^{14}$ and $5.0x10^{14}$ /cm^2, but begin to increase due to over-melt at an indium dose of $1.5x10^{15}$ /cm^2. The over-melt occurring for the two higher co-implanted indium doses of $1.5x10^{15}$ /cm^2 and $3.0x10^{15}$ /cm^2, result in a junction depths that increase by 5 and 15 nm respectively, over that of the three lower indium doses.

The increase in the junction depth due to an indium co-implant dose induced increase in the melt depth is exacerbated by the post-LTP anneal. The post-LTP anneal provides the thermal budget for diffusion. Diffusion occurring during the post-LTP anneal causes the dopant junctions to become deeper. Figure 3-40 is a plot of the boron depth profiles measured by SIMS as a function of indium co-implant dose after a post-LTP anneal at 900 ^{o}C for 600 s. The post-LTP anneal increases the disparity between the depth of boron junctions associated with the low doses of co-implanted indium, which do

not induce an over-melt, and the higher doses that do result in an over-melt. In terms of indium co-implant dose, diffusion of the boron during the post-LTP anneal is larger for the two highest doses. Defining the junction depth at a boron concentration of $1.0x10^{18}$ /cm^3, the control and two low doses of co-implanted indium ($0.0x10^0$, $1.0x10^{14}$ and $5.0x10^{14}$ /cm^2) correspond to similar boron junction depths of approximately 112 nm. In contrast, increasing the indium co-implant dose to $1.5x10^{15}$ and $3.0x10^{15}$ /cm^2, corresponds to junction depths that are respectively 18 and 23 nm deeper than those of the control and two low doses. Prior to the post-LTP anneal the same increase in indium co-implant dose corresponded to an increase in junction depth of only 5 and 15 nm. Hence, not only does the co-implanted indium induce an over-melt at higher doses that increases the junction depth, but the disparity in junction depth increases after the post-LTP anneal.

Increase in the indium co-implant dose corresponds to an increase in the boron clustering concentration. During the post-LTP anneal, the boron population above a critical concentration forms clusters. Boron interstitial clusters or BIC's are submicroscopic and are composed of both silicon self interstitials and boron atoms. The clusters form during thermal processing when there is high local concentration of substitutional boron and interstitials [85]. The resulting boron clusters are immobile and electrically inactive [85, 86]. In contrast, the boron population below the critical concentration necessary to form the clusters is active and mobile. Hence, the boron population below the clustering concentration diffuses during annealing forming a diffused shoulder. The concentration of the diffused shoulder is characterized by SIMS depth profiles of boron. Figure 3-40 is a plot of SIMS depth profiles for boron as a

function of indium co-implant dose measured after the post-LTP anneal. A diffusion shoulder in the boron profile occurs for all the doses of co-implanted indium. However, the concentration at which the shoulder occurs differs between the low and high doses of co-implanted indium. For the control and low co-implanted indium doses of $1.0x10^{14}$ and $5.0x10^{14}$ /cm^2 the diffused shoulder occurs at a concentration of approximately $6.0x10^{19}$ /cm^3, while for the two higher doses of $1.5x10^{15}$ and $3.0x10^{15}$ /cm^2 the shoulder concentration of is closer to $1.0x10^{20}$ /cm^3. Between the low and high doses of co-implanted indium the diffused boron shoulder, which is indicative of the clustering concentration, increases by a factor of approximately two. Hence, increasing the indium co-implant dose increases the boron clustering concentration.

Increase in the indium co-implant dose corresponds to an increase in the electrically active dose and reduction in the sheet resistance. The electrically active dose is measured by Hall Effect and reported as sheet number. Figure 3-41 is a plot of the sheet number and corresponding sheet resistance as function of indium co-implant dose measured after the 600 s post-LTP anneal at 900 ^{o}C, for junctions originally activated by a laser energy density of 0.74 J/cm^2. The increase in sheet number with increasing indium co-implant dose corresponds to lower sheet resistances. For a $3.0x10^{15}$ /cm^2 dose of co-implanted indium the resulting sheet number is $7.1x10^{14}$ /cm^2, compared to a value of $4.2x10^{14}$ /cm^2 for control that is not implanted with indium. For the two highest doses of co-implanted indium, the increase in the sheet number is approximately the same, and results in a 77 % increase over that of the control. In contrast, for the two lower indium doses, for which over-melt does not occur, the sheet number increases with increasing indium co-implant dose, resulting in a maximum increase over that of the control of 16 % at an indium dose

of $5.0x10^{15}$ /cm^2. The difference in the sheet number between the high and low dose regimes is due to an over-melt induced increase in the junction depth and boron clustering concentration. Calculating the sheet number by integrating the boron SIMS depth profiles below the respective clustering concentrations elucidates the contribution of the over-melt. Figure 3-40 is plot of the SIMS depth profiles for boron after the post-LTP anneal. The boron clustering concentrations for the indium co-implant dose of $0.0x10^0$ (control), $1.0x10^{14}$, $5.0x10^{14}$, $1.5x10^{15}$ and $3.0x10^{15}$ /cm^2 are approximately $5.6x10^{19}$, $5.8x10^{19}$, $6.0x10^{19}$, $1.1x10^{20}$, and $1.2x10^{20}$, respectively. Assuming that only boron below the clustering concentrations is active, the integrated boron depth profiles for the control and highest indium co-implant dose of $3.0x10^{15}$ /cm^2 result in sheet numbers of $4.0x10^{14}$ and $8.6x10^{14}$ /cm^2, respectively.[12] The sheet numbers calculated for the control and highest dose of co-implanted indium using the SIMS depth profiles are in qualitative agreement with the respective values of $4.2x10^{14}$ and $7.1x10^{14}$ /cm^2 measured by Hall Effect. The sheet number values calculated using SIMS depth profiles and those measured by Hall Effect are plotted in Figure 3-42 as a function for indium co-implant dose. The sheet number values calculated from SIMS depth profiles are only a function of junction depth and boron clustering concentration that are determined by the melt conditions; therefore the large increase in sheet number between indium co-implant doses of $5.0x10^{14}$ and $1.5x10^{15}$ /cm^2 is due to over-melt. Specifically, the 77 % increase in sheet number, as measured by Hall Effect, for the high doses of co-implanted indium is primarily due to the increase in junction depth and boron clustering concentration

[12] The active dose is calculated in two parts. At concentrations above respective clustering concentration the dopants are inactive so until the concentration drops below this value the carrier concentration is assumed to be constant. When the concentration falls below the respective clustering concentrations, the SIMS profile is integrated. The doses from both regions are added to yield the total active dose.

associated with over-melt. In contrast, despite having junction depths approximately equal to that of the control, suggesting no over-melt, the two low indium co-implant doses of $1.0x10^{14}$ and $5.0x10^{14}$ /cm^2 correspond to an increase in the sheet number measured by Hall Effect up to 16 % over that of the control. The increase in sheet number with increasing indium co-implant dose contributes to a decrease in the sheet resistance (Figure 3-41). Hence, the suppression in the sheet resistance for the two high dose of co-implanted indium is primarily due to dose induced over-melt; however the for the two low doses, the sheet resistance is still suppressed below that of the control despite the lack of any over-melt. The source of the increase in sheet number for the two low doses of co-implanted indium over that of the control is addressed later in the current section.

Increase in the sheet number with increasing indium co-implant dose can not account for the entire sheet resistance suppression during the post-LTP anneal. As plotted in Figure 3-41, increasing the indium co-implantation dose from $0.0x10^{0}$ for the control to $3.0x10^{15}$ /cm^2 results in a 1.7 factor increase in the sheet number. Based on Eqn. 2.9, if the sheet number is the sole factor influencing the sheet resistance the increase in sheet number with increasing indium co-implant dose should decrease the sheet resistance by an equivalent factor. However, over the same co-implant doses the sheet resistance plotted in Figure 3-41 decreases from 475 to 218 ohms/sq, which is a reduction by a factor of approximately 2.2. Based on the disparity between the two factors, the increase in sheet number with increasing indium co-implant dose can not account for the entire suppression of the sheet resistance.

Increases in the carrier mobility with indium co-implant dose accounts for the remainder of the sheet resistance suppression occurring during the post-LTP anneal. According to Eqn. 2.9, sheet resistance is the reciprocal of the product of the carrier charge, sheet number and mobility. The carrier charge is a constant and as previously shown the effect of co-implantation on the sheet number does not account for the entirety of the sheet resistance suppression; hence the remainder must be due to mobility. Figure 3-43 is a plot of mobility and sheet resistance as a function of the indium co-implant dose after the post-LTP anneal. An increase in the co-implant indium dose from $0.0x10^{0}$ for the control to $3.0x10^{15}$ /cm^2 results in an increase of the mobility from 31 to 40 cm^2/V*s, which is approximately a factor of 1.3 increase. The product of the 1.7 factor increase in the sheet number and the 1.3 factor increase in the mobility results in a 2.2 factor reduction in the sheet resistance. In summary, the suppression of the sheet resistance during the post-LTP anneal as a function of increasing indium co-implant dose is the result of contributions from increased sheet number and carrier mobility.

Increase in the carrier mobility is due to reduction of the carrier scattering mechanisms associated with electrical transport. For nonpolar semiconductors like silicon the mobility is affect by carrier scattering resulting primarily from ionized impurities and acoustic phonons.[13] Ionized impurities (i.e., electrically active dopants) act as scattering cites for carriers, thus mobility decreases with increasing carrier concentration. Acoustic phonons are thermally excited lattice vibrations that scatter the carriers, consequently increasing the temperature increases the scattering and decreases the mobility. In addition to the scattering mechanisms discussed above, mobility can be

[13] Mobility is also affect by the conductivity effective mass *m**, which differs with respect to carrier type. Base on *m** electrons have a higher mobility than holes for p-type dopants.

degraded by scattering from lattice defects. In general the contribution from defect scattering is small for crystalline silicon, but for high defected silicon the contribution becomes larger. In the case of the indium co-implanted samples, the mobility increases with ionized impurity concentration or sheet number as reported in Figure 3-44. The concomitant increase in of mobility and sheet number implies that ionized impurities are not the dominate scattering mechanism, as an increase in sheet number should decrease the mobility. Additionally, all samples were measured at a room temperature, so the acoustic phonon contribution to scattering should be similar between samples. Therefore, in terms of scattering mechanisms, the increase in mobility is likely due to a reduction in scattering occurring from defects in the crystalline lattice. Defects in the silicon lattice are imaged by plan-view transmission electron microscopy. Figure 3-45 contains PTEM micrographs of indium co-implanted samples after the post-LTP anneal at 900 ^{o}C for 60 s. Prior to the post-LTP anneal the samples were irradiated with a laser energy density of 0.74 J/cm^2. With increasing indium co-implant dose the crystallinity of the silicon improves, as signified by a reduction in the defect population. The trend of improving crystallinity with increasing indium co-implant dose occurs prior to the post-LTP anneal and traces back to the dose effect on the process window. Increasing indium dose increases the depth of the laser induced melt and subsequent junction depth as defined by the SIMS depth profiles of the dopants (Figure 3-36 and Figure 3-37). Increasing the melt depth initially improves the quality of the liquid phase epitaxy, thus reducing the number of regrowth related defects. Progression of the melt further into the crystalline silicon consumes the end-of-range damage, which would have contributed to the defect population after the post-LTP anneal. Hence, a shift in the process window with indium

co-implant dose results in a reduction in the defect population. The effect of the indium co-implant dose on the defect population after LTP at an energy density of 0.74 J/cm^2 is imaged in Figure 3-32. The disparity in defect population after LTP perpetuates during the post-LTP anneal, resulting in a decrease of the defect population with increasing indium co-implant dose. Attributing the increase in mobility to a reduction in the defect population is in part supported by the data. The most significant reduction in the defect population after the post-LTP anneal is co-incident with the over-melt that occurs for the two highest indium co-implant doses of 1.5x10^{15} and 3.0x10^{15} /cm^2. For the two high doses of indium the reduction in the defect population corresponds to a 31 % reduction in the mobility (Figure 3-43), which supports the argument for defect dominated scattering. For the lower dose of 1.0x10^{14} and 5.0x10^{14} /cm^2, the disparity in defect population is not as pronounced, but the mobility is still increased by a maximum of 16 % over that of the control with increasing dose. Based on the PTEM data, it is likely that the improvement in mobility for the two high doses of indium is due to over-melt and the associated reduction in the defect population.

Over-melt induced by the indium co-implant dose accounts for a large portion of the post-LTP anneal suppression of the sheet resistance. Figure 3-46 is a plot of the sheet resistance as a function of indium co-implant dose measured by Four-Point Probe after LTP at an energy density of 0.74 J/cm^2 and again after the 900 ^{o}C post-LTP anneal for 600 s. For all doses the sheet resistances are higher after the post-LTP anneal due to deactivation, but decrease in value with increasing indium co-implant dose. For the high indium co-implant doses of 1.5x10^{15} and 3.0x10^{15} /cm^2, the suppression of the sheet resistance corresponds to over-melt of the crystalline substrate. As demonstrated by

SIMS depth profiles of the dopant species after LTP (Figure 3-36 and Figure 3-37), the transition to the over-melt regime occurs between the doses of $5.0x10^{14}$ and $1.5x10^{15}$ /cm^2. Hence, of the 53 % reduction in the sheet resistance with increasing indium co-implant dose, only the 23 % that occurs for the two low doses of $1.0x10^{14}$ and $5.0x10^{14}$ /cm^2 can be decoupled from over-melt phenomena. The suppression of the post-LTP sheet resistance with increasing indium co-implant dose is due to an increase in sheet number (Figure 3-41) and carrier mobility (Figure 3-43). Over-melt associated with high doses of co-implanted indium increases both sheet number and mobility. For the high doses of co-implanted indium that induce over-melt, the sheet number increases due to a simultaneous increase in the junction depth and cluster concentration, while the mobility increases due to a reduction in the defect population.

For over-melt doses, the increase in the sheet number is primarily due to an increase in the clustering concentration rather that an increase in the junction depth. Increasing the co-implant indium dose increases the depth of the dopant profiles and the clustering concentrations, both of which contribute to a lower post-LTP anneal sheet resistance. Junction depth and sheet resistance are inversely related, meaning that a lower sheet resistance can be achieved at the expense of increased junction depth (Figure 1-4). It is therefore consistent that the increase in junction depth, due to the indium induced over-melt and the concentration–dependant diffusion [87] occurring during the post-LTP anneal, results in lower sheet resistance values. However, in the over-melt regime the suppression in the sheet resistance due to increased sheet number is only partially accounted for by the increase in junction depth. Removing the over-melt affect on the clustering concentration by assuming that the clustering concentration is fixed at

$6.0x10^{19}$ /cm^3 for all doses of indium, the increase in junction depth from the shallowest to the deepest junction would only increase the integrated active dose from $4.2x10^{14}$ to $5.0x10^{14}$ /cm^2, in comparison to $8.6x10^{14}$ /cm^2 when the effect of boron clustering concentration is included. Therefore, of the difference in the sheet number calculated from the boron SIMS depth profiles; only 18 % is from the increase in junction depth, with the remainder resulting from the difference in the clustering concentration. Hence, an indium dose induced over-melt does suppress the sheet resistance, but only a fraction of the sheet number contribution is from the junction being physically deeper.

The increase in the boron clustering concentration is due to over-melt. Formation of the boron clusters require a high local concentration of substitutional boron and silicon self interstitials [85]. Too few interstitials diminishes the likelihood of boron cluster formation. For amorphizing cases, the interstitials from the end-of-range contribute to boron cluster formation [88]. During over-melt, induced by high doses of co-implanted indium, the end-of-range damage created by the preamorphizing implant is consumed by the encroaching melt front, thus reducing the interstitial concentration. Reduction in the interstitial concentration with over-melt is supported by PTEM micrographs of the junctions after LTP. Interstitials in the end-of-range also form defects, with fewer interstitials forming fewer defects. As plotted in Figure 3-32, the defect concentration diminishes significantly between the indium co-implant doses of $5.0x10^{14}$ and $1.5x10^{15}$ /cm^2. Based on the PTEM micrographs, over-melting into the end-of-range region reduces the interstitial population that contributes to the formation of boron clusters. Fewer boron clusters, translates to a reduction in the boron population that clusters as

observed by an increase in the cluster concentration. Hence, over-melt reduces the end-of-range damage and correspondingly increases the clustering concentration.

Low doses of co-implanted indium have an effect on the sheet resistance despite not resulting in an over-melt. The term low doses, refers to the control sample that is not implanted with indium and to the indium co-implanted doses of $1.0x10^{14}$ and $5.0x10^{14}$ /cm^2. The term high doses is reserved for the indium co-implant dose of $1.5x10^{15}$ and $3.0x10^{15}$ /cm^2, which result in over-melt at the laser energy density of 0.74 J/cm^2. As plotted in Figure 3-36, the SIMS depth profiles of boron after LTP at an energy density of 0.74 J/cm^2 exhibit similar junction depths for the indium co-implant doses of $1.0x10^{14}$ and $5.0x10^{14}$ /cm^2 to that of the control. Additionally, after the post-LTP anneal at 900 ^{o}C for 600 s the low doses of co-implanted indium do not show any increase in junction depth or boron clustering concentration over that of the control (Figure 3-40). Based on the SIMS depth profiles, the low doses of co-implanted indium do not exhibit an over-melt or associated phenomena with respect to the control. However, despite exhibiting similar SIMS depth profiles after the post-LTP anneal to that of the control, the low indium co-implant doses of $1.0x10^{14}$ and $5.0x10^{14}$ /cm^2 still correspond to a suppression of the sheet resistance over that of the control. Figure 3-46 is a plot of the sheet resistance as a function of indium co-implant dose measured by Four-Point Probe after LTP at an energy density of 0.74 J/cm^2 and again after the 900 ^{o}C post-LTP anneal for 600 s. The decrease in sheet resistance after the post-LTP anneal with increasing indium co-implant dose is not linear. For the two low doses of co-implanted indium, the small change in dose corresponds to precipitous decrease in sheet resistance compared to the almost stagnate values for the two high doses. Specifically, the sheet resistance decreases

from a value of 475 ohms/sq for the control with no co-implanted indium to 417 ohms/sq for an indium co-implant dose of $1.0x10^{14}$ /cm^2, which is approximately a factor of 1.14 suppression of the sheet resistance. Further increasing the indium co-implant dose by a factor of five to $5.0x10^{14}$ /cm^2 decreases the sheet resistance to 365 ohms/sq, which is a reduction of a factor of 1.3 over that of the control. In contrast, while the onset of over-melt between the indium doses of $5.0x10^{14}$ and $1.5x10^{15}$ /cm^2 introduces a 2.2 factor of reduction in the sheet resistance over that of the control, within the over-melt regime, a doubling of the co-implanted indium dose from $1.5x10^{14}$ to $3.0x10^{15}$ /cm^2 does not reduce the sheet resistance. Neglecting the onset of over-melt, the low doses of co-implanted indium have a more pronounced effect on the sheet resistance as a function of dose. For the low dose samples, the source of the sheet resistance suppression with increasing indium co-implant dose is not a result of over-melt or associated phenomena, thus allowing an alternate explanation such as strain compensation.

Strain Compensation

Strain-compensation may be responsible for the reduction in deactivation during the post-LTP anneal. Dopant atoms incorporated substitutionally in the lattice introduce strain. The amount of strain that is introduced to the lattice is dependant on the relative size of the dopant atom to that of the lattice atoms and the concentration. In the case of melt laser thermal processing, dopants are incorporated into the lattice to concentrations in excess of equilibrium solid solubility. The large concentration of substitutional dopant atoms produces a corresponding strain. The strain is not energetically favorable, and during a post-LTP anneal the dopants are rejected from the lattice, thus diminishing the population of electrically active dopants in a process termed deactivation. Hence, reducing the strain in the lattice prior to the post-LTP anneal may diminish the driving

force for deactivation. Co-Implantation is a process that utilizes two dopants, which introduce strain of opposite type to the lattice, potentially reducing the total strain and the driving force for deactivation during the post-LTP anneal.

Strain introduced by the solute impurity is a factor limiting solid solubility and a potential driving force for deactivation. W. Hume-Rothery determined that solubility of an impurity in a solid solution is affected by four factors, one of which is the relative atomic diameters of the solute impurity to the that of the solvent [49]. For all other factors being equal, a larger difference between the atomic diameters of solute and solvent atoms results in a lower solid solubility of the solute. Fundamentally the relationship between solid solubility and disparity in atomic diameters of the solute and solution is explained by strain. Differences in atomic diameters translate into differences in covalent bonding radii and lattice parameters, subsequently, a disparity in lattice parameters between solute and solvent results in lattice strain. Strain is the distortion of physical dimensions in conjunction with a stress. Stress is a force per unit area. Hence, large disparities between solute and solvent atomic diameters are prohibitive due to the increased lattice strain and associated stress. At sufficiently large strains the associated stress is unsustainable and the solute is not incorporated, rather it is rejected from the solution resulting in a lower solid solubility. Laser thermal processing can incorporate dopants into the lattice in excess of solid solubility due to the non-equilibrium nature of the liquid phase epitaxy. The increase in the substitutional dopant concentration results in a proportional increase in the strain. Increase in the strain provides a potential driving force for deactivation during subsequent post-LTP annealing.

Substitutional boron introduces a tensile strain into the silicon lattice. Boron atoms incorporated substitutionally in a silicon lattice have smaller covalent bonding radii than silicon atoms, thus the periodic spacing between atoms or lattice parameter of the doped layer is reduced to account for the mismatch between the radii of the boron and silicon atoms [51]. For a doped layer that is thin and coherent (i.e. epitaxial), the in-plane lattice parameter is constrained to that of the silicon substrate, a_{Si} = 5.431 Å while the out-of-plane lattice parameter, $a_{\perp}$, is allowed to distort [50]. Therefore, in the case of a shallow implant of boron into silicon, $a_{\perp}$ decreases in order to compensate for the in-plane tensile stress. Changes in $a_{\perp}$ are measured by High Resolution X-Ray Diffraction two-theta omega (HR-XRD 2θ–ω) rocking curve scans symmetric about the (004) silicon reflection. Figure 3-47 is a plot of HR-XRD rocking curve data as a function of the two-theta angle, taken after LTP at a laser energy density of 0.74 J/cm^2 for a preamorphized sample implanted with a 3.0x10^{15} /cm^2 dose of boron without co-implanted indium (control). The scan consists of a narrow, intense peak centered at 69.196 ^{o} from the silicon substrate and a broad satellite peak of lower intensity from the boron doped layer. Peaks are the result of coherent diffraction of x-rays by the lattice according to Bragg's law,

$$n \cdot \lambda = 2 \cdot d_{hkl} \cdot \sin(\theta) \qquad \text{Eqn. 3.2}$$

where n is an integer, λ is the wavelength of the Cu $K_{\alpha 1}$ radiation (1.5405 Å), d_{hkl} is the interplanar spacing of planes with Miller indices of h, k and l, and θ is the angle between the incident beam and the lattice planes. Intensity of the peaks is a function of thickness and crystalline quality. A thicker layer has a larger diffraction volume, thus increasing the number of x-rays diffracted by the layer and detected as intensity. Improved

crystallinity increases the peak intensity by reducing losses occurring from non-coherent diffraction and diffuse scattering. Additionally, improved crystallinity of the layer also narrows the breadth or full-width-half-maximum of the peak. In contrast, misalignments of the crystalline lattice, associated with poor crystallinity, allow coherent diffraction at additional angles resulting in broadening of the peak. The angular position of the peak as expressed in Eqn. 3.2 is a function of d_{hkl}. For crystalline structures having cubic symmetry, like silicon, d_{hkl} is related to $a_{\perp}$ by

$$d_{hkl} = \frac{a}{\sqrt{h^2 + k^2 + l^2}} \qquad \text{Eqn. 3.3}$$

Based on Eqn. 3.2 and Eqn. 3.3, layers with smaller interplanar spacing than the substrate correspond to a diffraction peak at larger two-theta angles than the substrate peak, as is the case for the boron implanted silicon layer. The boron satellite peak is located at a two-theta position of approximately 69.92 ^{o}, which corresponds to a $a_{\perp}$ value of 5.37 Å. Strain associated with change in the out-of-plane lattice parameter is classically described by [56],

$$\varepsilon_{\perp} = \frac{a_{\perp} - a_{Si}}{a_{Si}} = \frac{\Delta a}{a} \qquad \text{Eqn. 3.4}$$

Alternatively, assuming that the in-plane lattice parameter is constrained by the substrate, the strain for each co-implant dose can be estimated using the pseudomorphic lattice growth mismatch formula [58, 89],

$$\frac{\Delta a}{a} = \left[\frac{C_{11}}{C_{11} + 2 \cdot C_{12}}\right] \cdot \left(\frac{\Delta d}{d}\right) \qquad \text{Eqn. 3.5}$$

where $\Delta a/a$ is the derivative of the alloy lattice constant, $\Delta d/d$ is the derivative of the lattice expansion in the direction normal to the surface, and C_{11} and C_{12} are the second

order elastic moduli of Si. The values of second order moduli are reported as 16.577×10^{11} dyn/cm^2 for C_{11}, and 6.39×10^{11} dyn/cm^2 for C_{12}. Appling the pseudomorphic lattice mismatch formula, the out-of-plane strain associated with the displacement of the boron satellite peak in Figure 3-47 is calculated as 0.516 %. Strain resulting from boron is tensile [50], as boron causes an increase in the two-theta position of the satellite peak that translates to reduction in the lattice parameter. Conversely, silicon implanted with species which produce an increase in the parameter, such as indium or germanium [55, 58, 90], result in peaks at angles lower than that of the silicon peak, which correspond to a compressive strain.

Co-implantation of indium reduces the strain introduced to the silicon lattice by substitutional boron. Strain compensation of highly boron doped silicon by simultaneously incorporation/doping with a larger atomic species like germanium has been demonstrated for laser [72] and non-laser processing techniques [53-55]. In contrast, strain compensation of silicon has not been demonstrated for a low solid solubility, non-isovalent species like indium. Figure 3-48 is a plot of HR-XRD rocking curves measured after LTP for boron and indium co-implanted silicon. The boron is implanted at a single dose of 3.0×10^{15} /cm^2, while the indium is implanted at doses of 0.0×10^{0}, 1.0×10^{14}, 5.0×10^{14}, 1.5×10^{15} and 3.0×10^{15} /cm^3. The vertical lines on the plot identify the two-theta position of the respective satellite peaks. As a function of increasing co-implanted indium dose, the satellite peaks associated with the strained implanted layers shift towards the peak for the silicon substrate. Not only do the satellite peaks shift with increasing indium dose, but also increase in intensity and decrease in breadth due to improved crystallinity and increased depth of the layer. Both improved

crystallinity and increased depth of the doped layer are due to the affect of indium co-implant dose on the process window, with the higher doses causing an over-melt that increases the junction depth and reduces the defect population after LTP (Figure 3-32). The shifting of the boron satellite peak towards the substrate peak with increasing indium co-implant dose confirms that co-implantation of indium is producing a strain compensating effect. Figure 3-49 is a plot of the strain as a function of indium co-implant dose, as calculated using the pseudomorphic lattice growth mismatch formula in conjunction with the HR-XRD rocking curves. Co-implantation of indium reduces the strain in the implanted layer from 0.516 % for control sample with boron alone, to 0.340 % for a 5.0×10^{14} /cm^2 dose of co-implanted indium. In the over-melt regime the strain is further reduced to 0.195 for a 3.0×10^{15} /cm^2 dose of indium.

Stain in a co-doped layer is a function of the respective dopant concentrations. Strain in terms of doping concentration was presented in the introduction chapter, but is now reviewed for convenience to the reader. In the range of purely elastic lattice distortion (i.e., no misfit dislocations), the strain in the doped layer ε is a linear function of the dopant concentration C [91]

$$\varepsilon = \beta_B \cdot C_B + \beta_{In} \cdot C_{In} \qquad \text{Eqn. 3.6}$$

where β is the lattice contraction coefficient of the respective impurity in the lattice of interest. Based on a linear model β is calculated by [52]

$$\beta = \left[1 - \frac{r_{dopant}}{r_{Si}} \right] \cdot \frac{1}{N} \qquad \text{Eqn. 3.7}$$

where r_{dopant} and r_{Si} are the covalent radii of the dopant and silicon atoms, respectively, and N is the atomic density of crystalline silicon (5.0×10^{22} /cm^3). Substituting the covalent bonding radii for boron and indium (r_B = 82 pm, r_{Si} = 111 pm and r_{In} = 144 pm)

into Eqn. 3.7 yields the lattice contraction coefficients of 5.2×10^{-24} and -5.92×10^{-24} /cm^3, respectively. Assuming that the average concentration of substitutional boron is approximately equal to the respective plateau boron concentrations (Figure 3-36), and that the average indium concentration is the taken at the depth half way between the surface and melt depth peaks (Figure 3-37), the strain produced by the co-doped layer may be calculated using Eqn. 3.6. For the control sample without any co-implanted indium, the stain calculated based on the substitutional concentration and lattice contraction coefficient for boron is approximately 0.512 %, which is in agreement with the value of 0.516 % calculated for the same implant conditions using the pseudomorphic lattice mismatch formula. Figure 3-50 is a plot of the strain calculated using the pseudomorphic lattice mismatch formula as well as the product of the dopant concentration and lattice contraction coefficient. The strain calculated by both expressions decreases with increasing indium co-implant dose, providing additional support for the argument that co-implantation of indium is compensating the tensile strain introduced by the boron implant. However, the strain values calculated using the pseudomorphic lattice mismatch formula exhibit a more precipitous decrease at the lower indium co-implant doses of 1.0×10^{14} and 5.0×10^{14} /cm^2 than do the values calculated using the lattice contraction coefficient. The disparity between the values calculated using the two different expressions is due to the fact that Eqn. 3.6 is a linear approximation as function of doping concentration, which does not account for distortions in the lattice that are not purely elastic. In contrast, strain values calculated using the pseudomorphic lattice mismatch formula are semi-empirical, resulting from differences in the satellite peak positions as measured by HR-XRD rocking curves.

Based on the negative offset of the semi-empirical data from that of the linear approximation (Figure 3-50), it is likely that there are two contributions to strain reduction for the low doses of co-implanted indium. The first contribution is from the product of the dopant concentration and lattice contraction coefficient, which increases linearly with increasing indium co-implant dose for all samples. The second contribution is potentially a defect assisted strain relaxation, which only occurs for the low doses of co-implanted indium. Figure 3-32 consists of PTEM micrographs taken after the post-LTP anneal as a function of indium co-implant dose. The additional reduction in the strain at lower doses of co-implanted indium correlates to a large defect population, where as at higher doses there is no deviation or significant defect population. Hence, the deviation of the semi-empirical values from the linear reduction in strain with increasing indium co-implant dose is likely due to defect assisted strain relaxation.

Co-implanted indium does not make a significant contribution to the sheet number after the post-LTP anneal. The indium concentrations responsible for the strain compensation after LTP are altered during the post-LTP anneal. Figure 3-51 is a plot of the indium SIMS depth profiles after LTP and again after the 900 ^{o}C for 600 s post-LTP anneal. Assuming that the indium after the post-LTP anneal is substitutional up to a concentration of $1.0x10^{19}$ /cm^3 for the $5.0x10^{14}$ /cm^2 dose, it could not account for the corresponding change in the sheet number. The concentration of substitutional indium that is electrically active can be determined by iteratively solving the charge neutrality equation.[14] For a nondegenerate p-type extrinsic semiconductor the charge neutrality equation is

[14] The charge neutrality equation was previously solved in the introduction for n-type semiconductors, but for the readers convenience is now solved for p-type semiconductors.

$$N_C \cdot e^{-(E_C - E_f)/k_B \cdot T} = N_V \cdot e^{-(E_C - E_f)/k_B \cdot T} - \frac{N_A}{1 + 4 \cdot e^{-(E_f - E_A)/k_B \cdot T}} + N_D \qquad \text{Eqn. 3.8}$$

where N_C and N_V are the effective density of states in the conduction and valence bands, while N_D and N_A are the donor and acceptor impurity densities, respectively. Additionally, E_C is the energy level of the conduction band, E_A is the ionization energy of the acceptor impurity, and E_f is the Fermi energy level, while k_B is the Boltzman constant and T is the temperature (298 K). For silicon the values of N'_C and N'_V are 2.75x10^{19} and 128x10^{19} /cm^3, respectively. For a p-type impurity in an n-type bulk, N_D is the background doping concentration, which is defined as 1.0x10^{17} /cm^3. At doping concentrations greater than 1.0x10^{19} /cm^3 the semiconductor becomes degenerate, resulting in narrowing of band gap. To account for the narrowing of the band gap at high doping concentrations it is necessary to adjust E_C as function of acceptor impurity density N_A

$$E_C = 1.1 - 0.009 \cdot \left(\ln\left(N_A / 1.0x10^{17} \right) + \sqrt{\ln\left(N_A / 1.0x10^{17} \right)^2 + 0.5} \right) \qquad \text{Eqn. 3.9}$$

Substituting Eqn. 3.9 into Eqn. 3.8 for E_C along with a value of 0.16 eV for the E_A of indium, N_A and E_f can be calculated simultaneously by iteratively solving Eqn. 3.8 for a value of zero. For the indium co-implant dose of 5.0x10^{14} /cm^3, the corresponding substitution concentration after the post-LTP anneal is approximated as 1.0x10^{19} /cm^3, which translates to an electrically active concentration of approximately 2.3x10^{18} /cm^3. Adjusted for the depth of the indium junction after the post-LTP anneal (45 nm), the contribution from electrically active indium results in a sheet number of approximately 1.0x10^{13} /cm^2, which is less than a sixth of the disparity in sheet number as measured by Hall Effect between the control (4.29x10^{14} /cm^2) and the 5.0x10^{14} /cm^2 dose of co-

implanted indium ($4.97x10^{14}$ /cm^2). Additionally, the calculation generously assumed a substitutional indium concentration an order of magnitude greater than the equilibrium solid solubility limit. The actual soluble concentration of indium in silicon after the post-LTP anneal and resulting sheet number are likely much lower. Hence, within the low dose regime, the suppression of the sheet number with increasing indium co-implant does can not be accounted for by a contribution from electrically active indium.

Compensation of strain with increasing indium co-implant dose correlates to the suppression of the sheet resistance. Figure 3-52 is a plot of the sheet resistance values measured by Four-Point Probe after the post-LTP anneal, and the lattice strain measured after LTP by HR-XRD rocking curve analysis as a function of the indium co-implant dose. For the low doses of co-implanted indium, both the strain and the sheet resistance decrease proportionally, supporting the argument for strain compensation as the source of suppression of sheet resistance during the post-LTP anneal.

Suppression of sheet resistance with increasing strain compensation is the product of reduced deactivation and increased carrier mobility with increasing indium co-implant dose. Figure 3-53 is a plot of the carrier mobility values measured by Hall Effect after the 900 ^{o}C post-LTP anneal against the corresponding tensile strain for each indium co-implant dose. Below the over-melt regime, increasing the indium co-implant dose correlates to an increase in the carrier mobility, resulting in a maximum increase of 12 % over that of the control for an indium co-implant dose of $5.0x10^{14}$ /cm^2. However, based on PTEM micrographs of the same samples in Figure 3-32, the source of the increase in the mobility can be argued as a reduction in the defect population with increasing indium co-implant dose. Conceding for the sake of argument that the enhancement of the carrier

mobility as a function of increasing indium co-implant dose is due to an associated reduction in the defect population, there still remains a reduction in the deactivation of the carrier population that corresponds to the increase in strain compensation measured after LTP.

Suppression of the carrier deactivation during the post-LTP anneal corresponds to a reduction in strain. Figure 3-54 is a plot of the sheet number values measured by Hall Effect as a function of tensile strain in the doped layer for each indium dose. The sheet number increases with decreasing strain. Within the low dose regime, the maximum improvement in the sheet number over that of the control is 16 %, and occurs at an indium co-implant dose of $5.0x10^{14}$ /cm^2. Higher sheet number values after the post-LTP anneal correlate to a reduction in deactivation. Calculated as the difference between the sheet number values measured before and after the post-LTP anneal, the percent deactivating is plotted in Figure 3-55. The deactivation decreases with increasing indium dose. For the low dose regime, which spans from the control with no indium to a dose of $5.0x10^{14}$ /cm^2, it was concluded previously in the study that the increase in sheet number was not the result of an electrical contribution from indium or a dose effect on the junction depth. Alternatively, based on the correlation between the increase in strain compensation and the decrease in deactivation, the suppression of the sheet resistance is due to co-implantation of indium. Thus, demonstrating for the first time that deactivation of metastable boron can be reduced by co-implantation of indium.

Ageing

Co-implantation of indium alters the optical, physical and electrical properties of the junction. Increasing the indium co-implant dose decreases the optical reflectivity, which for a common laser energy density produces a shift in the process window. For the

preamorphizing and boron implants used in the current study a laser energy density of 0.74 J/cm^2 results in an over-melt of the amorphous layer at higher indium co-implant dose of 1.5x10^{15} and 3.0x10^{15} /cm^2. The over-melt results in a deeper junction and a higher boron clustering concentration. Additionally, the over-melt improves the crystallinity of the junction by consuming the end-of-range damage, thus reducing the defect population. Consequently, at high doses of co-implanted indium the resulting junction has a higher sheet number and higher mobility, which correspond to a lower electrical sheet resistance.

To diminish the contribution of over-melt on the junction electrical properties over the entire dose range, the laser energy densities are adjusted to compensate for the indium dose effect on the process window. The laser energy required to approximately achieve the process for indium doses of 0.0x10^0, 1.0x10^{14}, 5.0x10^{14}, 1.5x10^{15} and 3.0x10^{15} /cm^2 are 0.74, 0.74, 0.74, 0.70 and 0.66 J/cm^2, respectively (Table 3-2). Figure 3-56 is a plot of the sheet resistance values measured by Four-Point Probe as function of annealing time at 900 ^{o}C in an ambient of nitrogen. The junctions are implanted with 15 keV silicon 1.0x10^{15} /cm^2, 1 keV boron 3.0x10^{15} /cm^2 and 5 keV indium at doses of 0.0x10^0, 1.0x10^{14}, 5.0x10^{14}, 1.5x10^{15} and 3.0x10^{15} /cm^2. In general, increasing the indium dose still results in a lower sheet resistance; being most distinguishable at an annealing time of 60s. However, at annealing times longer than 60 s, the sheet resistance begins to decrease instead of continuing to increase as previously observed (Figure 3-38).

Change in the sheet resistance response with post-LTP annealing time is not due to the adjustment of the laser energy density to achieve the process window. The control and two low doses of indium (0.0x10^0, 1.0x10^{14} and 5.0x10^{14} /cm^2) receive the same laser

energy densities as those previously reported in Figure 3-38. The primary difference between the current and previous sheet resistance values for the control and two low indium doses is the date that the post-LTP anneal is performed. Sheet resistance values reported in Figure 3-38 were measured from samples that received the post-LTP anneal in March of 2002, in contrast, valves reported in Figure 3-56 were annealed in May of 2003, approximately one year apart. Figure 3-57 plots the sheet resistance measured by Four-Point Probe as function of post-LTP annealing time for junctions annealed approximately one year apart. Based on the date the post-LTP anneal is performed, there exists a disparity in the sheet resistance values measured by Four-Point Probe.

The differences in the sheet resistance values are due to differences in junction depths associated with the duration between LTP and the post-LTP anneal. Figure 3-58 is a plot of the boron depth profiles as a function of the post-LTP[15] annealing date. For all samples the date of laser thermal processing is the same, occurring in February of 2002. SIMS depth profiles performed after LTP but before annealing are identical despite being performed one year apart. Additionally, the depth profile for the sample annealed in 2002 does not changed when depth profiled again in 2003. The lack of disparity between depth profiles of samples that are processed on the same date, but analyzed on a later date confirms that a SIMS artifact is not responsible for the difference in depth profiles. In contrast, depth profiles of samples that are annealed on different dates have distinctly different profiles. Delaying the post-LTP anneal by a year results in a diffused junction depth[16] that is approximately 75 Å deeper than the depth produced by

[15] In the legend of the figure, the acronym RTA, which stands for rapid thermal anneal is used instead of post-LTP anneal. The anneal is still 900 ^{o}C for 600 s in an ambient of nitrogen.

[16] Junction depth is defined at a concentration of $1.0x10^{18}$ /cm^{3}.

the identical anneal at an earlier date. Based on the SIMS data, the source of the phenomena is related to the date upon which the post-LTP anneal is performed.

Differences in junction depths with respect to duration between activation and the post anneal are also observed for non-LTP samples. Figure 3-59 is a plot of the SIMS depth profiles for samples implanted with 0.5 keV boron to a dose of $1.0x10^{15}$ /cm^2. The two shallow profiles are for the as implanted boron measured by SIMS one year apart. There is no motion in the as implanted profile over the one year duration between SIMS analysis dates. The two deeper profiles are for boron after a 1050 ^{o}C for 10 s rapid thermal anneal (RTA), differing only in the date upon which the anneal is performed. In agreement with trends first observed for the LTP samples, the sample annealed a year later exhibits a deeper junction than the sample receiving the same anneal and analysis a year prior. Figure 3-60 is a plot of the SIMS depth profiles for a sample with a doped amorphous layer that is re-crystallized by solid phase epitaxial regrowth (SPER). The surface of the sample is amorphized by a 12 keV germanium implant with a $1.0x10^{15}$ /cm^2 dose. The amorphous layer is implanted with boron at 0.5 keV with a dose of $1.0x10^{15}$ /cm^2. Solid phase epitaxial regrowth of the amorphous layer is achieved by annealing at 750 ^{o}C for 5 min. The shallowest boron depth profile is measured after SPER. The two intermediate depth profiles receive an RTA consisting of a 950 ^{o}C spike at the same time, but are analyzed by SIMS at different dates. With the exception of minor variations, the two intermediate boron depth profiles are identical; demonstrating again that the date upon which SIMS analysis is performed is not the source of the disparity in junction depth with age of the sample. The deepest SIMS depth profile is for a sample that receives the same RTA approximately a year later than the two previous

samples. Delaying the date that the RTA is performed results in an increase in the junction depth. Hence, as observed for several different processing conditions, allowing samples to age between implantation/activation and subsequent thermal processing results in a diffusion enhancement that increase in the final depth of the junction.

Adjusting the laser energy density to mitigate the effect of over-melt does not provide an unambiguous extension of the relationship between strain compensation and the full range of indium co-implant doses. Samples that receive the post-LTP anneal at a later data, such as those used to mitigate the effect of indium dose on over-melt by adjusting the laser energy density, experience enhanced diffusion. The enhanced diffusion occurring during the post-LTP anneal increases the junction depth such that the effect of the indium co-implant dose is not observed on the sheet resistance measured at the final annealing time of 600 s. All values as a function of dose are approximately equal at the final annealing time (Figure 3-56). Hence, due to enhanced diffusion resulting from an ageing phenomenon, adjusting the laser energy density to meet the process window did not extend the relationship between strain compensation and indium co-implantation to the higher indium doses. Additionally, due to the ageing phenomena further study of strain compensation at additional temperatures is not feasible.

Table 3-1 Maximum solid-solubility of alternate dopant species and the active carrier concentrations for LTP junctions.

Dopant Species	**Max. Solid-Solubility[17] (atoms/cm^3)**	**Xj (Å)**	**Active Carrier Conc.[18] (atoms/cm^3)**	**R_S (ohms/cm^2)**
Aluminum (Al)	$2.1x10^{19}$	~350	$3.8x10^{19}$	3795
Gallium (Ga)	$4.0x10^{19}$	~350	$1.8x10^{20}$	1009
Indium (In)	$8.0x10^{17}$	~350	$1.0x10^{19}$	5541
Nitrogen (N)	$4.5x10^{15}$	~350	NA	NA
Antimony (Sb)	$6.4x10^{19}$	~350	$3.1x10^{20}$	171

[17] Maximum solid-solubility is reported as the highest value independent of temperature [41].

[18] Active carrier concentration is calculated as the product of the sheet number measured by Hall Effect and a junction depth of approximately 350 Å.

Table 3-2 Process window for co-implant samples as a function of indium dose.

LED (J/cm^3) / **Implant Conditions**	**0.74**	**0.70**	**0.66**
15 keV $^{14}Si^+$ 1.0x10^{15} /cm^2 1 keV 5B$^+$ 3.0x10^{15} /cm^2 *No Indium*	defected crystalline	NA NA	NA NA
15 keV $^{14}Si^+$ 1.0x10^{15} /cm^2 1 keV 5B$^+$ 3.0x10^{15} /cm^2 *5 keV $^{49}In^+$ 1.0x10^{14} /cm^2*	defected crystalline	defected poly	defected poly
15 keV $^{14}Si^+$ 1.0x10^{15} /cm^2 1 keV 5B$^+$ 3.0x10^{15} /cm^2 *5 keV $^{49}In^+$ 5.0x10^{14} /cm^2*	defected crystalline	defected poly	defected poly
15 keV $^{14}Si^+$ 1.0x10^{15} /cm^2 1 keV 5B$^+$ 3.0x10^{15} /cm^2 5 keV $^{49}In^+$ 1.5x10^{15} /cm^2	few defects crystalline	defected crystalline	defected poly
15 keV $^{14}Si^+$ 1.0x10^{15} /cm^2 1 keV 5B$^+$ 3.0x10^{15} /cm^2 *5 keV $^{49}In^+$ 3.0x10^{15} /cm^2*	clean crystalline	nearly clean crystalline	few defects crystalline

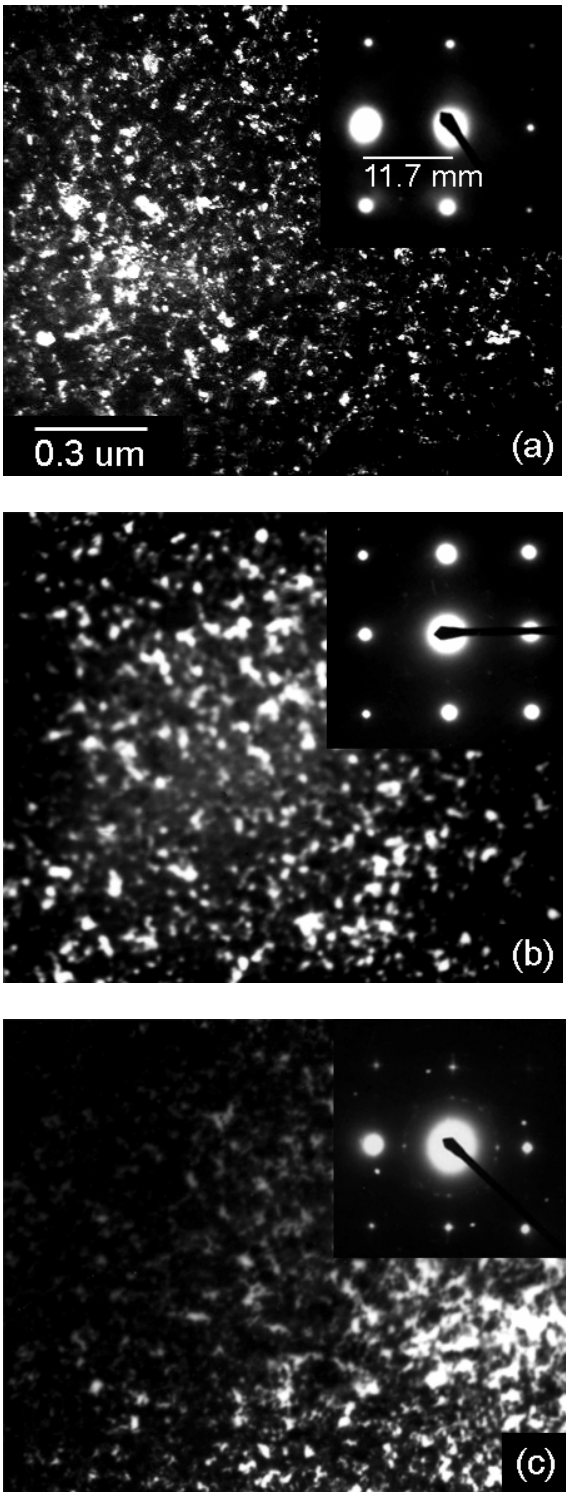

Figure 3-1 PTEM diffraction and defect micrographs of wafers preamorphized with silicon and implanted with 5 keV indium implants at doses of: (a) $1.5x10^{15}$, (b) $5.0x10^{14}$ and (c) $1.0x10^{14}$ /cm^2, after laser thermal processing with an energy density of 0.68 J/cm^2.

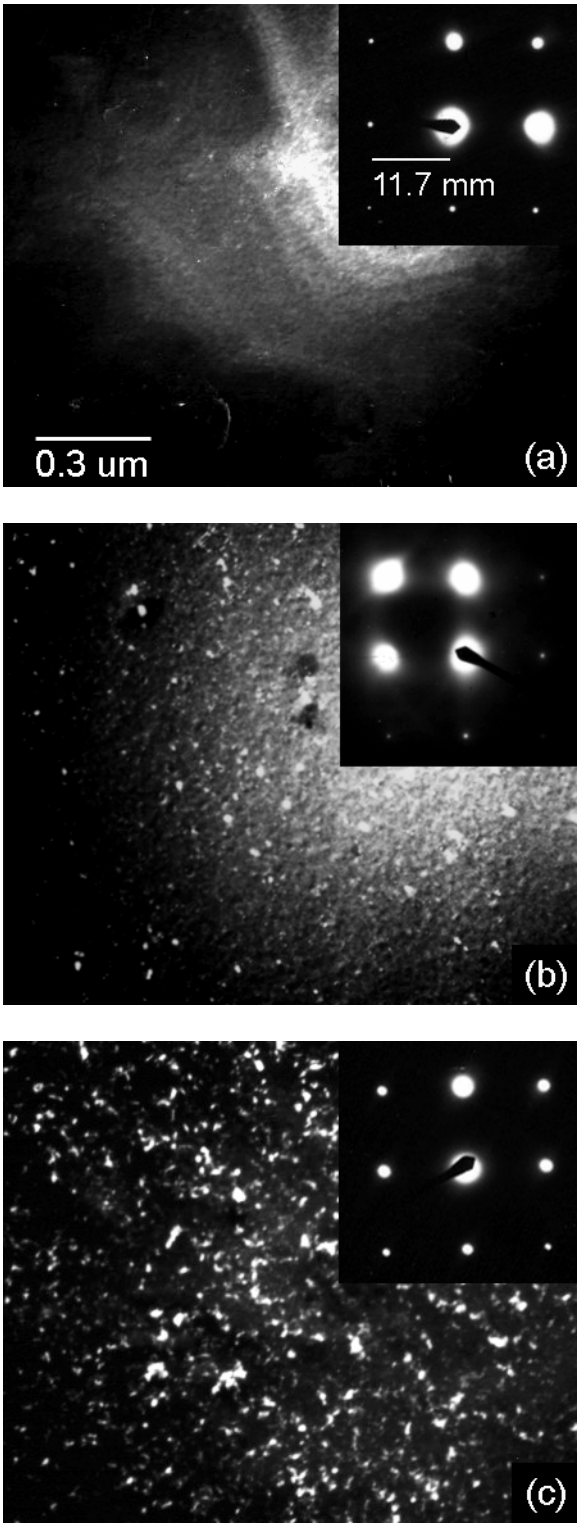

Figure 3-2 PTEM diffraction and defect micrographs of wafers preamorphized with silicon and implanted with 5 keV indium implants at doses of: (a) $1.5x10^{15}$, (b) $5.0x10^{14}$ and (c) $1.0x10^{14}$ /cm^2, after laser thermal processing with an energy density of 0.76 J/cm^2.

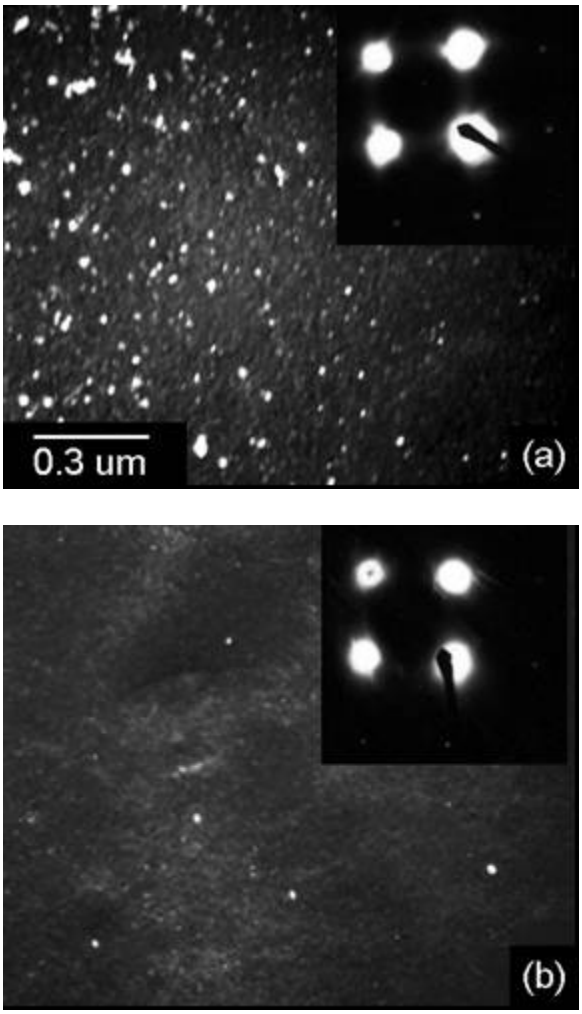

Figure 3-3 PTEM diffraction and defect micrographs of wafers preamorphized with silicon and implanted with 1 keV boron implants at doses of: (a) $1.0x10^{14}$, (b) $1.5x10^{15}$ /cm^2, after laser thermal processing with an energy density of 0.76 J/cm^2.

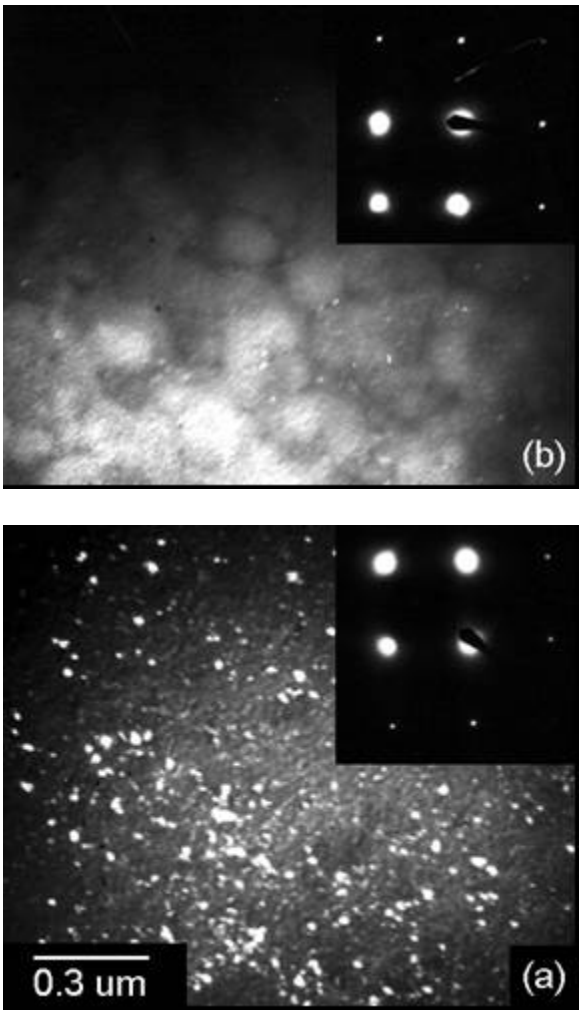

Figure 3-4 PTEM diffraction and defect micrographs of wafers preamorphized with silicon and implanted with 5 keV aluminum implants at doses of: (a) $1.0x10^{14}$, (b) $1.5x10^{15}$ /cm^2, after laser thermal processing with an energy density of 0.76 J/cm^2.

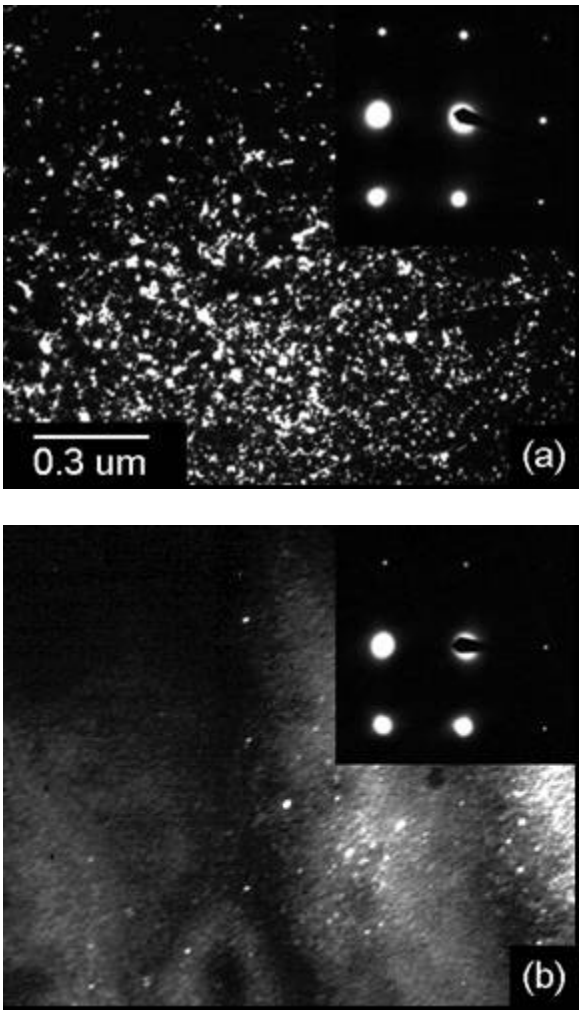

Figure 3-5 PTEM diffraction and defect micrographs of wafers preamorphized with silicon and implanted with 5 keV gallium implants at doses of: (a) $1.0x10^{14}$, (b) $1.5x10^{15}$ /cm^2, after laser thermal processing with an energy density of 0.76 J/cm^2.

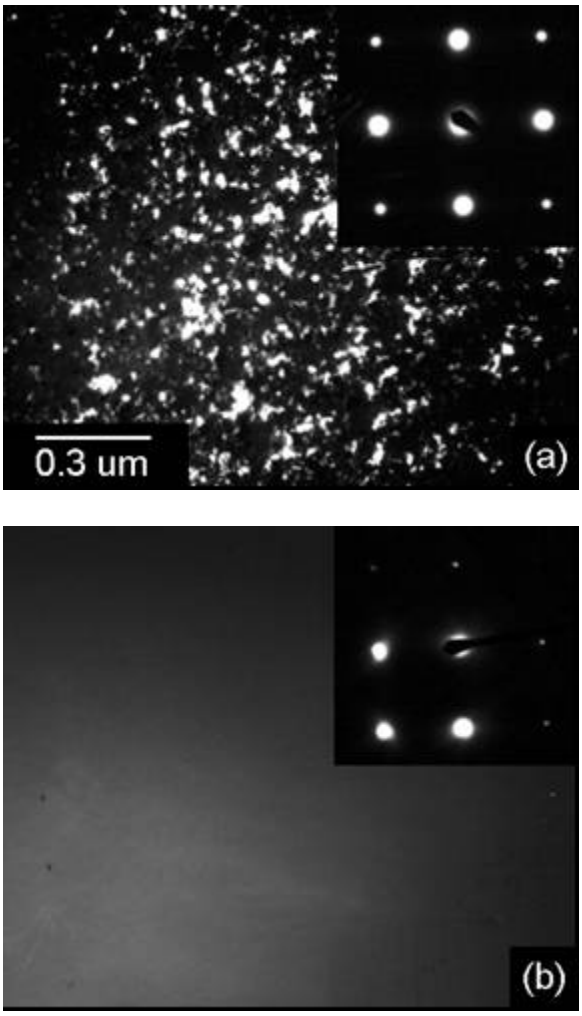

Figure 3-6 PTEM diffraction and defect micrographs of wafers preamorphized with silicon and implanted with 5 keV nitrogen implants at doses of: (a) $1.0x10^{14}$, (b) $1.5x10^{15}/cm^2$, after laser thermal processing with an energy density of 0.76 J/cm^2.

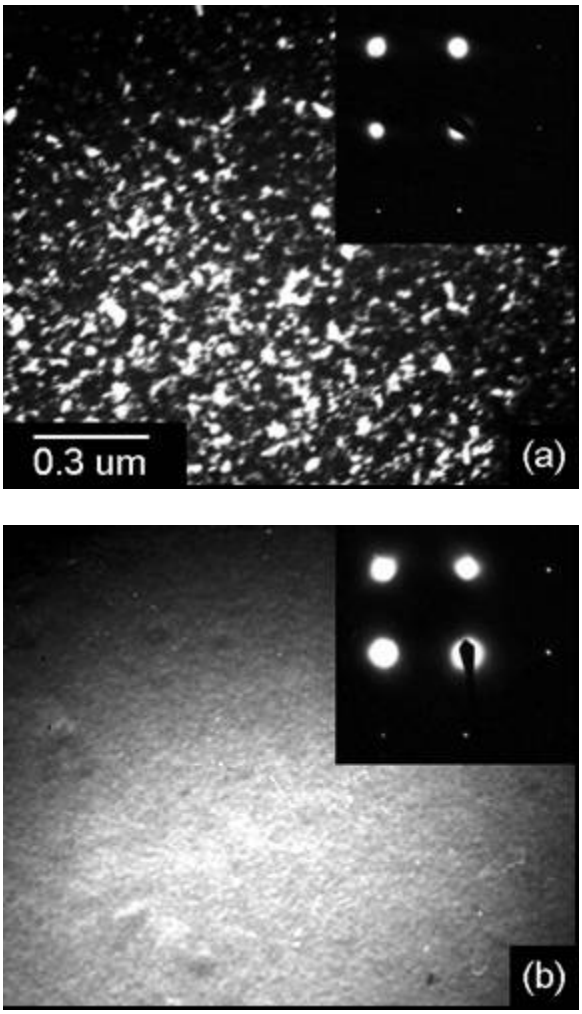

Figure 3-7 PTEM diffraction and defect micrographs of wafers preamorphized with silicon and implanted with 5 keV arsenic implants at doses of: (a) $1.0x10^{14}$, (b) $1.5x10^{15}$ /cm^2, after laser thermal processing with an energy density of 0.76 J/cm^2.

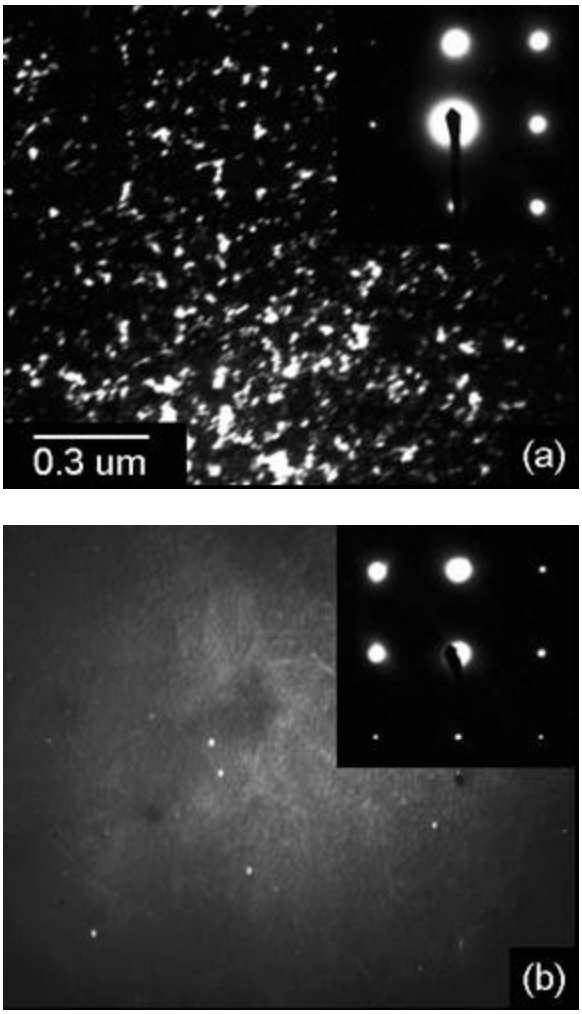

Figure 3-8 PTEM diffraction and defect micrographs of wafers preamorphized with silicon and implanted with 5 keV antimony implants at doses of: (a) $1.0x10^{14}$, (b) $1.5x10^{15}$ /cm^2, after laser thermal processing with an energy density of 0.76 J/cm^2.

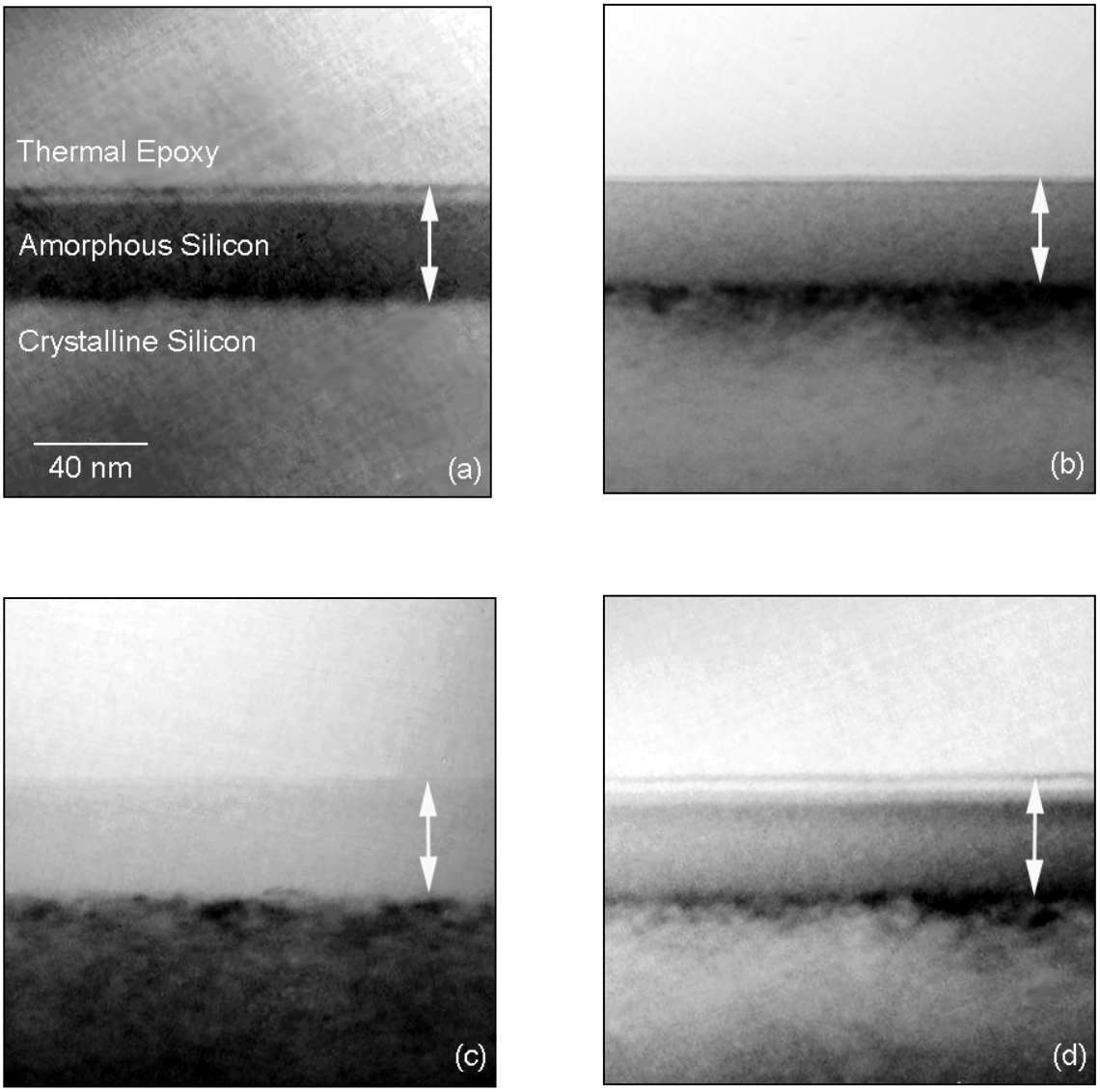

Figure 3-9 Amorphous depth imaged by XTEM at a magnification of 150,000X, after implants of 15 keV silicon $1.0x10^{15}/cm^2$ and 5 keV indium for doses of: a) $0.0x10^{00}$, b) $1.0x10^{14}$, c) and $5.0x10^{14}$ and d) $1.5x10^{15}/cm^2$.

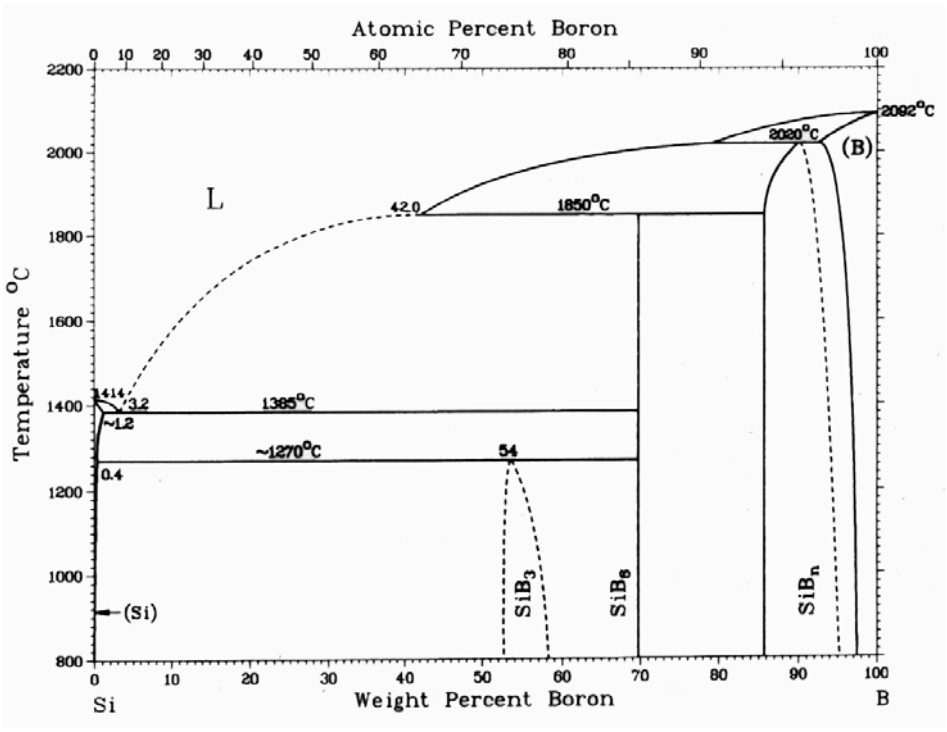

Figure 3-10 Equilibrium phase diagram for boron-silicon system [74].

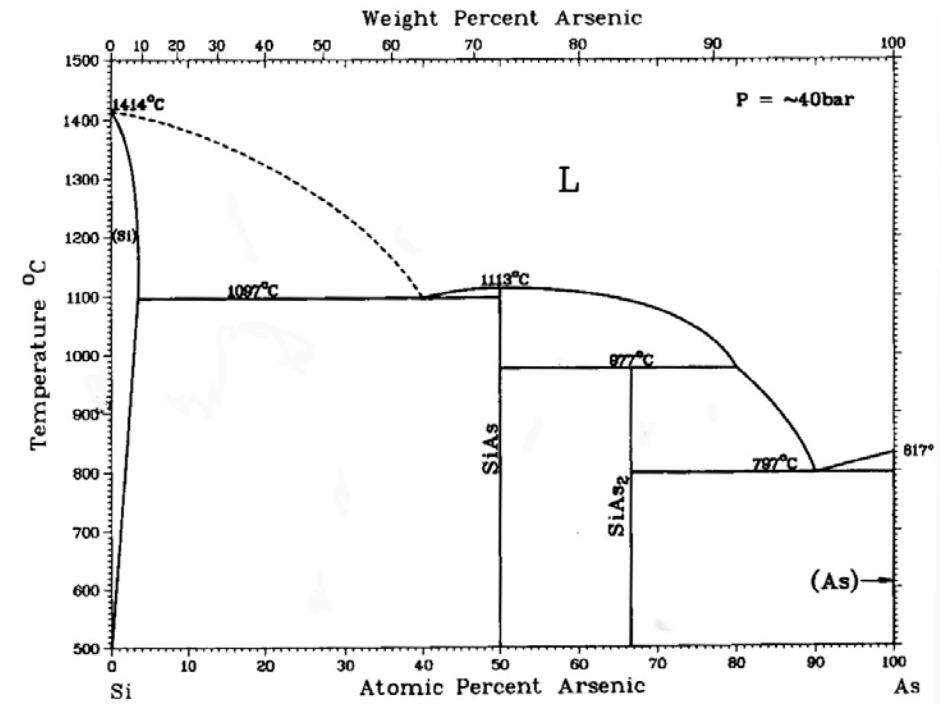

Figure 3-11 Equilibrium phase diagram for arsenic-silicon system [74].

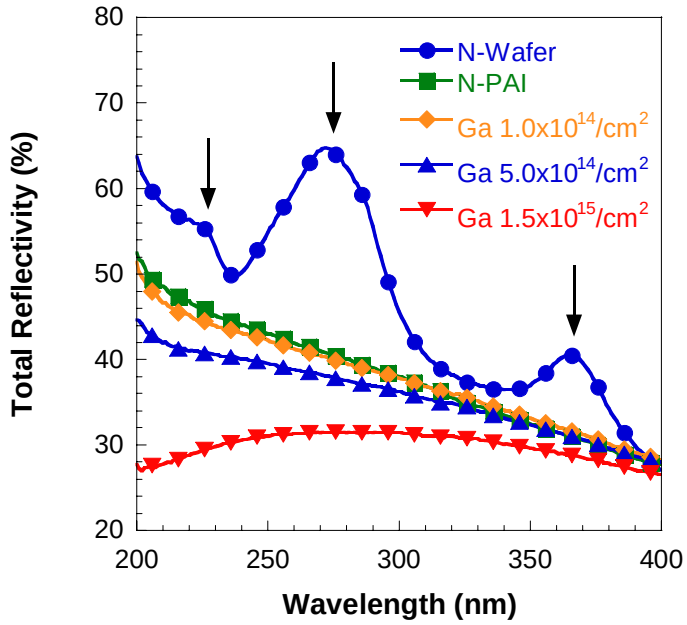

Figure 3-12 Total reflectivity as a function of wavelength measured by UV-Vis. system as a function of implant conditions prior to LTP.

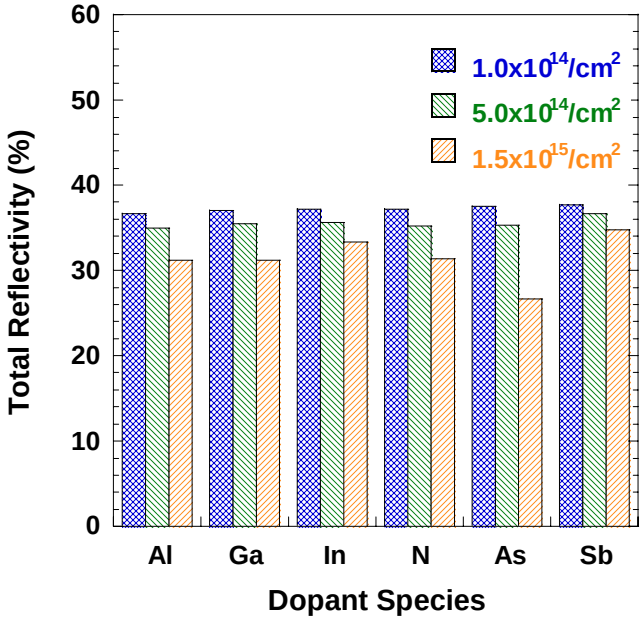

Figure 3-13 Total reflectivity as a function of dopant dose measured at a wavelength of 308 nm, prior to LTP. All samples are amorphized with a 15 keV silicon implant with dose of $1.0x10^{15}$ /cm^2.

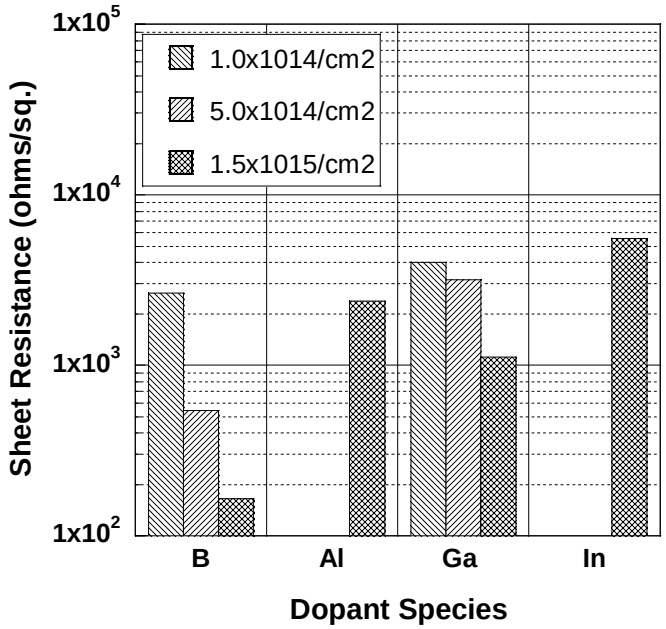

Figure 3-14 Sheet resistance measured by Hall Effect for p-type alternate dopants after LTP as a function of implant dose. Samples are preamorphized with a 15 keV silicon $1.0x10^{15}$ /cm^2 and implanted with the dopant species at doses of $1.0x10^{14}$, $5.0x10^{14}$ and $1.5x10^{15}$ /cm^2. The doped amorphous layer is activated and recrystallized by LTP.

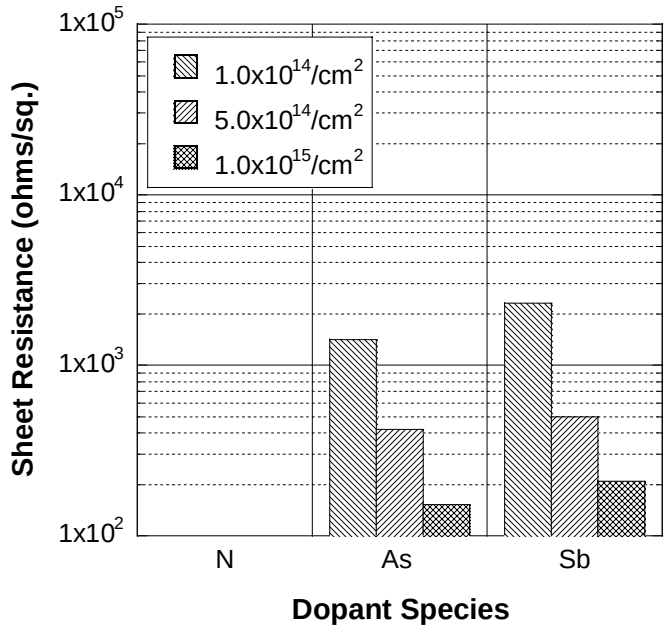

Figure 3-15 Sheet resistance measured by Hall Effect for n-type alternate dopants after LTP as a function of implant dose. Samples are preamorphized with a 15 keV silicon $1.0x10^{15}$ /cm^2 and implanted with the dopant species at doses of $1.0x10^{14}$, $5.0x10^{14}$ and $1.5x10^{15}$ /cm^2. The doped amorphous layer is activated and recrystallized by LTP.

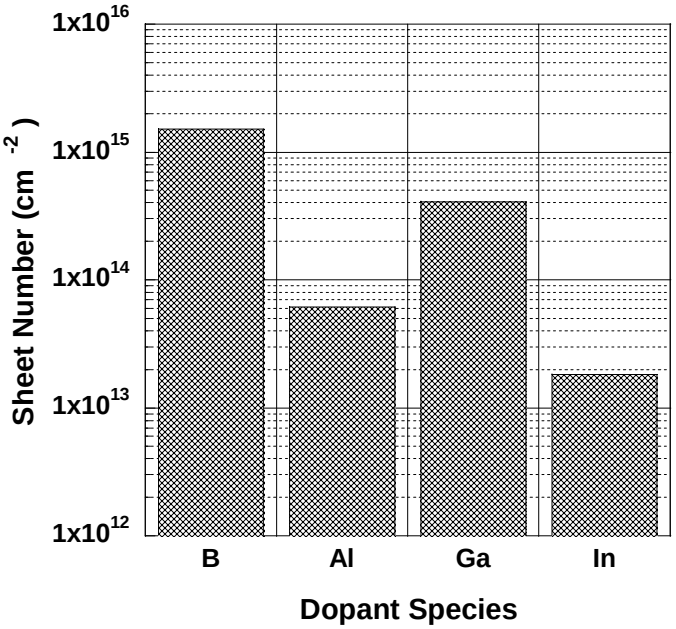

Figure 3-16 Sheet number measured by Hall Effect for p-type alternate dopants after LTP for an implant dose of $1.5x10^{15}$ /cm^2. Samples are preamorphized with a 15 keV silicon $1.0x10^{15}$ /cm^2 and implanted with the dopant species at dose of $1.5x10^{15}$ /cm^2. The doped amorphous layer is activated and recrystallized by a laser energy density of 0.68 J/cm^2.

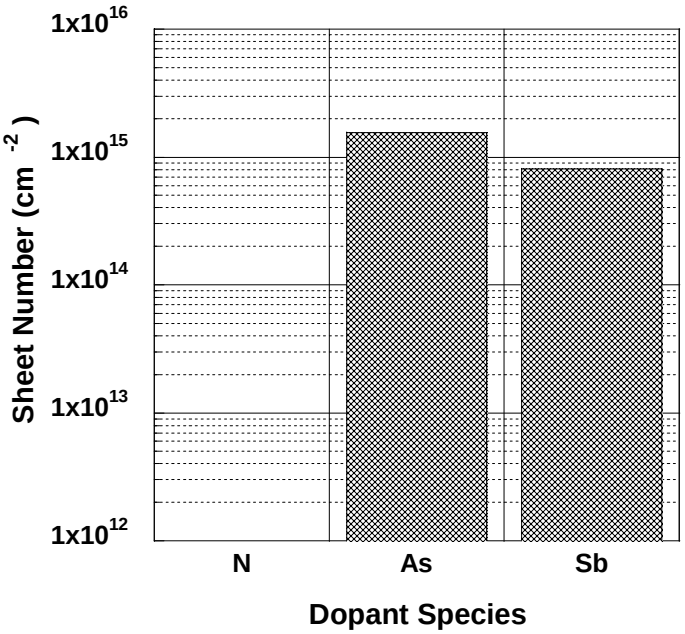

Figure 3-17 Sheet number measured by Hall Effect for n-type alternate dopants after LTP for an implant dose of $1.5x10^{15}$ /cm^2. Samples are preamorphized with a 15 keV silicon $1.0x10^{15}$ /cm^2 and implanted with the dopant species at dose of $1.5x10^{15}$ /cm^2. The doped amorphous layer is activated and recrystallized by a laser energy density of 0.68 J/cm^2.

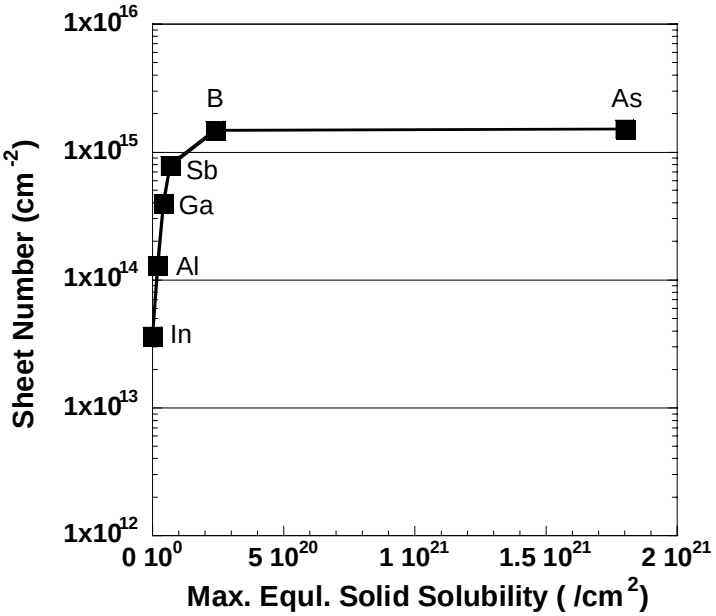

Figure 3-18 Sheet number for an implant dose of $1.5x10^{15}$ /cm^2 after LTP as a function of alternate dopant species maximum equilibrium solubility. Samples are preamorphized with a 15 keV silicon $1.0x10^{15}$ /cm^2 and implanted with the dopant species at dose of $1.5x10^{15}$ /cm^2. The doped amorphous layer is activated and recrystallized by a laser energy density of 0.68 J/cm^2.

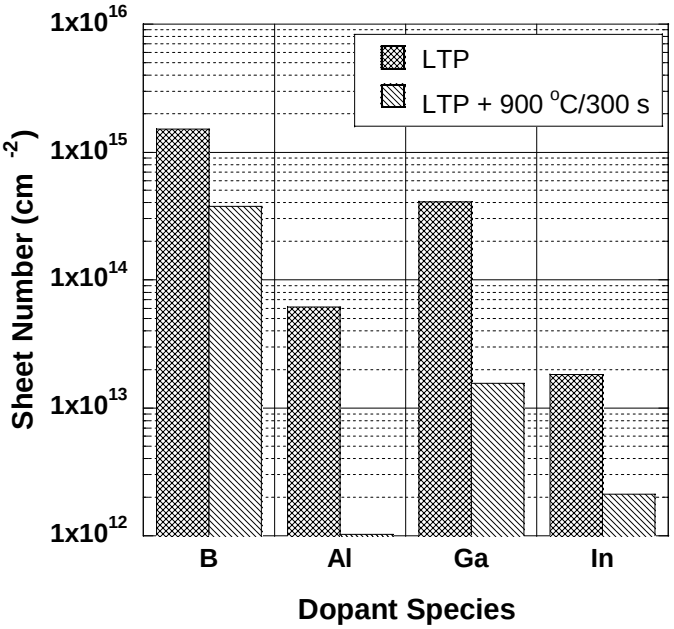

Figure 3-19 Sheet number measured by Hall Effect for p-type alternate dopants after LTP and again after a 900 ^{o}C/300 s anneal for samples implanted with a dopant dose of $1.5x10^{15}$ /cm^2. Samples are preamorphized with a 15 keV silicon $1.0x10^{15}$ /cm^2 and recrystallized by a laser energy density of 0.68 J/cm^2.

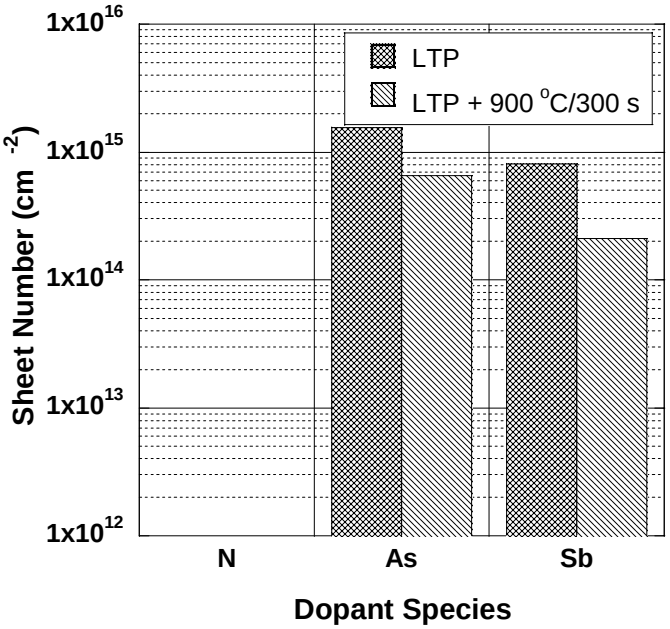

Figure 3-20 Sheet numbers measured by Hall Effect for n-type alternate dopants after LTP and again after a 900 ^{o}C/300 s anneal for samples implanted with a dopant dose of 1.5x10^{15} /cm^{2}. Samples are preamorphized with a 15 keV silicon 1.0x10^{15} /cm^{2} and recrystallized by a laser energy density of 0.68 J/cm^{2}.

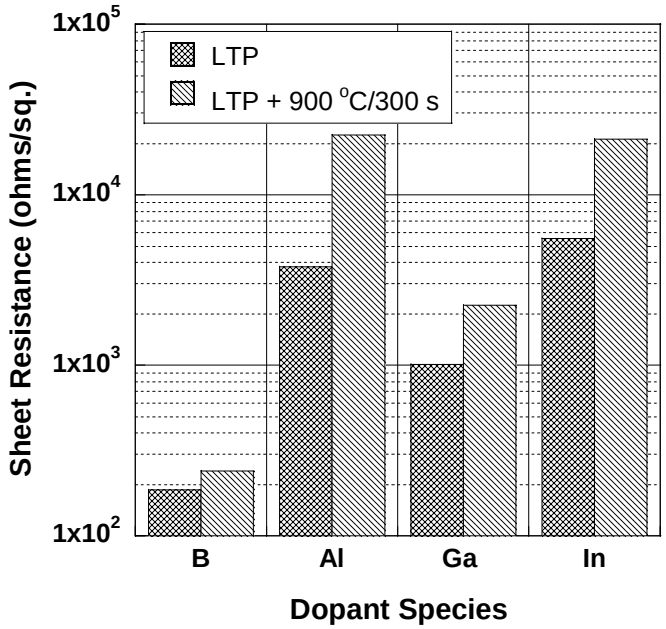

Figure 3-21 Sheet resistance measured by Hall Effect for p-type alternate dopants after LTP and again after a 900 ^{o}C/300 s anneal for samples implanted with a dopant dose of 1.5x10^{15} /cm^{2}. Samples are preamorphized with a 15 keV silicon 1.0x10^{15} /cm^{2} and recrystallized by a laser energy density of 0.68 J/cm^{2}.

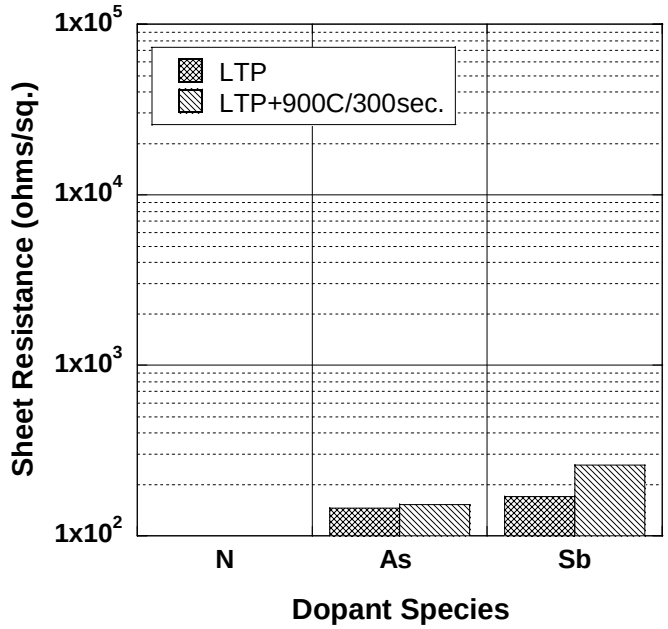

Figure 3-22 Sheet resistance measured by Hall Effect for n-type alternate dopants after LTP and again after a 900 ^{o}C/300 s anneal for samples implanted with a dopant dose of $1.5x10^{15}$ /cm^2. Samples are preamorphized with a 15 keV silicon $1.0x10^{15}$ /cm^2 and recrystallized by a laser energy density of 0.68 J/cm^2.

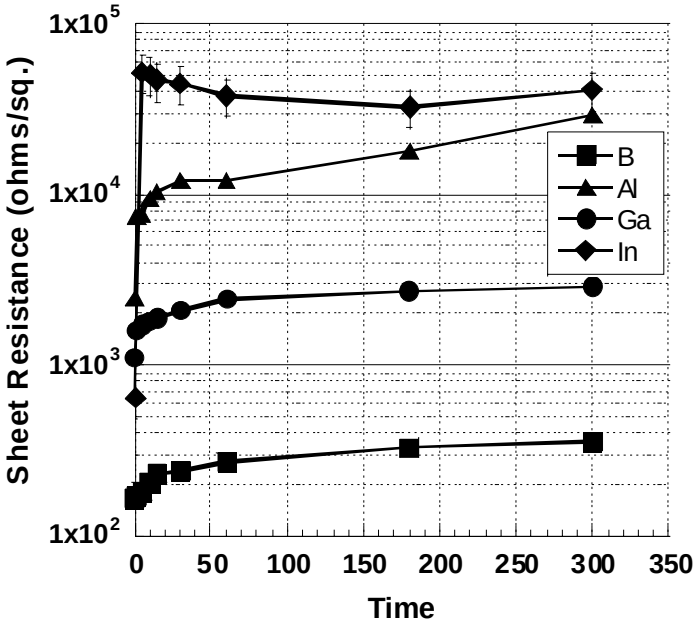

Figure 3-23 Sheet resistance measured by Four-Point Probe for p-type alternate dopants as a function of annealing time at 900 ^{o}C for dopant implant doses of $1.5x10^{15}$ /cm^2. Samples are preamorphized with a 15 keV silicon $1.0x10^{15}$ /cm^2 and recrystallized by a laser energy density of 0.68 J/cm^2.

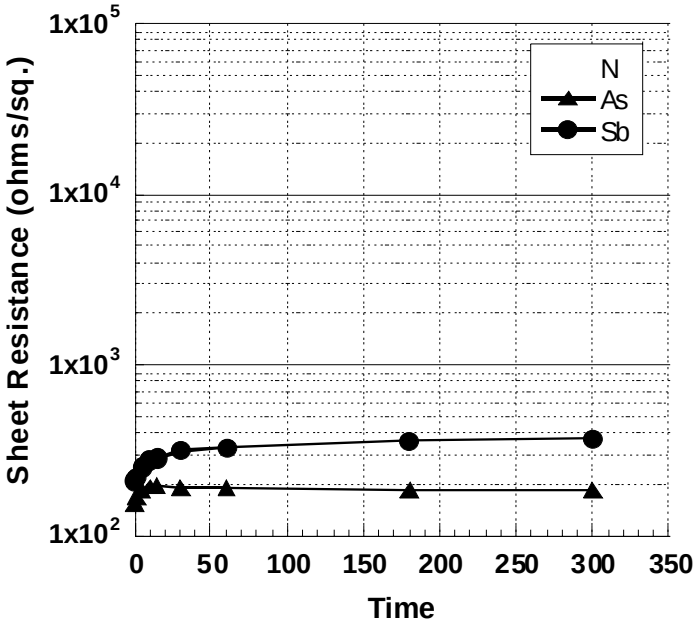

Figure 3-24 Sheet resistance measured by Four-Point Probe for n-type alternate dopants as a function of annealing time at 900 ^{o}C for dopant implant doses of $1.5x10^{15}$ /cm^2. Samples are preamorphized with a 15 keV silicon $1.0x10^{15}$ /cm^2 and recrystallized by a laser energy density of 0.68 J/cm^2.

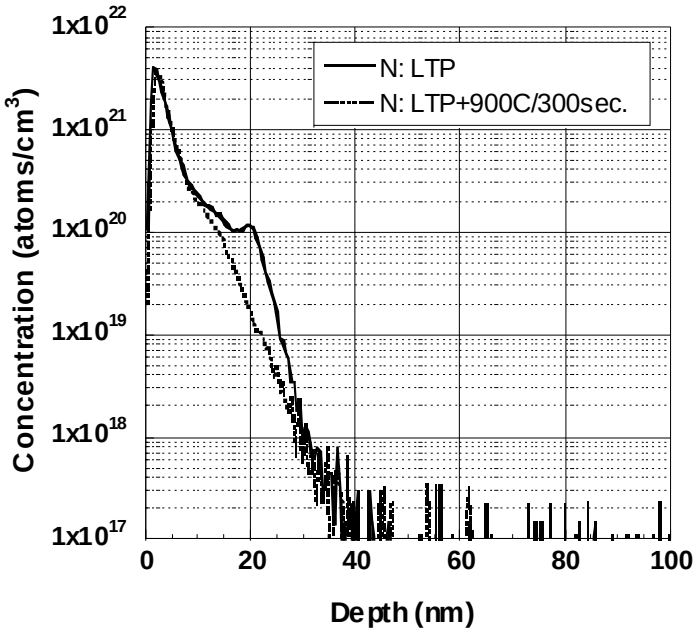

Figure 3-25 Secondary Ion Mass Spectrometry depth profile of nitrogen for an implant dose of 1.5x1015 /cm2, after LTP and the post-LTP anneal. The sample is preamorphized with a 15 keV silicon $1.0x10^{15}$ /cm^2 and recrystallized by a laser energy density of 0.68 J/cm^2.

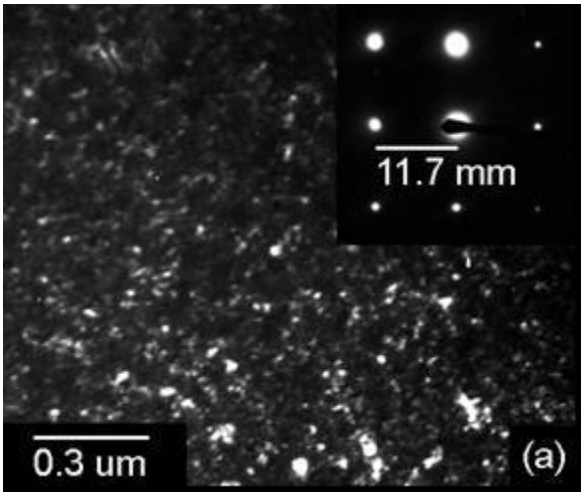

Figure 3-26 Diffraction and defect micrographs for a sample preamorphized with a 15 keV silicon implant of $1.0x10^{15}$ /cm^2 dose. The amorphous layer is implanted with 1 keV boron at a dose of $3.0x10^{15}$ /cm^2, no indium is implanted. The amorphous layer is regrown by a laser energy density of: (a) 0.74 J/cm^2.

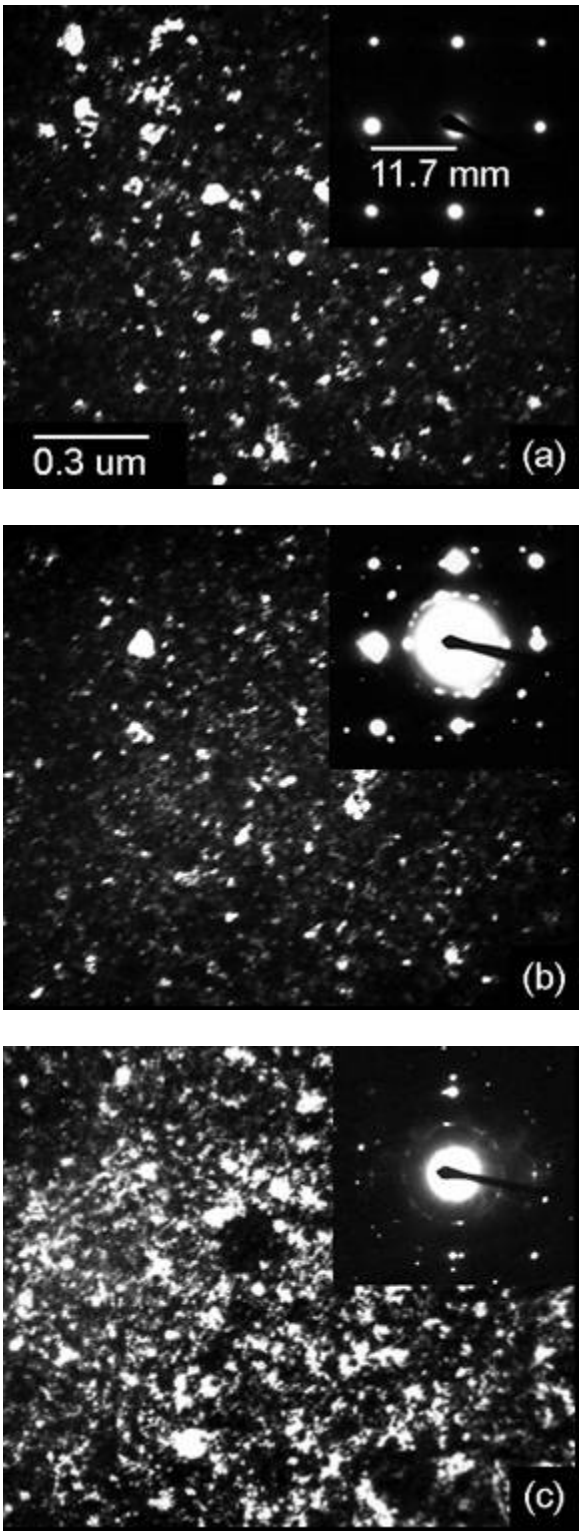

Figure 3-27 Diffraction and defect micrographs for amorphous layers, implanted with a $1.0x10^{14}$ /cm^2 dose of indium and a $3.0x10^{15}$ /cm^2 dose of boron, which are regrown by laser energy densities of: (a) 0.74, (b) 0.70 and (c) 0.66 J/cm^2.

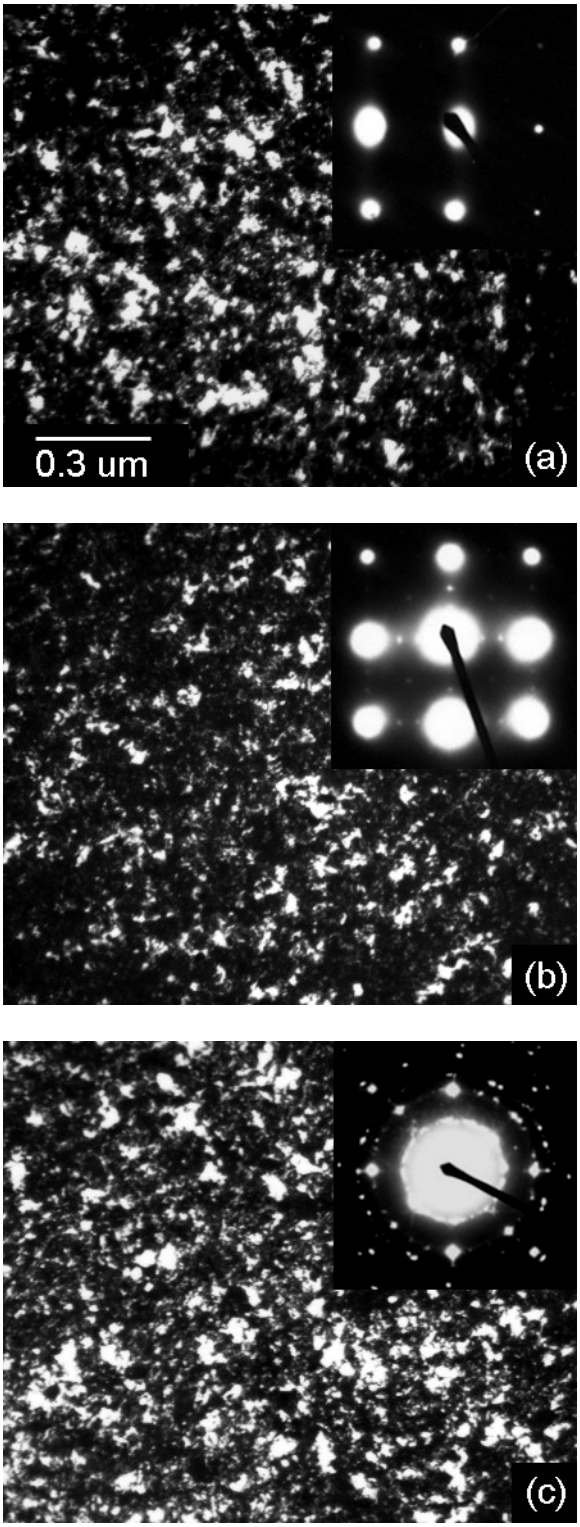

Figure 3-28 Diffraction and defect micrographs for amorphous layers, implanted with a $5.0x10^{14}$ /cm^2 dose of indium and a $3.0x10^{15}$ /cm^2 dose of boron, which are regrown by laser energy densities of: (a) 0.74, (b) 0.70 and (c) 0.66 J/cm^2.

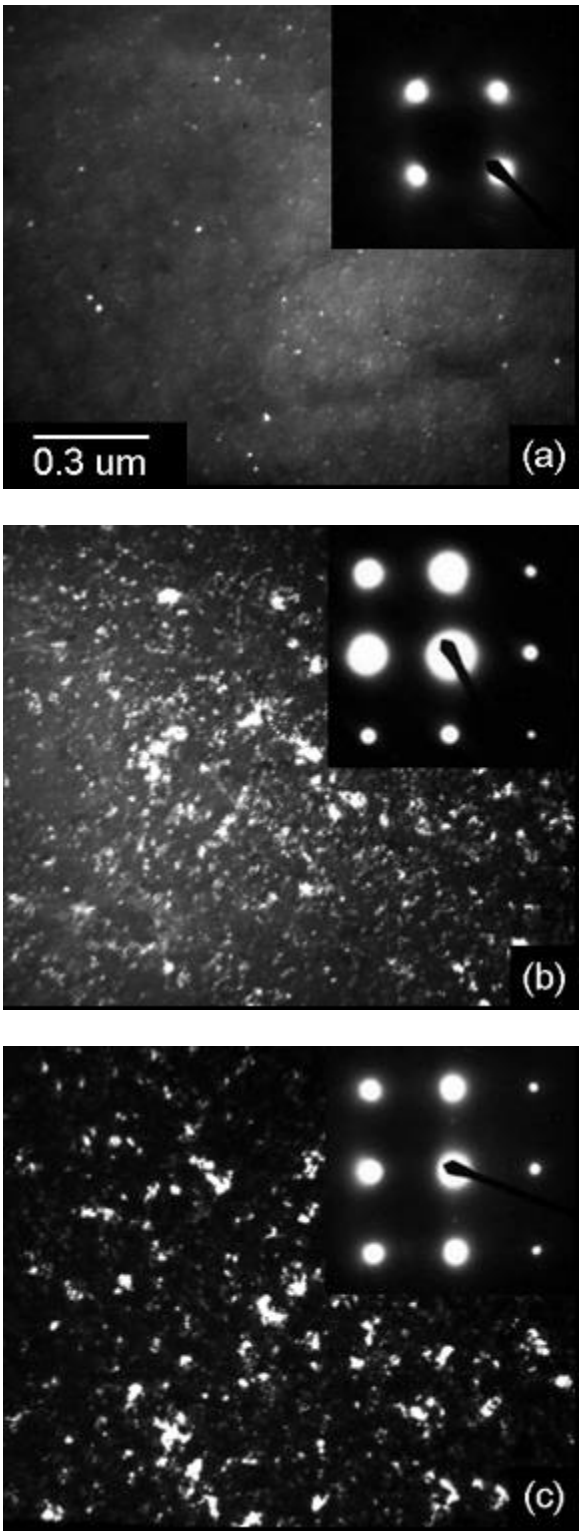

Figure 3-29 Diffraction and defect micrographs for amorphous layers, implanted with a $1.5x10^{15}$ /cm^2 dose of indium and a $3.0x10^{15}$ /cm^2 dose of boron, which are regrown by laser energy densities of: (a) 0.74, (b) 0.70 and (c) 0.66 J/cm^2.

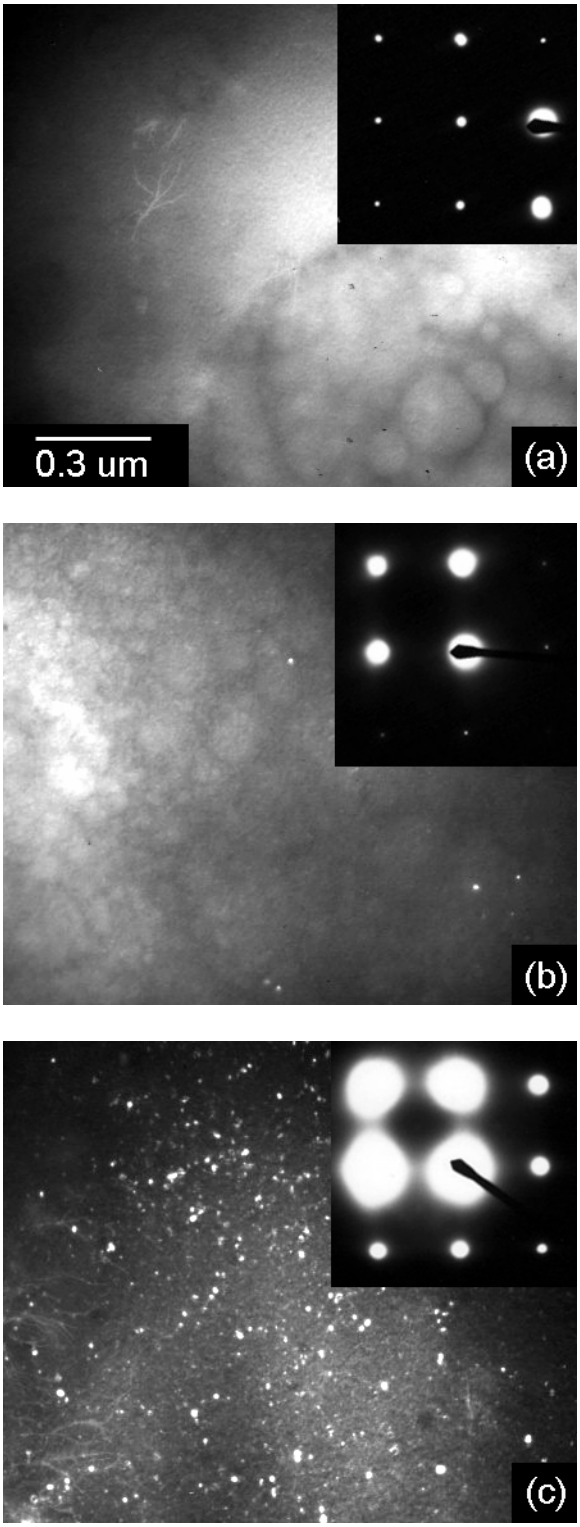

Figure 3-30 Diffraction and defect micrographs for amorphous layers, implanted with a $3.0x10^{15}$ /cm^2 dose of indium and a $3.0x10^{15}$ /cm^2 dose of boron, which are regrown by laser energy densities of: (a) 0.74, (b) 0.70 and (c) 0.66 J/cm^2.

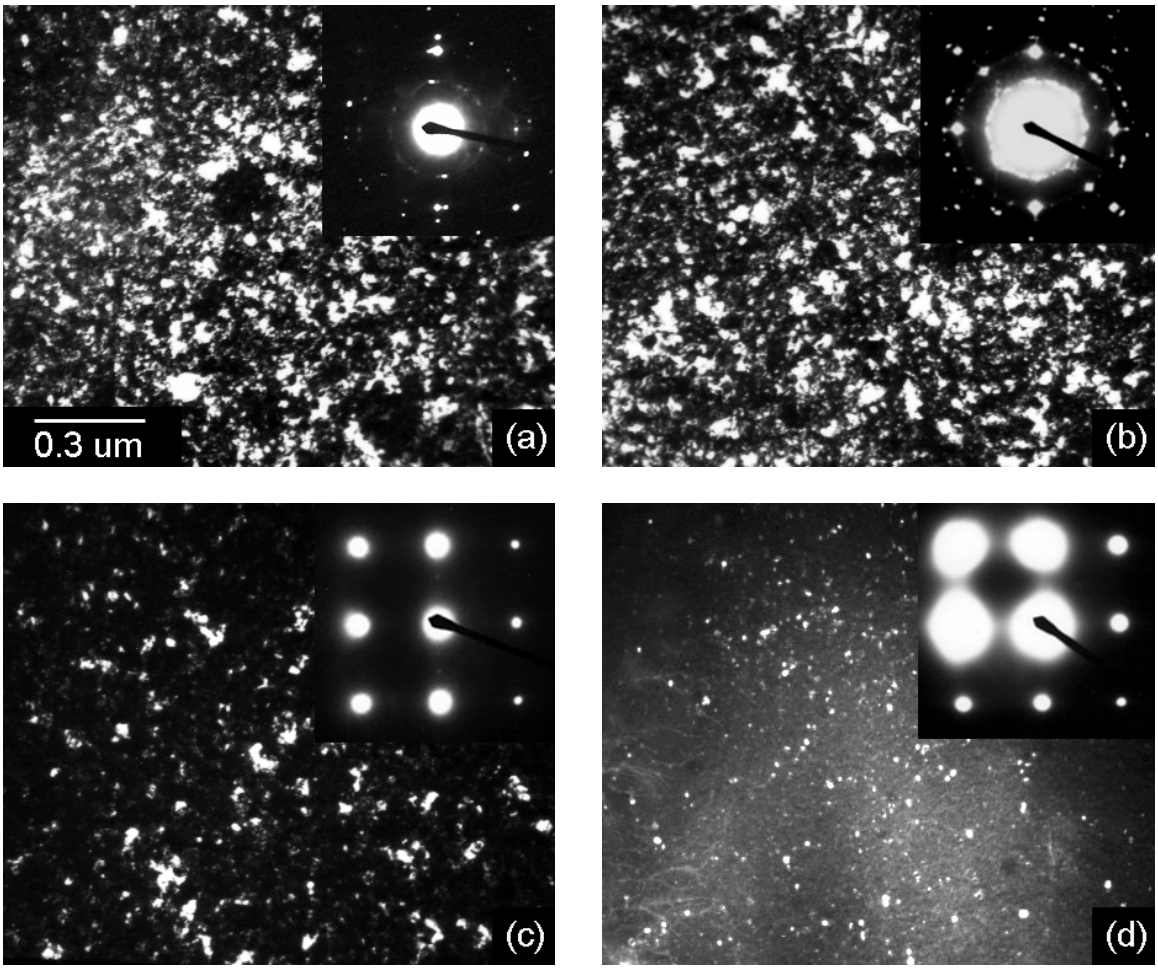

Figure 3-31 PTEM defect micrographs after laser thermal processing at an energy density of 0.66 J/cm^2, as a function of 5 keV co-implant indium dose: (a) 1.0x10^{14}, (b) 5.0x10^{14}, (c) 1.5x10^{15} and (d) 3.0x10^{15} /cm^2.

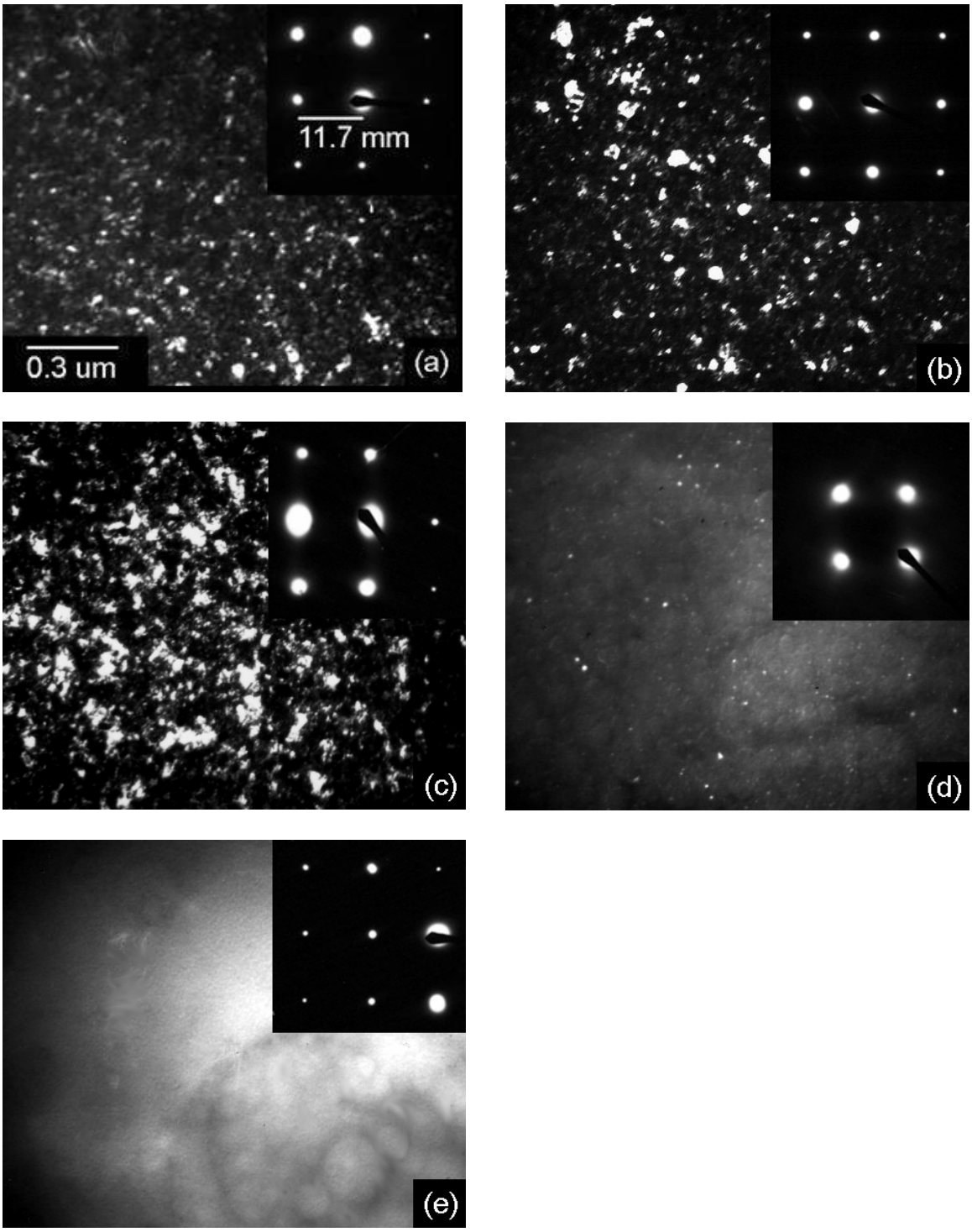

Figure 3-32 PTEM defect micrographs after laser thermal processing at an energy density of 0.74 J/cm^2, as a function of 5 keV co-implant indium dose: (a) 0.0x10^0, (b) 1.0x10^{14}, (c) 5.0x10^{14}, (d) 1.5x10^{15} and (e) 3.0x10^{15} /cm^2.

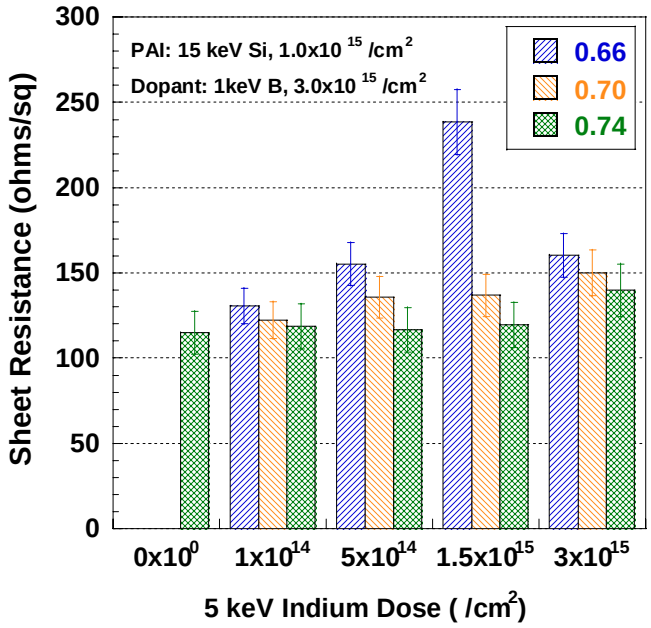

Figure 3-33 Sheet resistance measured by Hall Effect as a function of 5 keV indium dose after laser thermal processing at energy densities of 0.66, 0.70 and 0.74 J /cm^2 for common preamorphizing and boron implants. The preamorphizing implant is a 15 keV silicon implant with a 1.0x10^{15} /cm^2 dose and the boron is implanted at 1 keV with a 3.0x10^{15} /cm^2 dose.

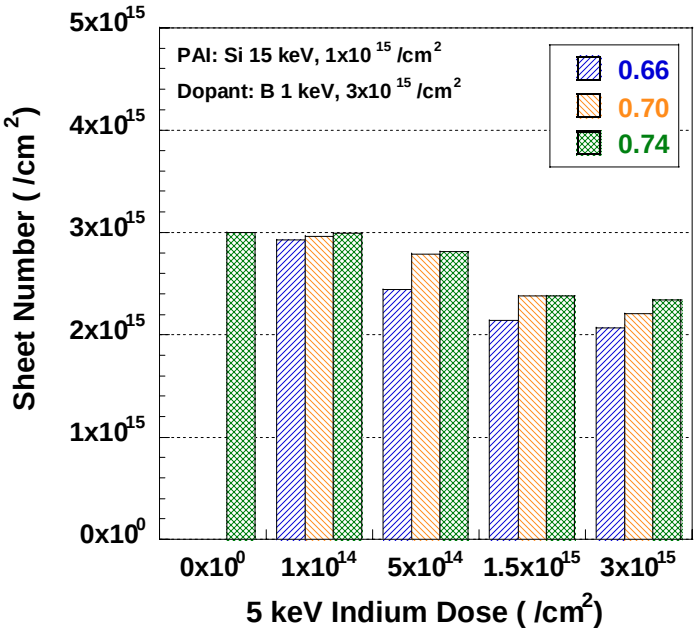

Figure 3-34 Sheet number measured by Hall Effect as a function of 5 keV indium dose after laser thermal processing at energy densities of 0.66, 0.70 and 0.74 J /cm^2 for common preamorphizing and boron implants. The preamorphizing implant is a 15 keV silicon implant with a 1.0x10^{15} /cm^2 dose and the boron is implanted at 1 keV with a 3.0x10^{15} /cm^2 dose.

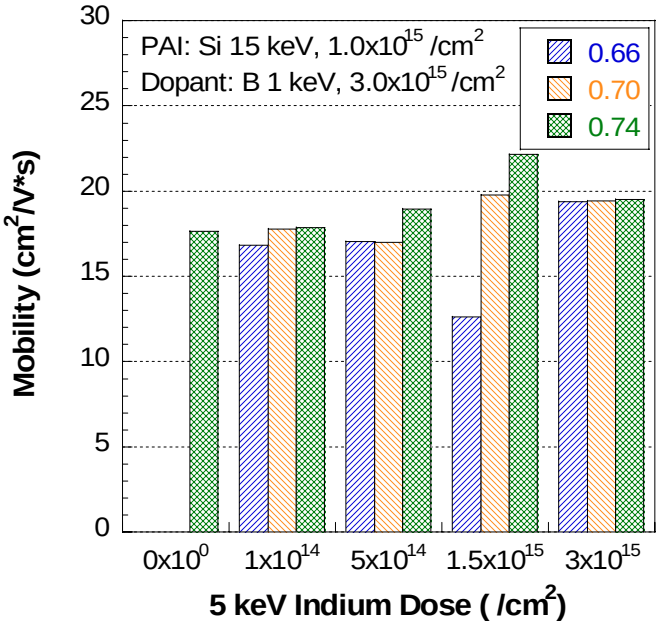

Figure 3-35 Carrier mobility measured by Hall Effect as a function of 5 keV indium dose after laser thermal processing at energy densities of 0.66, 0.70 and 0.74 J /cm^2 for common preamorphizing and boron implants. The preamorphizing implant is a 15 keV silicon implant with a 1.0x10^{15} /cm^2 dose and the boron is implanted at 1 keV with a 3.0x10^{15} /cm^2 dose.

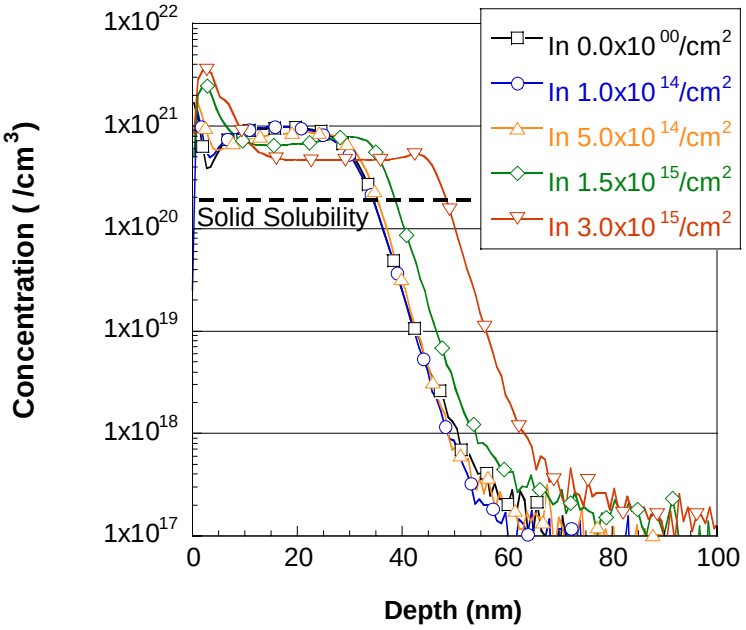

Figure 3-36 Boron depth profiles measured by SIMS after LTP at an energy density of 0.74 J/cm^2, for junctions preamorphized with a 15 keV silicon 1.0x10^{15} /cm^2, implanted with 1 keV boron 3.0x10^{15} /cm^2 and 5 keV indium at doses of 0.0x10^{00}, 1.0x10^{14}, 5.0x10^{14}, 1.5x10^{15} and 3.0x10^{15} /cm^2.

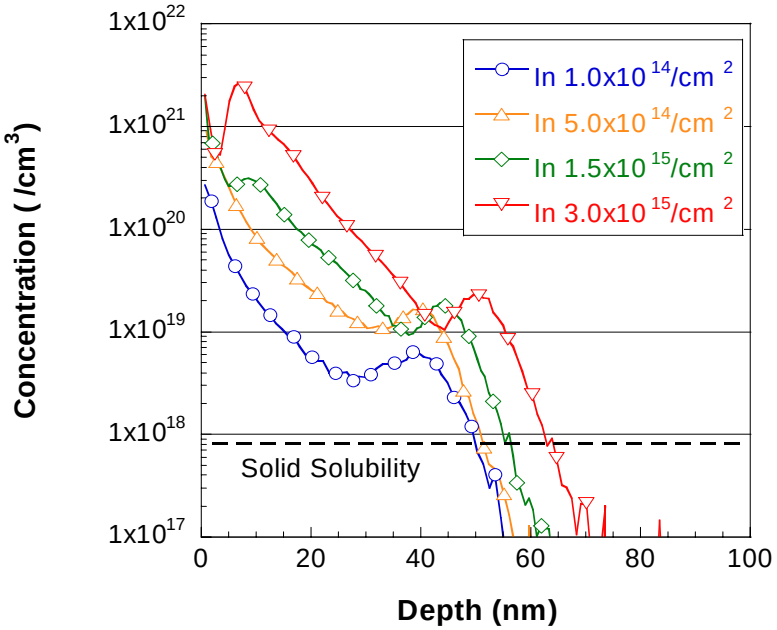

Figure 3-37 Indium depth profiles measured by SIMS after LTP at an energy density of 0.74 J/cm^2, for junctions preamorphized with a 15 keV silicon 1.0x10^{15} /cm^2, implanted with 1 keV boron 3.0x10^{15} /cm^2 and 5 keV indium at doses of 1.0x10^{14}, 5.0x10^{14}, 1.5x10^{15} and 3.0x10^{15} /cm^2.

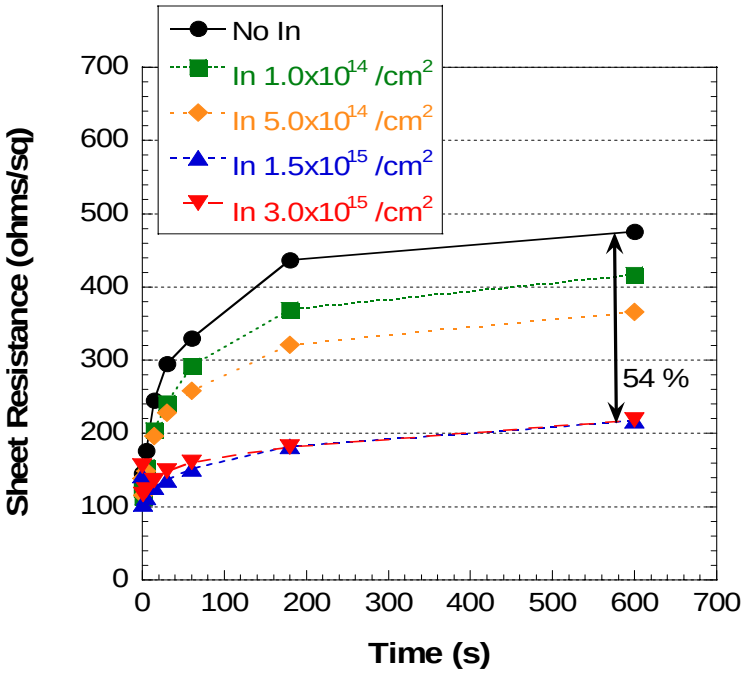

Figure 3-38 Sheet resistance measured by Four-Point Probe as function of annealing time at 900 ^{o}C for junctions preamorphized with a 15 keV silicon 1.0x10^{15} /cm^{2}, implanted with 1 keV boron 3.0x10^{15} /cm^{2} and 5 keV indium at doses of 0.0x10^{00} (control) junctions implanted with 15 keV silicon 1.0x10^{15} /cm^{2}, 1 keV boron 3.0x10^{15} /cm^{2} and 5 keV indium at doses of 0.0x10^{00}, 1.0x10^{14}, 5.0x10^{14}, 1.5x10^{15} and 3.0x10^{15} /cm^{2}, and irradiated with an energy density of 0.74 J/cm^{2}.

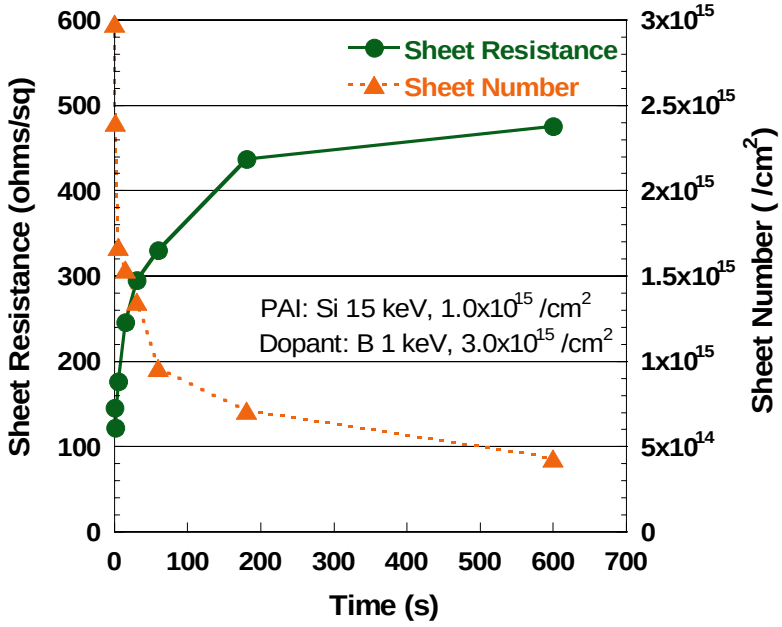

Figure 3-39 Comparison of the sheet resistance measured by Four-Point Probe and the sheet number measured by Hall Effect as function of annealing time at 900 ^{o}C for the control sample (no indium co-implant) implanted with 15 keV silicon 1.0x10^{15}/cm^{2}, 1 keV boron 3.0x10^{15}/cm^{2} and irradiated with a 0.74 J/cm^{2} energy density.

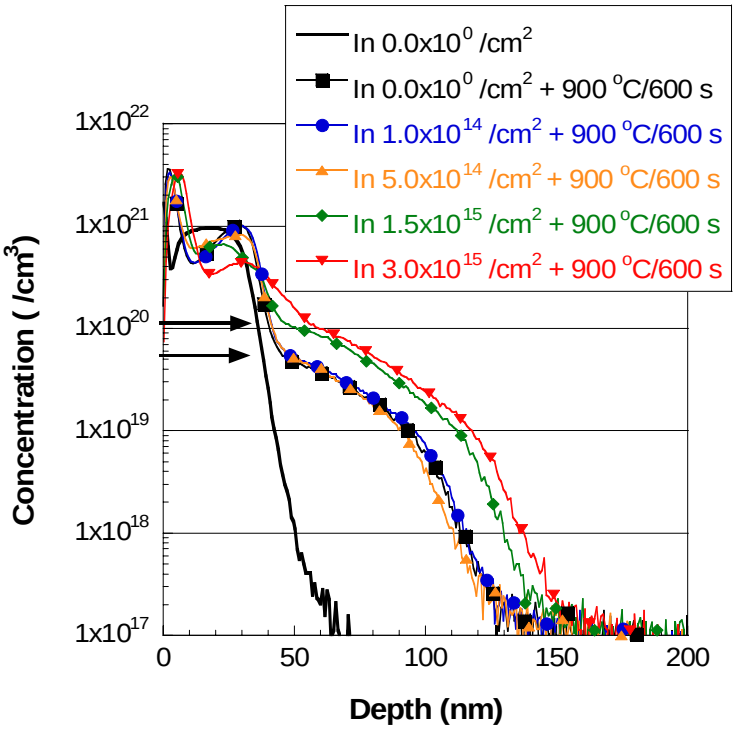

Figure 3-40 Boron depth profiles measured by SIMS after the post-LTP anneal (900 ^{o}C/600 s), for junctions preamorphized with a 15 keV silicon 1.0x10^{15} /cm^{2}, implanted with 1 keV boron 3.0x10^{15} /cm^{2} and 5 keV indium at doses of 0.0x10^{00} (control), 1.0x10^{14}, 5.0x10^{14}, 1.5x10^{15} and 3.0x10^{15} /cm^{2}. Samples were irradiated with a laser energy density of 0.74 J/cm^{2}.

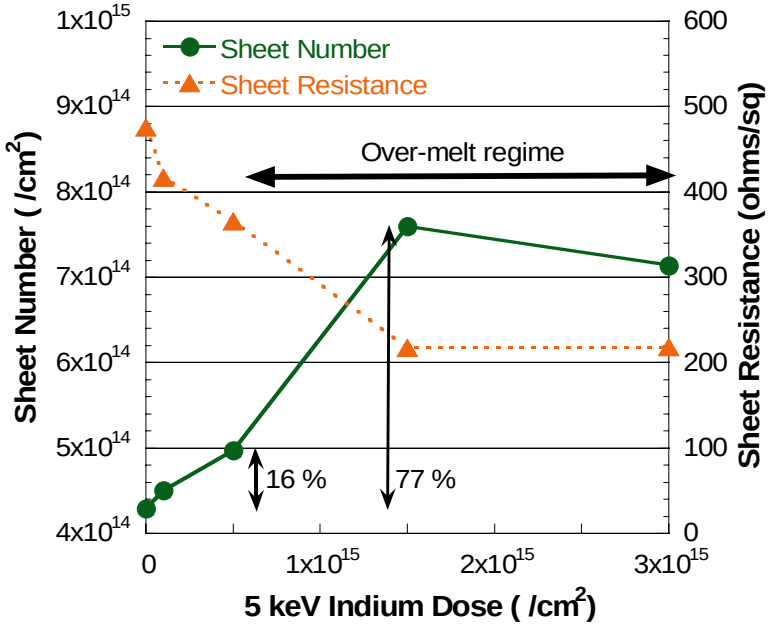

Figure 3-41 Sheet number measured by Hall Effect and sheet resistance measured by Four-Point Probe as a function of 5 keV indium co-implant dose after the post-LTP anneal at 900 ^{o}C for 600 s. Prior to the post-LTP anneal the samples are amorphized by a 1.0x10^{15} /cm^{2} dose of silicon implanted at 15 keV. Boron is implanted into the amorphous layer at 1 keV with a 3.0x10^{15} /cm^{2} dose. The layer is recrystallized by a laser energy density of 0.74 J/cm^{2}.

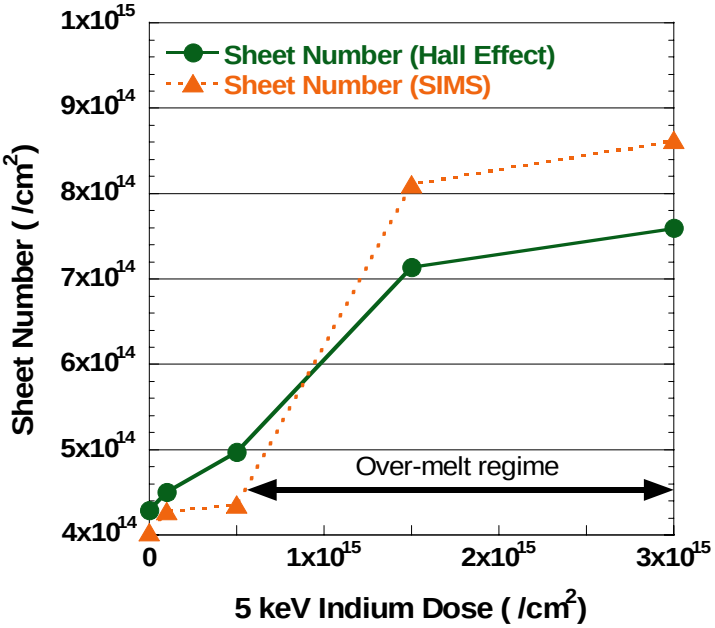

Figure 3-42 Sheet number as a function of 5 keV indium co-implant dose after the post-LTP anneal at 900 ^{o}C for 600 s for values measured by Hall Effect and calculated from SIMS depth profiles. Prior to the post-LTP anneal the samples are amorphized by a 1.0x10^{15} /cm^{2} dose of silicon implanted at 15 keV. Boron is implanted into the amorphous layer at 1 keV with a 3.0x10^{15} /cm^{2} dose. The layer is recrystallized by a laser energy density of 0.74 J/cm^{2}.

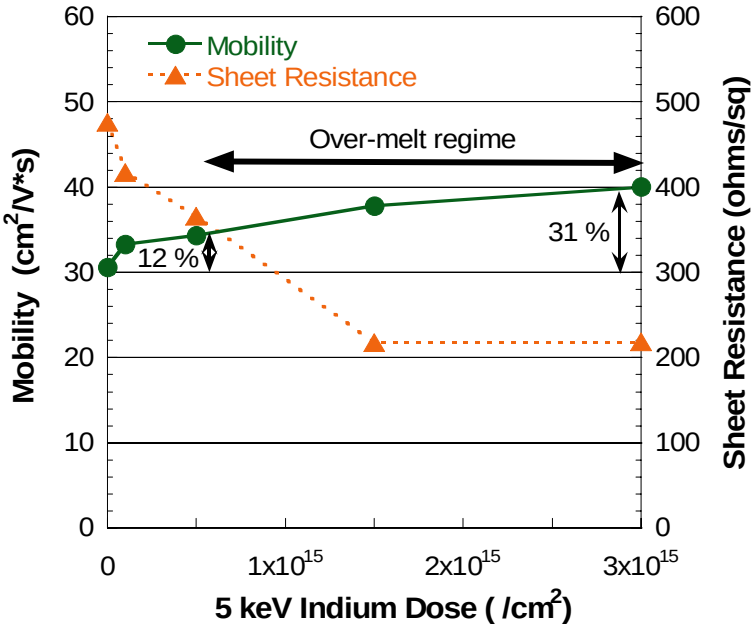

Figure 3-43 Carrier mobility measured by Hall Effect and sheet resistance measured by Four-Point Probe as a function of 5 keV co-implant indium dose after the post-LTP anneal at 900 ^{o}C for 600 s. Prior to the post-LTP anneal the samples are amorphized by a 1.0x10^{15} /cm^{2} dose of silicon implanted at 15 keV. Boron is implanted into the amorphous layer at 1 keV with a 3.0x10^{15} /cm^{2} dose. The layer is recrystallized by a laser energy density of 0.74 J/cm^{2}.

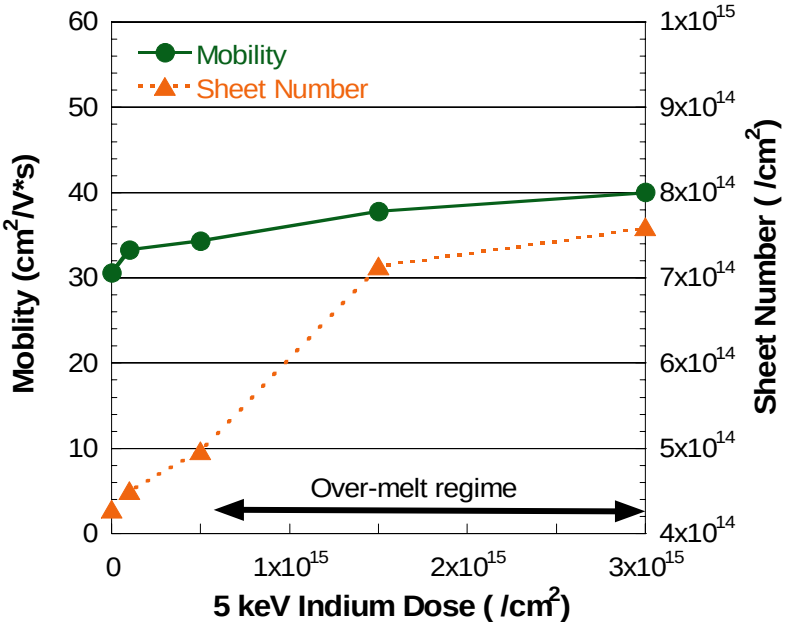

Figure 3-44 Mobility and sheet number measured by Hall Effect as a function of 5 keV co-implant indium dose after the post-LTP anneal at 900 ^{o}C for 600 s. Prior to the post-LTP anneal the samples are amorphized by a 1.0x10^{15} /cm^{2} dose of silicon implanted at 15 keV. Boron is implanted into the amorphous layer at 1 keV with a 3.0x10^{15} /cm^{2} dose. The layer is recrystallized by a laser energy density of 0.74 J/cm^{2}.

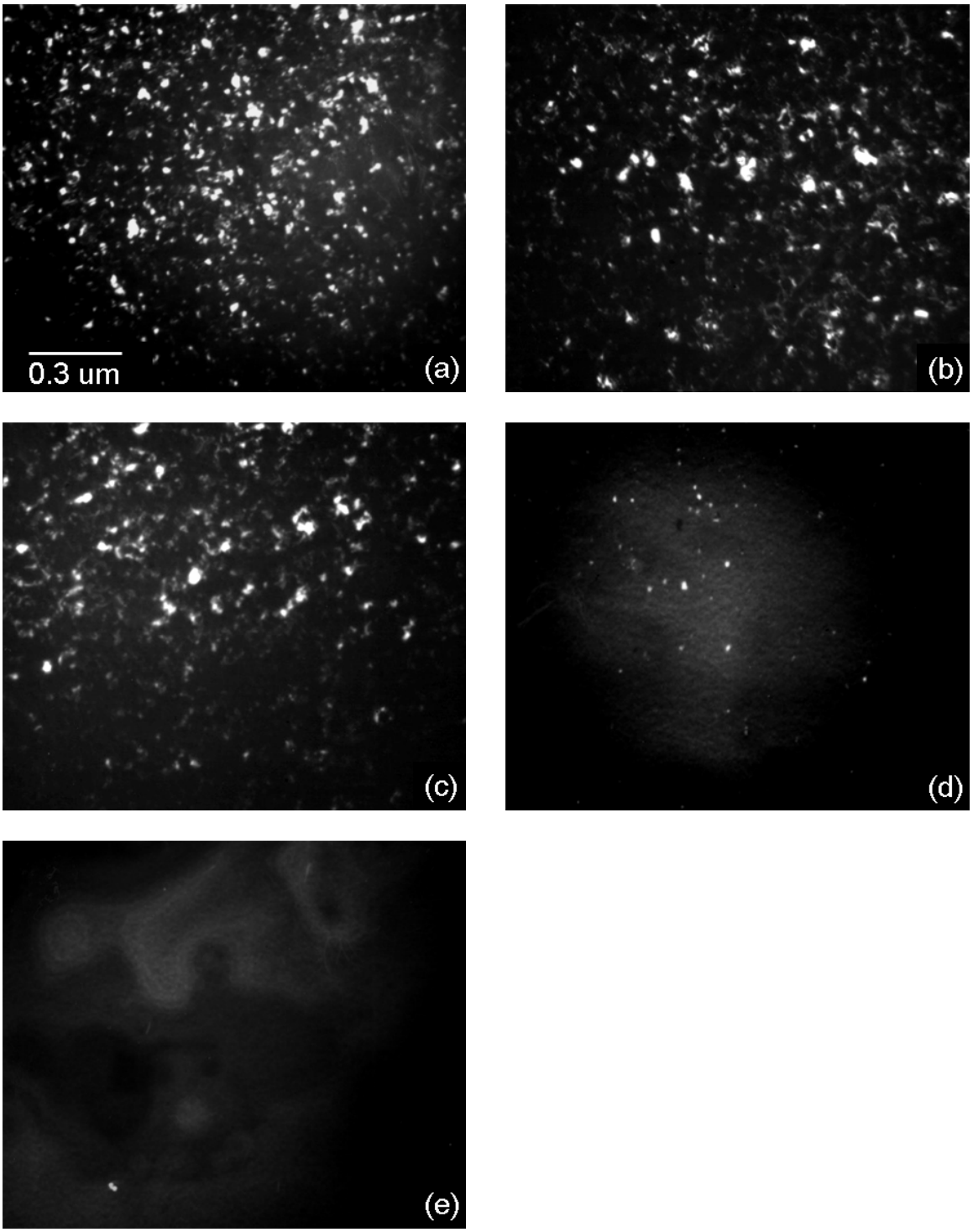

Figure 3-45 PTEM defect micrographs after annealing at 900 ^{o}C for 60 s as a function of 5 keV co-implant indium dose: (a) $0.0x10^{00}$, (b) $1.0x10^{14}$, (c) $5.0x10^{14}$, (d) $1.5x10^{15}$ and (e) $3.0x10^{15}$ /cm^2. Prior to the post-LTP anneal the samples are amorphized, implanted with boron and recrystallized by a laser energy density of 0.74 J/cm^2.

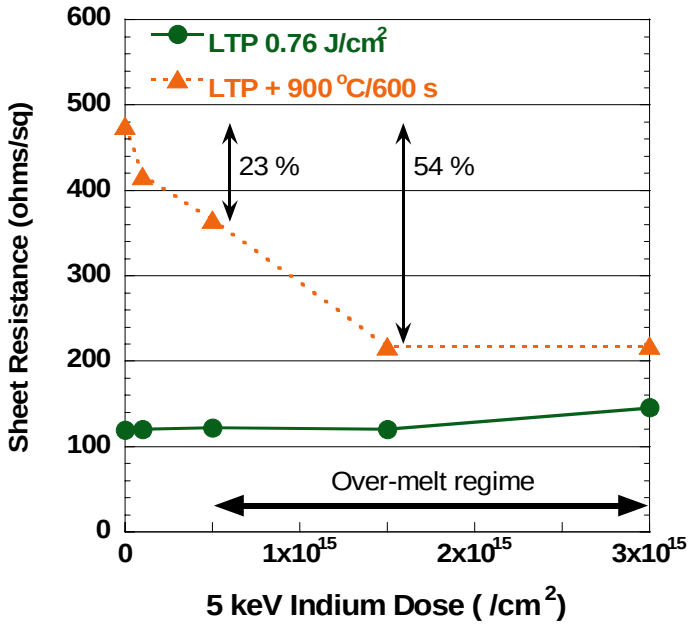

Figure 3-46 Sheet resistance measured by Hall Effect as a function of 5 keV indium co-implant dose after LTP at an energy density of 0.74 J/cm^2 and again after the post-LTP anneal at 900 ^{o}C for 600 s. The samples are amorphized by a 1.0x10^{15} /cm^2 dose of silicon implanted at 15 keV. Boron is implanted into the amorphous layer at 1 keV with a 3.0x10^{15} /cm^2 dose. The layer is recrystallized by a laser energy density of 0.74 J/cm^2.

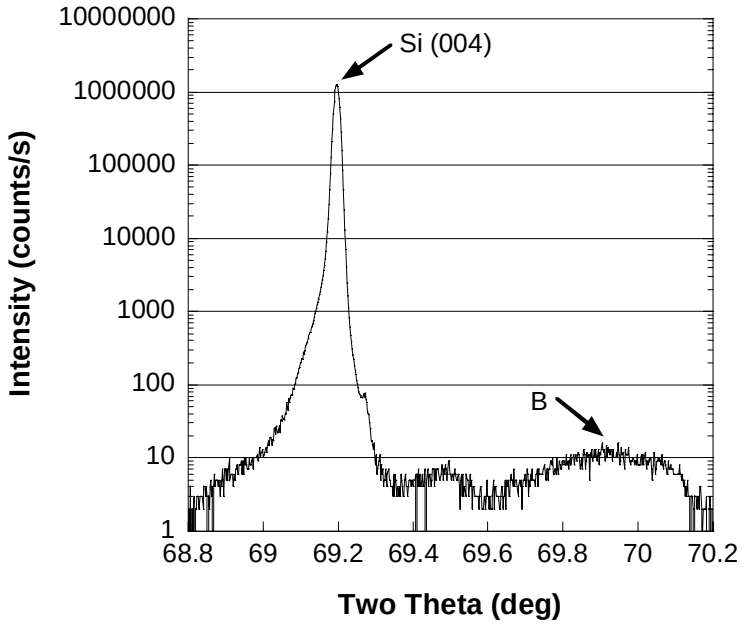

Figure 3-47 HR-XRD rocking curve measured after LTP, for the control sample (no co-implanted indium) preamorphized with 15 keV silicon $1.0x10^{15}$ /cm^2, implanted with 1 keV boron $3.0x10^{15}$ /cm^2 and recrystallized by a laser energy density of 0.74 J/cm^2.

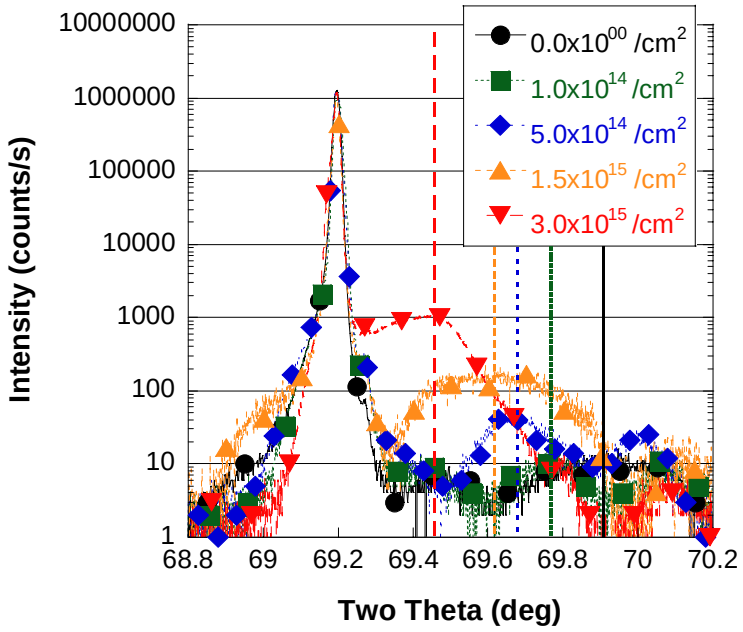

Figure 3-48 HR-XRD rocking curves measured after LTP, for junctions preamorphized with a 15 keV silicon $1.0x10^{15}$ /cm^2, implanted with 1 keV boron $3.0x10^{15}$ /cm^2 and 5 keV indium at doses of $0.0x10^{00}$ (control), $1.0x10^{14}$, $5.0x10^{14}$, $1.5x10^{15}$ and $3.0x10^{15}$ /cm^2. The implanted layer is irradiated with an energy density of 0.74 J/cm^2.

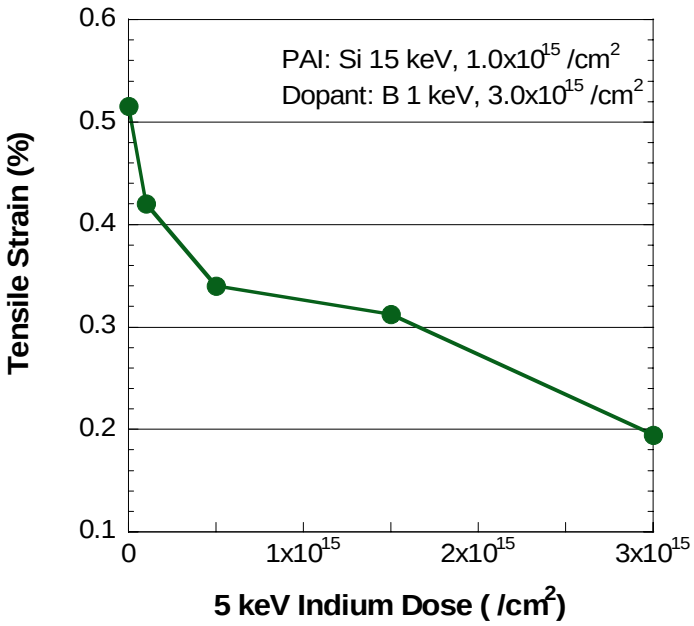

Figure 3-49 Strain calculated from differences in lattice parameter as measured by HR-XRD rocking curve analysis as a function of indium co-implant dose after LTP at an energy density of 0.74 J/cm^2. Junctions preamorphized with a 15 keV silicon 1.0x10^{15} /cm^2, implanted with 1 keV boron 3.0x10^{15} /cm^2 and 5 keV indium at doses of 0.0x10^{00} (control), 1.0x10^{14}, 5.0x10^{14}, 1.5x10^{15} and 3.0x10^{15} /cm^2.

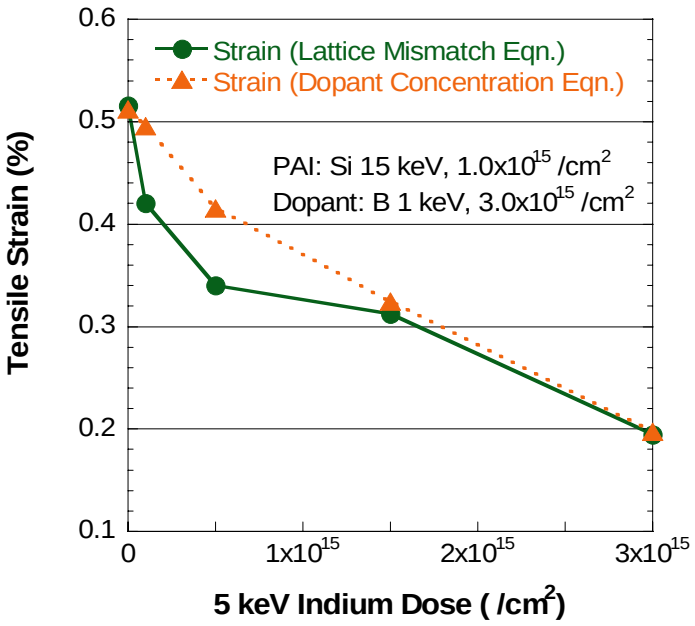

Figure 3-50 Strain calculated using the pseudomorphic lattice mismatch formula as well as the product of the lattice contraction coefficient and dopant concentration. For junctions preamorphized with a 15 keV silicon $1.0x10^{15}$ /cm^2, implanted with 1 keV boron $3.0x10^{15}$ /cm^2 and 5 keV indium at doses of $0.0x10^{0}$ (control), $1.0x10^{14}$, $5.0x10^{14}$, $1.5x10^{15}$ and $3.0x10^{15}$ /cm^2. The implanted layer is irradiated with an energy density of 0.74 J/cm^2.

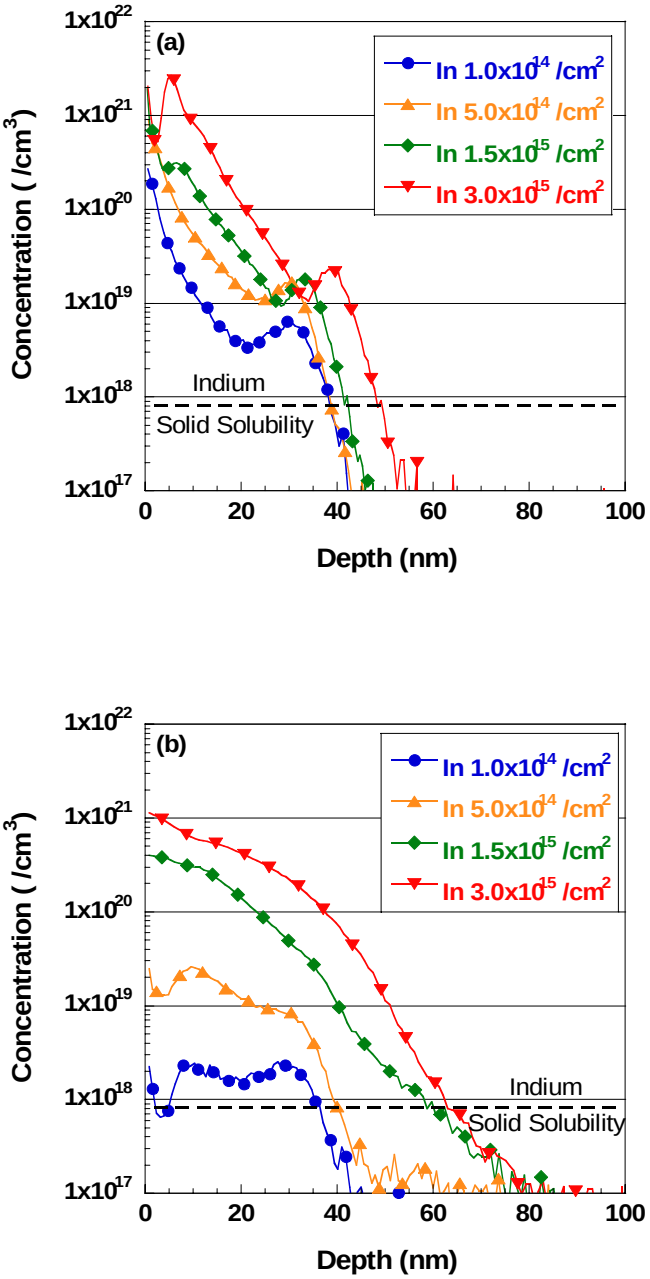

Figure 3-51 Indium depth profiles measured by SIMS for junctions implanted with 15 keV silicon 1.0×10^{15} /cm^2, 1 keV boron 3.0×10^{15} /cm^2 and 5 keV indium after a) LTP at an energy density of 0.74 J/cm^2 and b) subsequent post-LTP anneal at 900 ^{o}C for 600 s.

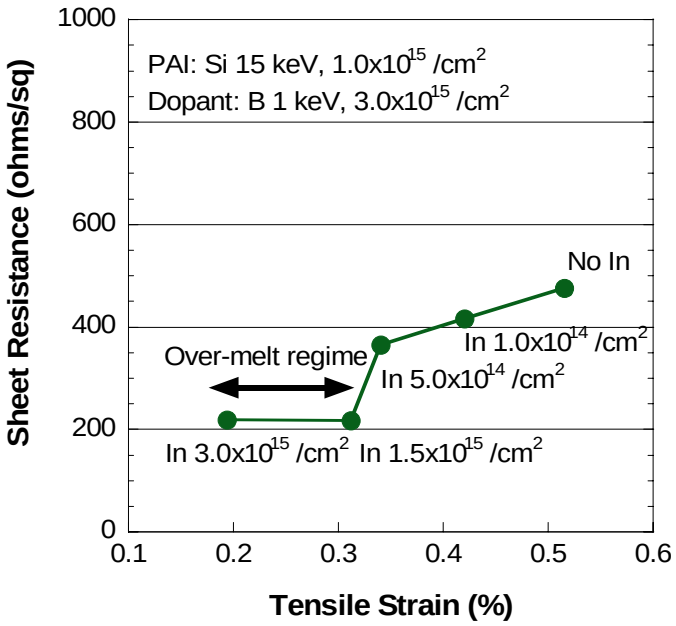

Figure 3-52 Comparison of sheet resistance measured by Four-Point Probe after the post-LTP anneal to strain calculated from HR-XRD rocking curve analysis as a function of indium co-implant dose. For junctions preamorphized with a 15 keV silicon $1.0x10^{15}$ /cm^2, implanted with 1 keV boron $3.0x10^{15}$ /cm^2 and 5 keV indium at doses of $0.0x10^{00}$ (control), $1.0x10^{14}$, $5.0x10^{14}$, $1.5x10^{15}$ and $3.0x10^{15}$ /cm^2. The implanted layer is irradiated with an energy density of 0.74 J/cm^2.

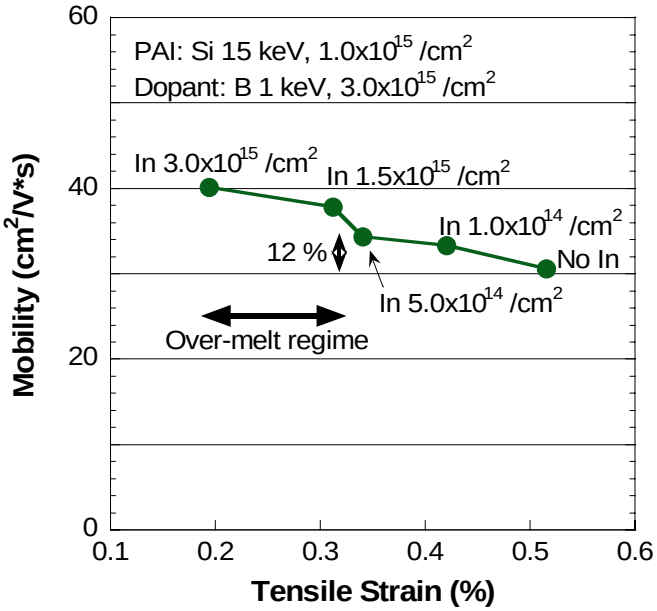

Figure 3-53 Comparison of carrier mobility measured Hall Effect after the 900 ^{o}C/600 s post-LTP anneal to strain calculated from HR-XRD rocking curve analysis as a function of indium co-implant dose. For junctions preamorphized with a 15 keV silicon 1.0x10^{15} /cm^2, implanted with 1 keV boron 3.0x10^{15} /cm^2 and 5 keV indium at doses of 0.0x10^{00} (control), 1.0x10^{14}, 5.0x10^{14}, 1.5x10^{15} and 3.0x10^{15} /cm^2. The implanted layer is irradiated with an energy density of 0.74 J/cm^2.

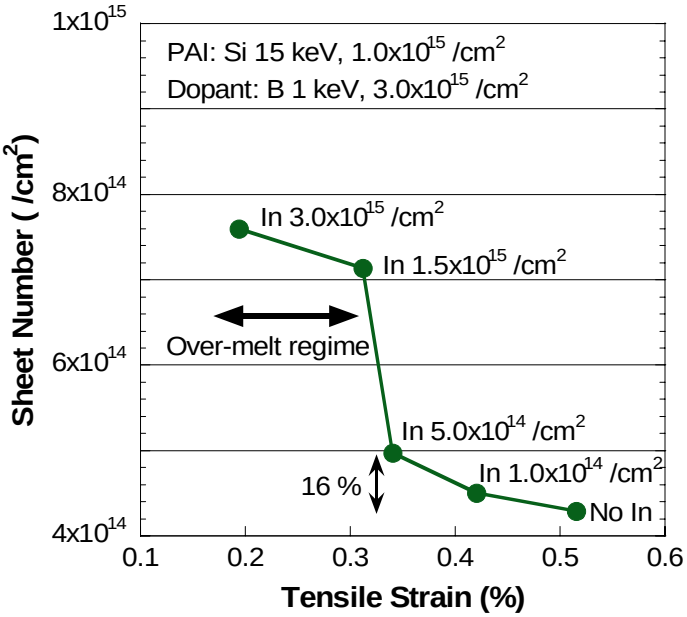

Figure 3-54 Comparison of sheet number measured by Hall Effect after the 900 ^{o}C/600 s post-LTP anneal to strain calculated from HR-XRD rocking curve analysis as a function of indium co-implant dose. For junctions preamorphized with a 15 keV silicon 1.0x10^{15} /cm^{2}, implanted with 1 keV boron 3.0x10^{15} /cm^{2} and 5 keV indium at doses of 0.0x10^{00} (control), 1.0x10^{14}, 5.0x10^{14}, 1.5x10^{15} and 3.0x10^{15} /cm^{2}. The implanted layer is irradiated with an energy density of 0.74 J/cm^{2}.

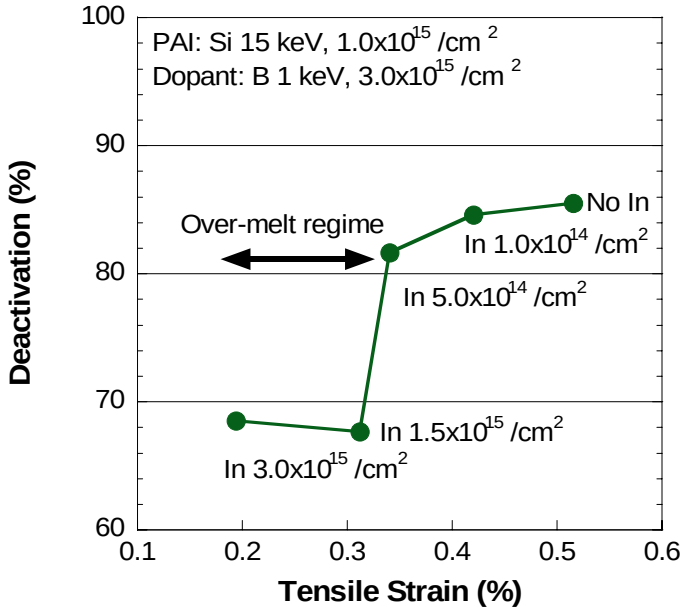

Figure 3-55 Carrier deactivation as a function of tensile strain. Deactivation is calculated as the percent difference between sheet number values measured before and after the post-LTP anneal. Strain is calculated from HR-XRD rocking curves as a function of indium co-implant dose prior to the post-LTP anneal. Junctions are preamorphized with a 15 keV silicon $1.0x10^{15}$ /cm^2, implanted with 1 keV boron $3.0x10^{15}$ /cm^2 and 5 keV indium at doses of $0.0x10^{00}$ (control), $1.0x10^{14}$, $5.0x10^{14}$, $1.5x10^{15}$ and $3.0x10^{15}$ /cm^2. The implanted layer is irradiated with an energy density of 0.74 J/cm^2.

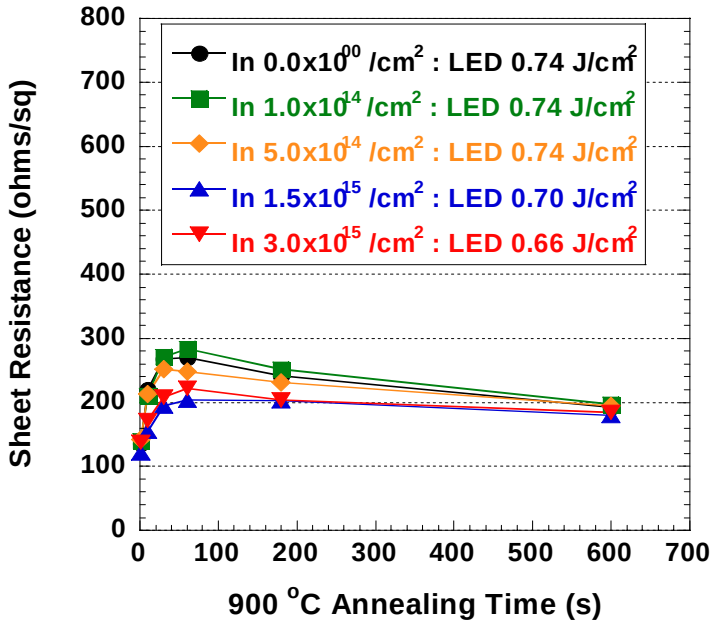

Figure 3-56 Sheet resistance measured by Four-Point Probe as function of annealing time at 900 °C for junctions implanted with 15 keV silicon $1.0x10^{15}/cm^2$, 1 keV boron $3.0x10^{15}/cm^2$ and 5 keV indium at doses of $0.0x10^{00}$, $1.0x10^{14}$, $5.0x10^{14}$, $1.5x10^{15}$ and $3.0x10^{15}/cm^2$ after laser annealing with energy densities adjusted for the indium dose effect on the process window.

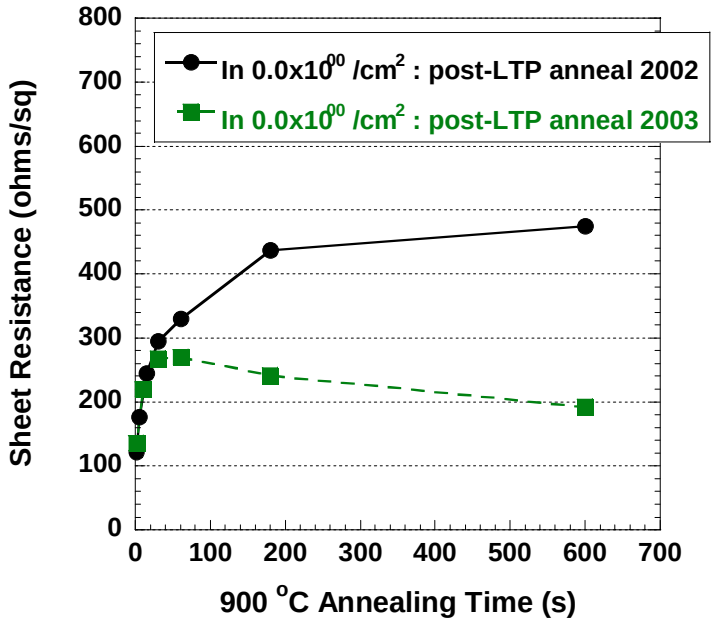

Figure 3-57 Sheet resistance measured by Four-Point Probe as function of annealing time at 900 ^{o}C for identical junctions with the exception of date that the post-LTP anneals are performed. Junctions are preamorphized by a 15 keV silicon implant with a 1.0x10^{15} /cm^2 dose. The amorphous layer is implanted with boron at 1 keV with a dose of 3.0x10^{15} /cm^2. The doped amorphous layer is regrown and activated by a laser energy density of 0.74 J/cm^2.

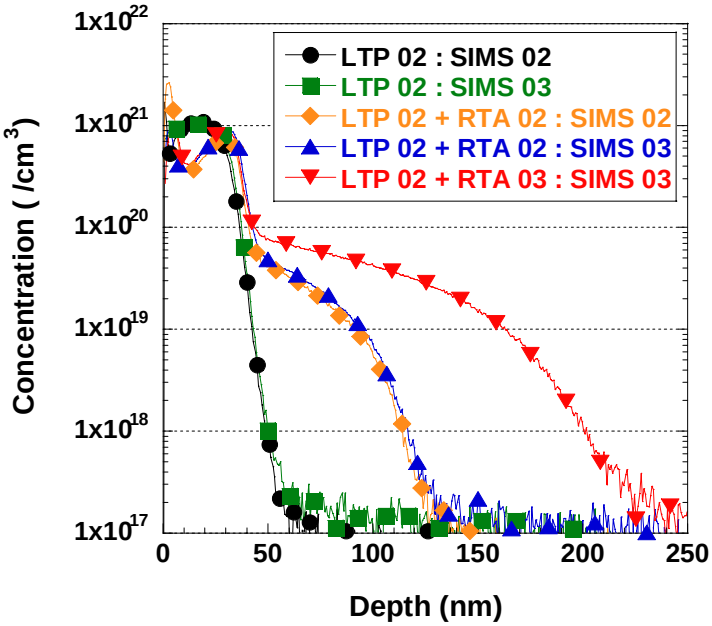

Figure 3-58 Boron depth profiles for identical junctions with the exception of the date the RTA and SIMS analysis is preformed. Junctions are preamorphized with a 15 keV silicon $1.0x10^{15}$ /cm^2, implanted with 1 keV boron $3.0x10^{15}$ /cm^2 and 5 keV indium at doses of $0.0x10^{00}$ (control), $1.0x10^{14}$, $5.0x10^{14}$, $1.5x10^{15}$ and $3.0x10^{15}$ /cm^2. The implanted layer is irradiated with an energy density of 0.74 J/cm^2.

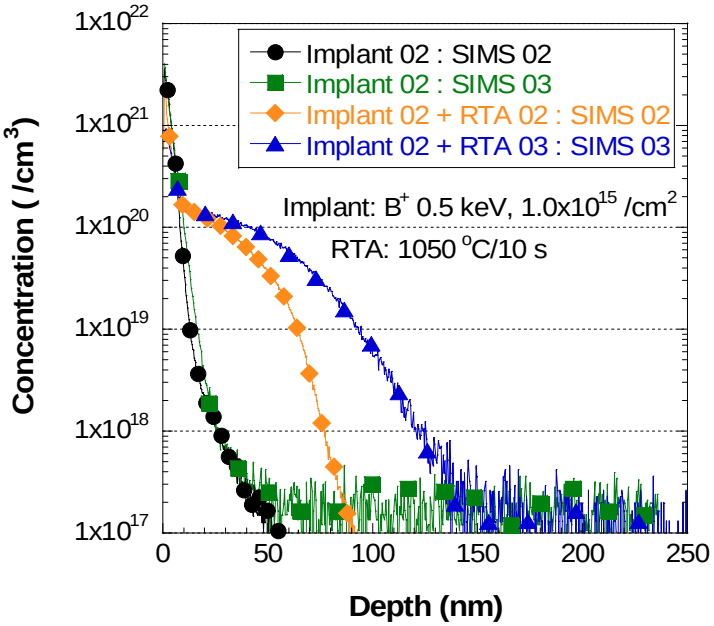

Figure 3-59 Boron depth profiles for identical junctions with the exception of the date the RTA and SIMS analysis is preformed. Junctions are formed by implanting boron at 0.5 keV with a dose of 1.0×10^{15} /cm^2. The subsequent RTA is 1050 ^{o}C for 10 s.

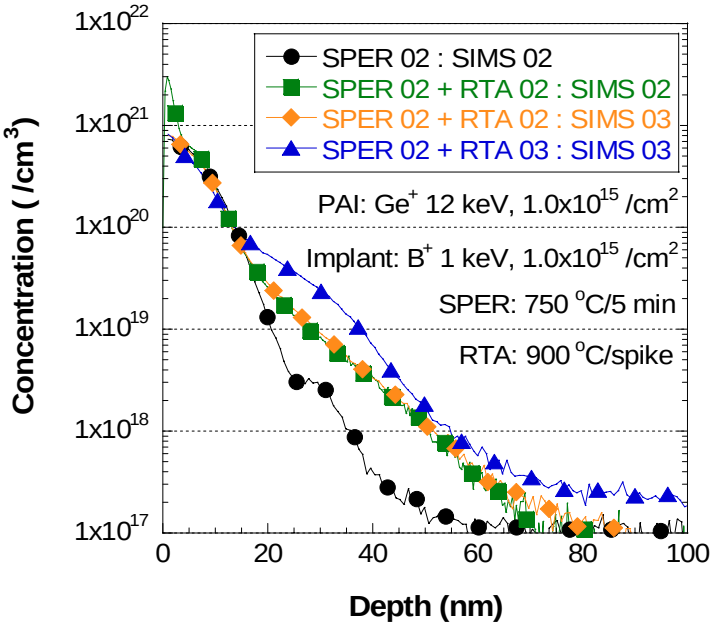

Figure 3-60 Boron depth profiles for identical junctions with the exception of the date the RTA and SIMS analysis is preformed. Junctions are preamorphized by a 12 keV germanium implant with a $1.0x10^{15}$ /cm^2 dose. The amorphous layer is implanted with boron at 0.5 keV with a dose of $1.0x10^{15}$ /cm^2. Solid phase epitaxial regrowth of the amorphous layer is achieved by 750 ^{o}C anneal for 5 min. The subsequent RTA is a 950 ^{o}C spike.

CHAPTER 4
CONCLUSIONS

Alternate Dopants

Alternate dopants can be activated above solid solubility by laser thermal processing. However, greater activation and low sheet resistance is realized for the conventional dopants. Additionally, while deactivation is effected by dopant species, alternate dopants do not offer favorable deactivation over that of conventional dopants after a 900 ^{o}C/300 s anneal. Based on the electrical data after LTP and again after the post-LTP anneal, the conventional dopants of boron and arsenic out perform their respective p- and n-type alternate dopant counter parts investigated in this study. It is also found that dose of the dopant alters the process window due to a decrease in the total reflectivity.

Co-Implants

Co-implantation of boron with indium alters the deactivation of junctions formed by melt laser thermal processing. Additionally, the dose of the co-implanted indium alters the process window, resulting in an effective increase in laser energy densities with increased indium co-implant dose. For similar junctions doped with equivalent boron dose and irradiated with the approximately the same laser energy density, increasing the indium co-implant doses dose not improve the sheet resistance after LTP. In contrast, after the post-LTP anneal the sheet resistance is suppressed with increasing dose of co-implanted indium. Due to over-melt induced at high doses of co-implanted indium a portion of the suppression is attributed to phenomena associated with over-melt.

However, for the low doses of indium, ranging from the control with no indium to a dose of $5.0x10^{15}$ /cm^2, there is a suppression of the sheet resistance with increasing indium co-implant dose that is due to a reduction in the deactivation of the active dopant population during the post-LTP anneal. Based on the methodical exclusion of other potential sources and correlation between reduced deactivation and increased strain compensation, the data supports, for low doses of indium, that the suppression of the sheet resistance is the result of strain compensation induced by the co-implantation of indium.

CHAPTER 5
LASER THERMAL PROCESSING SIMULATIONS

The current chapter describes the conceptual basis and development of a flexible model for treating laser induced heating and associated diffusion of dopants. The purpose of the chapter is not simulate the phenomena observed in previous chapters, but to provide a record of current work and starting point for future work. At the current stage of development, the FLOOPS script implementing this model can only address limited cases of laser solid interactions. Continued development of the script is necessary to accurately apply the approaches describe herein to experimental data.

Introduction

The work herein describes the mathematical and logic models implemented to simulate heat transfer, phase change and atomic diffusion arising from pulsed irradiation of semiconductors. Laser thermal processing of materials has been proposed as a direct means of activating implanted dopants and forming highly activated, abrupt, shallow junctions without heating the bulk silicon. Prior to the current work, Heating5 [92], LIMP [68] and Laser8 [93], were developed to simulate laser induced melting and solidification of materials. However, these codes all neglect the diffusion of dopant species, which is fundamental to junction formation. The script under development implements successful melt and solidification concepts from previous models, and augments them with additional code to account for the diffusion of dopant species. Additionally, the current script is coded using the Florida Object Oriented Process

Simulator, thus allowing laser thermal processing of virtual structures created using FLOOPS processing commands.

General Assumptions and Boundary Conditions

The laser-irradiated sample is modeled as a two-dimensional solid composed of user-defined mesh.

General assumptions:

- Energy transfer from the laser to the material lattice occurs instantaneously in comparison to the pulse duration [94].
- Constant absorption coefficient for all temperatures.
- No re-melt after primary solidification.
- Constant material density for all temperatures
- Latent Heat of phase transformation is distributed across the time increment of transformation.

Boundary conditions:

- No temperature distribution in the sample at time zero.
- No loss of heat at any time from the irradiated surface.
- As depth of the sample goes to infinity, the temperature is a constant.
- Latent heat is released so quickly that the interface velocity is only limited by the rate of heat conduction away from the interface (Stefan Boundary Condition or Heat flow limited).

Heat Transfer

Heat Flow Equation

The heat flow equation is solved using an enthalpy formulation. The approach of using an enthalpy formation of heat flow was originally developed by Rose and later

implimented by Geist et al. [95]. Using Rose's scheme, the phase or state of a material volume is based on the enthalpy rather than the temperature. Allowing a phase change to occur at any temperature, with the practical result being that overheating and undercooling can be included if desired. To realize the full flexibility of this method, the changes of phase and state, and the conditions at which they occur, are specified by a state array [34, 96].

Conversion of the differential equation from temperature as a function of depth and time into an equation for enthalpy is is performed by Geist et al. [95] and reproduced here for clarity. The equation for enthalpy is directly derived from the energy balance condition. In integral form the condition is given by

$$\frac{d}{dt}\int_V \rho \cdot e \cdot dv = \int_V S \cdot dv + \int_A k \cdot \nabla T \cdot \vec{n} \cdot da \qquad \text{Eqn. 5.1}$$

in which ρ is the density, *e* the internal energy, and *k* the thermal conductivity in a differntial volume element *dv*. *S* is the heat generation function describing the effects of the laser irradiation and *n* is an outwardly directed unit vector normal to the element of area *da*. The left hand side of Eqn. 5.1 is the rate of change of the energy stored in the volume *V*, the first term on the right hand side is the rate at which energy is generated by the laser pulse and the second term is the rate of change of the stored energy due to conduction in and out of area *A* through the surface bounding *V*.

Enthalpy *h*, is related to the internal energy and the pressure *p* by the equation

$$e = h - p/\rho \qquad \text{Eqn. 5.2}$$

which when substituted into Eqn. 5.1 yields

$$\frac{d}{dt}\int_V \left[\rho \cdot h - p\right] \cdot dv = \int_V S \cdot dv + \int_A k \cdot \nabla T \cdot \vec{n} \cdot da \qquad \text{Eqn. 5.3}$$

Pressure is assumed to be independent of time during a phase change (isobaric), consequently Eqn. 5.3 becomes

$$\frac{d}{dt}\int_V \rho \cdot h \cdot dv = \int_V S \cdot dv + \int_A k \cdot \nabla T \cdot \vec{n} \cdot da \qquad \text{Eqn. 5.4}$$

Application of the divergence theorem to the second term on the right hand side and interchange of the order of integration and differentiation yields

$$\int_V \frac{d}{dt} \rho \cdot h \cdot dv = \int_V S \cdot dv + \int_V \nabla \cdot \left(k \cdot \nabla T\right) \cdot dv \qquad \text{Eqn. 5.5}$$

Eqn. 5.5 is valid for any volume element, consequently, the enthalpy equation is described as follows

$$\frac{d}{dt}\left(\rho \cdot h\right) = \nabla \cdot \left(k \cdot \nabla T\right) + S \qquad \text{Eqn. 5.6}$$

In one dimension Eqn. 5.6 simplifies to

$$\frac{d}{dt}\left(\rho \cdot h\right) = \frac{d}{dx} \cdot \left(k \frac{dT}{dx}\right) + S \qquad \text{Eqn. 5.7}$$

Additionally, since ρ is not strong function of temperature for silicon, it is assumed constant with time, thus simplifying Eqn. 5.7 to

$$\frac{d}{dt} h = \frac{d}{dx} \cdot \left(k \frac{dT}{dx}\right) + S \qquad \text{Eqn. 5.8}$$

which is the starting point for discretization.

Interaction of the Laser with the Sample

The laser itself is characterized by an instantaneous intensity (W/cm^2) and an integrated intensity or pulse energy (J/cm^2). The laser interacts with the sample in one of two ways. Laser intensity is reflected in the near surface region or absorbed by the bulk. Reflected intensity is not translated to thermal energy. In contrast, intensity absorbed through phonon generation translates to thermal heating, thus constituting the source term

S in Eqn. 5.8. The source term is a function of both time and depth. For constant absorbance (linear regime), the amount of energy penetrating to a particular depth *x* at time *t* is approximated by

$$S(x,t) = (1 - R(x,t)) \cdot P(t) \cdot \alpha \cdot e^{-\alpha x} \qquad \text{Eqn. 5.9}$$

where *R(x,t)* is the reflectivity of sample surface and *P(t)* is time variation of the laser pulse intensity. Refection of intensity from the material is not purely a surface phenomenon and can therefore be a function of depth as well as time. For simplicity, reflectivity is assumed a function of time alone, as *R* changes with temperature and phase of the surface material. Separation of the absorbance function into time-dependant and depth-dependant factors is not taking into consideration. The laser pulse *P(t)* is approximated as a Gaussian profile. A typical laser pulse shape of intensity versus time is shown in Figure 1-6.

Diffusion

Diffusion is the thermally driven random motion of particles in three dimensions. The driving force for intrinsic diffusion of atoms is a concentration gradient. For example, when the concentration of atoms is homogeneous and their motion is isotropic, the flux of the atoms in any one direction is on average balanced by an equal flux in the opposite direction. In contrast, in the presence of a concentration gradient the random motion results in the net transport of atoms in the direction of decreasing concentration. Specifically, the probability for a particle to move in any direction is identical, but due to the concentration gradient there is a larger population of atoms available to move from the higher concentration region to the low concentration region, hence there exists a statistical net flux of atoms in the direction of decreasing concentration.

Diffusion of an atom can be described mathematically by Fick's laws of diffusion. Fickian diffusion is applicable when diffusion exhibits simple behavior, where diffusion is isotropic and independent of concentration. Fick's first law of diffusion relates the number of atoms passing through a unit area per unit time, termed flux, to the concentration gradient. In one dimension the Fick's first law is expressed by

$$j_n = -D\frac{\partial C}{\partial x} \qquad \text{Eqn. 5.10}$$

where C is the impurity atom concentration, j_n is the flux, D is the diffusion coefficient or diffusivity, $\partial C/\partial x$ is the concentration gradient over a distance ∂x. The negative sign of the left hand side of the equation accounts for the diffusion flux being in the opposite direction of the concentration gradient. At any two points as a function of depth, the flux of solute atoms is different, unless the gradient of the concentration profile is the same. Consequently, for a region with a concentration gradient, the difference in the flux of solute atoms entering j_1 and leaving j_2 over a time interval Δt leads to a small increase in the local concentration

$$\Delta C \cdot A \cdot \Delta x = (j_1 - j_2) \cdot A \cdot \Delta t \qquad \text{Eqn. 5.11}$$

where A is the cross-sectional area of the flux surface. For $\Delta x = x_2 - x_1$ being very small, Eqn. 5.11 simplifies to

$$j_2 = j_1 + \frac{\partial j}{\partial x}\Delta x \qquad \text{Eqn. 5.12}$$

In the limit of Δx and Δt tending towards zero, the following relationship is obtained

$$\frac{\partial C}{\partial t} = -\frac{\partial J}{\partial x} = -\frac{\partial}{\partial x}\left(D\frac{\partial C}{\partial x}\right) \qquad \text{Eqn. 5.13}$$

Eqn. 5.13 is known as Fick's Second Law, and is generally applicable if the diffusion coefficient is taken to depend on composition. In the special case where D is independent of composition, the equation simplifies to

$$\frac{\partial C}{\partial t} = D \cdot \frac{\partial^2 C}{\partial x^2} \qquad \text{Eqn. 5.14}$$

Fick's Second Law can be understood as a reduction in curvature, since the second differential with respect to distance is the curvature of the profile. If the profile curves downwards (gradient decreasing) then the concentration reduces with time. Conversely, a positive curvature (increasing gradient) results in an increase in concentration. In both cases, the concentration is tending towards zero curvature where there is no change in composition.

Diffusivity or diffusion coefficient is a function of atom, medium and temperature. Diffusion of an atom is defined by diffusivity, which is the ease atom moves through a medium. In an ideal case the temperature dependency of diffusivity is described by an Arhenius expression of the form

$$D(T) = D_0 \cdot e^{-E_A/k \cdot T} \qquad \text{Eqn. 5.15}$$

where D_0 is a measure of the frequency at which an atom attempts to jump over an energy barrier, and the exponential term (Boltzman factor) represents the probability that a solute atom will have energy equal to or in excess of the activation energy E_A. Both D_0 and the exponential term are temperature dependant, however, since the exponential term changes much more rapidly with temperature, D_0 is approximated as a constant for small temperature ranges.

Discretization

The mesh is a framework for describing the sample. The mesh consists of nodes, which are locations in space that discretize the sample. Each node can be defined with physical properties (thermal conductivity or heat capacity) and define boundary conditions (surface). The node is also a computational point at which the numerical expressions are solved. The spacing between nodes determines the spatial resolution between solutions. For the laser thermal annealing simulation, the mesh is defined as an amorphous silicon layer on a silicon substrate. The spacing in the amorphous layer is set to five angstroms, which is approximately the distance between silicon atoms in crystalline silicon.

Material State

State Diagrams

State of a material is determined by state diagrams. Figure 5-1 is a partial form of the state diagram for silicon. The state diagram is constructed in terms of temperature and enthalpy in order to utilize Rose's scheme. For a specified enthalpy the temperature and state of the material is known. In the case of crystalline or liquid silicon an increase in enthalpy corresponds to an increase in temperature. However, during the transition between crystalline and liquid states, the temperature is stagnant with changing enthalpy. The change in state at a constant temperature corresponds to the evolution of latent heat. The region of constant temperature over which the transformation occurs is termed mush.

Transition States

From the standpoint of a finite difference calculation, it is convenient to use transitions states such as mush. A node undergoes a transition when the material composing the node changes from on state to another. For example, a node that has more

enthalpy than crystalline silicon, but less than liquid is in a transition state. Since the node is neither completely crystalline nor solid is termed mush. The crystalline to liquid fraction is determined by the amount of latent heat in the node relative to the total amount of latent heat involved in the state change. During the state transition, the fraction continues to change as a function of latent heat until the transition is complete.

State Arrays

In conjunction with the state diagram the state array summarizes the conditions under which a transition can occur. A fundmental criteria of the state array is that all processes involved conserve engery. The state array is used only for bookkeeping; implementation of the state array in the script is made by way of logic statements. Table 5-1 depicts the state array for transition of material between solid and liquid states in reference to the state diagram (Figure 5-1). This simplified state array is only valid for melting and crystallization of a single material, overheating and under cooling effects are neglected. Diagonal elements of the array are blank because no transition occurs for (c : c), (l : l) and (m : m). The (c, l) and (l, c) elements are blank signifying that all transitions between crystalline and liquid must go through an intermediate mushy state. Transitions associated with the melting and crystallization process are given in the following expression

$$c \Leftrightarrow m \Leftrightarrow l \qquad \text{Eqn. 5.16}$$

Referring to Table 5-1, a material that is originally crystalline (row c) transitions to mush (column m) only if the enthalpy E as depicted in Figure 5-1 is greater than E_c. If the E of the mushy material (row m) drops below E_c the material becomes crystalline (column c). Alternatively, if the E of the mushy material (row m) continues to rise and exceeds E_{lc} the

material transitions to liquid (column l). Complexity of the state array can be increased to account for the multiple states and or additional criteria associated with changes in state.

Table 5-1 State array for simple case of transition in state between solid and liquid. The nomenclature is as follows: c-crystalline, m-mush and l-liquid.

	c	m	l
c		$E>E_c$	
m	$E<E_c$		$E>E_{lc}$
l		$E<E_{lc}$	

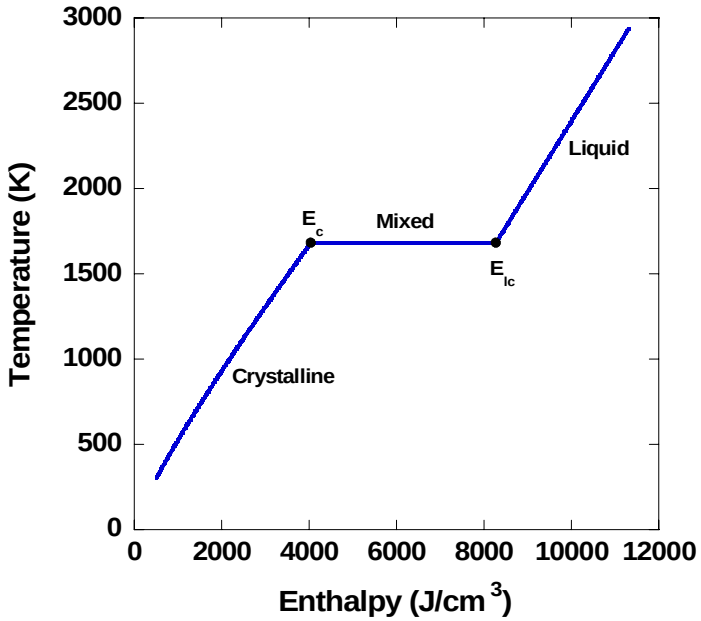

Figure 5-1 State diagram for crystalline silicon.

APPENDIX A
LIST OF ACRONYMS AND DEFFINITIONS

FLOOPS: FLorida Object Oriented Process Simulator

Front-end-processing: All processes before the fist metallization.

HR-XRD: High Resolution X-Ray Diffraction

LTP: Laser Thermal Processing

MOS: Metal Oxide Semiconductor

MOSFET: Metal Oxide Semiconductor Field Effect Transistor

Node: Technology generation spanning a duration of approximately three years

PTEM: Plan-View Transmission Electron Microscopy

RTP: Rapid Thermal Anneal

SIMS: Secondary Ion Mass Spectrometry

Spike: A rapid thermal anneal that has rapid ramp-up and ramp-down times with a short dwell time at temperature.

SWAMP: SoftWare and Analysis of advanced Material Processing

TEM: Transmission Electron Microscopy

UV/Vis: Ultraviolet Visible Spectrometer

XTEM: Cross-Sectional Transmission Electron Microscopy

APPENDIX B
SAMPLE SIMULATION CODE

```
proc Init {} {
 line x loc=0 spacing=0.0005 tag=1
 line x loc=0.03 spacing=0.0005 tag=2
 line x loc=10 spacing=1 tag=3
 region silicon xlo=1 xhi=2
 region silicon xlo=2 xhi=3
 init quiet

        ## Amorphous Depth, A0 (um)
        global A0
        set A0 0.02
}
Init


#### LASER PULSE ####

        ## Artificial time for Gaussian
        math diffuse dim=1 umf col none scale
        solution add name = tt solve negative
        pdbSetString Si tt Equation "ddt(tt) - 1"
        pdbSetDouble Si tt  Abs.Error 1.0e-15
        sel z=1e-10 name=tt store
        set Dt0 {tt-Begtt}
        term name=Dt0 add silicon eqn=$Dt0

        ## Location on the Abcissa of the Pulse Peak, u (seconds)
        set u 40.0e-9

        ## Pulse Full Width Half Maximum, FWHM (seconds)
        set FWHM 10.0e-9

        ## Standard Deviation, s (seconds)
        set s [expr $FWHM/(sqrt(8*log(2)))]

        ## Laser Fluence, LF (J/cm^2)
        set LF 1.0

        ## Guassian Laser Intensity, LI (W/cm^2)
```

```
set LI {$LF*(1/(2*3.14*$s^2)^0.5)*exp(-((tt-$u)^2/(2*$s^2)))}
term name=LI add silicon eqn=$LI

## Reflectivity, R (unitless)
set R 0.562

## Absorptivity, a (1/cm)
set a 1.38e6

## Laser Power Density, LPD (W/cm^3)
set LPD {LI * (1 - $R) * $a  * exp(-$a * x * 1.0e-4)}
term name=LPD add silicon eqn=$LPD


#### MATERIAL PROPERTIES ####

## Specifice Heat, Cp1 (J/K*cm^3)
set Cp {0.5743*log(TT)-1.8019}
term name=Cp add silicon eqn=$Cp
set Cp1 2.367
term name=Cp1 add silicon eqn=$Cp1

## Density, p (g/cm^3)
set p 2.33

## Thermal Conductivity, k0 (W/cm*K)
set k1 {(PA2==30)?(1.4):(0)}
term name=k1 add silicon eqn=$k1
set k2 {(PA2==25)?((1-MF)*5125.0*exp(-1.3953*log(TT))+MF*1.4):(0)}
term name=k2 add silicon eqn=$k2
set k4 {(PA2==20)?(5125.0*exp(-1.3953*log(TT))):(0)}
term name=k4 add silicon eqn=$k4
set k0 {k1+k2+k4}
term name=k0 add silicon eqn=$k0

## Amorphous Melting Temperature, TMA (K)
set TMA 1430.0
term name=TMA add silicon eqn=$TMA

## Crystalline/Liquid Transition Temperature, TMC (K)
set TMC 1685.0
term name=TMC add silicon eqn=$TMC

## Latent Heat of Fusion
set LHF 4206.0
term name=LHF add silicon eqn=$LHF
```

```
#### MATERIAL PHASE ####

        ## For phase determination Cp is constant at the melt temperature "Cp1"

        ## Phase Determination, PA2 (A=10, AL=15, C=20, CL=25, L=30)
        sel z=11 name=PB0 store
        set PB {(PB0<=26)?(1):(2)}
        term name=PB add silicon eqn=$PB
        set P1 {(HH<TMC*Cp1)?(20):(0.0)}
        term name=P1 add silicon eqn=$P1
        set P2 {(HH>=TMC*Cp1 && HH<LHF+TMC*Cp1)?(25):(0.0)}
        term name=P2 add silicon eqn=$P2
        set P3 {(HH>LHF+TMC*Cp1)?(30):(0.0)}
        term name=P3 add silicon eqn=$P3
        set PA {P1+P2+P3}
        term name=PA add silicon eqn=$PA

        sel z=11 name=PB1 store
        set PB2 {(PB1<=26)?(1):(2)}
        term name=PB2 add eqn=$PB2
        set P21 {(BegHH<TMC*Cp1)?(20):(0.0)}
        term name=P21 add silicon eqn=$P21
        set P22 {(BegHH>=TMC*Cp1 && BegHH<LHF+TMC*Cp1)?(25):(0.0)}
        term name=P22 add silicon eqn=$P22
        set P23 {(BegHH>LHF+TMC*Cp1)?(30):(0.0)}
        term name=P23 add silicon eqn=$P23
        set PA2 {P21+P22+P23}
        term name=PA2 add silicon eqn=$PA2

        ## Phase Change, PC (C:M=-5, C:L=-10, L:C=+10, L:M=+5)
        set PC {PA2-PA}
        term name=PC add silicon eqn=$PC

        ## Melt Fraction, MF (solid=0, melt=1)
        set MF {(PA==25)?((HH-TMC*Cp1)/LHF):(0)}
        term name=MF add silicon eqn=$MF

        ## Phase Data File
        global Ph
        set Ph [open matphase w]


#### ENTHALPY PROFILE ####
```

```
        ## Enthalpy Profile, HH (J/cm^3)
        solution add name = HH solve negative
        pdbSetString Si HH Equation "ddt(HH) - k0 * grad(TT) - LPD"
        pdbSetDouble Si HH  Abs.Error 1.0e-3
        ## Substrate Temperature
        sel z=300*Cp1 name=HH

        ## Temperature Profile, T (K)
        solution add name = T solve negative
        pdbSetString Si T Equation "ddt(T*Cp) - k0 * grad(HH/Cp) - LPD"
        pdbSetDouble Si T  Abs.Error 1.0e-3
        ## Substrate Temperature
        sel z=300 name=T

        ## Enthalpy conversion to Temperature, TT (K)
        set TT {(PA==25)?(TMC):((PA==30)?((HH-LHF)/Cp1):(T))}
        term name=TT add silicon eqn=$TT

#### BUSY WORK ####

        set Pi 3.14159
        set freq1 1.0e9
        set freq2 1.0e9
        set err  1.0e-5

        solution add name = Sin solve negative
        solution add name = Cos solve negative

        pdbSetString Si Sin Equation "ddt(Sin) - 2.0 * $Pi * $freq1 * Cos"
        pdbSetDouble Si Sin Abs.Error $err
        pdbSetString Si Cos Equation "ddt(Cos) + 2.0 * $Pi * $freq2 * Sin"
        pdbSetDouble Si Cos Abs.Error $err
        sel z=0.0 name=Sin
        sel z=1.0 name=Cos


set Win1 [CreateGraphWindow]
set Win3 [CreateGraphWindow]

set step 0.0
set t 0.0
######################################################
diffuse time=3E-9 temp=300 init=1.0e-15 movie = {

## Phase Determination
sel z=PA+PB name=PB0
```

```
sel z=PA2+PB2 name=PB1


## Artificial Time Step
        sel z=tt
        set tt [interpolate silicon x=0.0]
#       AddtoLine $Win tt $time $tt

## Differntial Time Spacing
        set CurrDt [expr $time - $t]
#       AddtoLine $Win dT $time $CurrDt
        set t $time

## Laser Intensity
        sel z=LI
        set LI [interpolate silicon x=0.0]
#       AddtoLine $Win LI $time $LI


## Laser Power Density
      sel z=(LPD/1e11+300)
        set LPD [interpolate silicon x=0.001]
        AddtoLine $Win1 LPD@10A $time $LPD

## Thermal Profile
        sel z=TT
        set TT [interpolate silicon x=0.0]
        AddtoLine $Win1 TT@0A $time $TT
        set TT [interpolate silicon x=0.001]
        AddtoLine $Win1 TT@10A $time $TT
      set TT [interpolate silicon x=0.01]
        AddtoLine $Win1 TT@100A $time $TT
      set TT [interpolate silicon x=0.1]
        AddtoLine $Win1 TT@1000A $time $TT
        sel z=T
        set T [interpolate silicon x=0.0]
        AddtoLine $Win1 T@0A $time $T
        sel z=HH
        set HH [interpolate silicon x=0.0]
        AddtoLine $Win1 HH@0A $time $HH


## Phase Profile
        sel z=PA
        set PA [interpolate silicon x=0.001]
        AddtoLine $Win3 PA@10A $time $PA
```

```
        set PA [interpolate silicon x=0.01]
        AddtoLine $Win3 PA@100A $time $PA
        set PA [interpolate silicon x=0.02]
        AddtoLine $Win3 PA@200A $time $PA
        sel z=MF
        set MF [interpolate silicon x=0.001]
        AddtoLine $Win3 MF@10A $time $MF


## Time Step Counter
set count [expr $step + 1]
set step $count


## Output File
    puts -nonewline $Ph $count
    puts -nonewline $Ph "  "
    puts -nonewline $Ph $TT
    puts -nonewline $Ph "  "
    sel z=TT
    puts -nonewline $Ph [print.1d]
    puts -nonewline $Ph "  "
    puts $Ph " "
    flush $Ph

 }
```

LIST OF REFERENCES

[1] Y. Taur, C. H. Wann, and D. J. Frank, "25 nm CMOS Design Considerations," *IEEE*, pp. 789-792, 1998.

[2] S. Thompson, P. Packan, and M. Bohr, "MOS Scaling: Transistors Challenges for the 21st Century," INTEL, Portland Q398, 1998.

[3] S.-D. Kim, C.-M. Park, and J. C. S. Woo, "Advanced Model and Analysis of Series Resistance on CMOS Scaling into Nanometer Regime--Part2: Qualitative Analysis," *IEEE Trans. Electron Devices*, vol. 49, pp. 467-472, 2002.

[4] G. E. Moore, "Cramming more Components onto Integrated Circuits," *Electronics*, vol. 38, 1965.

[5] ITRS, "International Technology Roadmap for Semiconductors," ITRS 2002 Update.

[6] R. Alväger and N. J. Hansen, *Rev. Scientific Instr.*, vol. 33, pp. 567, 1962.

[7] J. W. Mayer, L. Eriksson, and J. A. Davies, *Ion Implantation in Semiconductors*. New York: Academic Press, 1970.

[8] S. Talwar, Y. Wang, and C. Gelatos, "Laser Thermal Processing (LTP) for Fabrication of Ultra-shallow, Hyper-Abrupt, Highly Activated Junctions for Deca-nanameter MOS Transistors," presented at Electrochem. Soc. Symp. Proc., Toronto, Canada, 2000.

[9] C. Dachs, R. Surdeanu, B. J. Pawlak, B. Doornbos, R. D. A. Heringa, Y. Ponomarev, R. Lindsay, K. Henson, B. Dieu, L. Geenen, I. Hoflijk, O. Richard, T. Claysse, B. Brijs, and V. Vandervost, "CMOS Scaling Beyond the 90 nm CMOS Technology Node Shallow Junction and Integration Challenges," presented at USJ, 2003.

[10] B. Yu, Y. Wang, H. Wang, Q. Xiang, C. Riccobene, S. Talwar, and M.-R. Lin, "70nm MOSFET with Ultra-Shallow, Abrupt, and Super-Doped S/D Extensions Implemented by Laser Thermal Process (LTP)," *IEEE*, pp. 509-512, 1999.

[11] P. A. Packan, "Physical Modeling of Transient Diffusion Effects in Silicon Due to Surface Oxidation and Ion-implantation," Diss. Stanford University, 1991.

[12] J. M. Poate and J. S. Williams, *Ion Implantation and Beam Processing*. New York: Academic Press, 1984.

[13] R. S. Tichy, K. Elliott, S. McCoy, and D. C. Sing, "Annealing of Ultrashallow Implanted Junctions Arc-Lamp

Technology: Achieving the 90 nm Node," Internataional Sematech, Technology Transfer #01094165A-TR, December 21, 2001 2001.

[14] V. I. Kuznetsov, A. B. Storm, G. J. Snijders, C. D. Ridder, E. H. A. Granneman, T. A. M. Ruijl, and J. C. G. v. d. Sanden, "LEVITOR 4000: An Advanced RTP System Based on Conductive Heat Transfer," presented at 197th Meeting of Elect. Chem. Soc, Toronto, Ontario, Canada, 2000.

[15] S. Talwar, G. Verma, and K. H. Weiner, "Ultra-Shallow, Abrupt, and Highly-Activated Junctions by Low-Energy Ion Implantation and Laser Annealing," *IEEE*, pp. 1171-1174, 1999.

[16] S. Talwar, S. Felch, D. Downey, and Y. Wang, "Study of Laser Thermal Processing (LTP) to Meet Sub 130 nm Node Shallow Junction Requirements," *IEEE*, pp. 175-177, 2000.

[17] R. Surdeanu, Y. V. Ponomarev, R. Cerutti, B. J. Pawlak, L. K. Nanver, I. Hoflijk, P. A. Stolk, C. J. J. Dachs, M. A. Verheijen, M. Kaiser, M. J. P. Hopstaken, J. G. M. v. Berkum, F. Roozeboom, and R. Lindsay, "Laser Annealing for Ultra-Shallow Junction Formation in Advanced CMOS," presented at ECS, Philadelphia, 2002.

[18] D. V. Rao and G. L. Narasimha, *J. Appl. Phys.*, vol. 39, pp. 4853, 1968.

[19] E. I. Shtyrkov, I. B. Khaibullin, M. M. Zaripov, M. F. Galyatudinov, and R. M. Bayazitov, *Sov. Phys.-Semicond.*, vol. 9, pp. 1309, 1976.

[20] S. S. Lau, W. F. Tseng, M.-A. Nicolet, and J. W. Mayer, "Epitaxial Growth of Deposted Amorphous Layer by Laser Annealing," *Appl. Phys. Lett.*, vol. 33, pp. 130-131, 1978.

[21] J. C. Bean, H. J. Leamy, G. A. Rozgonyi, T. T. Sheng, J. S. Williams, and G. K. Celler, "Epitaxial Laser Crystallization of Thin-Film Amorhous Silicon," *Appl. Phys. Lett.*, vol. 33, pp. 227-230, 1978.

[22] M. Bohr, S. U. Ahmed, L. Brigham, R. Chau, R. Gasser, R. Green, W. Hargrove, E. Lee, R. Natter, S. Thompson, K. Weldon, and S. Yang, "High Performance 0.35 um Logic Technology for 3.3 V and 2.5 V Operation," *IEDM Technical Digest*, pp. 273, 1994.

[23] J. F. Ziegler, "Ion Implantation-Science and Technology." Edgewater, MD: Ion Implantation Technology Co., 2000, pp. 687.

[24] S. Talwar, G. Verma, K. Weiner, and C. Gelatos, "Laser Thermal Processing for Shallow Junction and Silicide Formation," presented at SPIE Conference on Microelectronic Device Technology II, Santa Clara, California, 1998.

[25] R. Murto, K. Jones, M. Rendon, and S. Talwar, "An Investigation of Species Dependence in Germanium Pre-amorphized and Laser Thermal Annealed Ultra-Shallow Abrupt Junctions," *IEEE*, pp. 182-185, 2000.

[26] S. Talwar, "GILD for Ultra Shallow Junction Formation in MOS Fabrication," Diss. Stanford University, 1995.

[27] M. O. Thompson, G. J. Galvin, J. W. Mayer, P. S. Percy, J. M. Poate, D. C. Jacobson, A. G. Cullis, and N. G. Chew, "Melting Temperature and Explosive Crystallization of Amorphous Silicon during Pulsed Laser Irradiation," *The American Physical Society*, vol. 52, pp. 2360-2363, 1984.

[28] H. Kodera, "Diffusion Coefficients of Impurities in Silicon Melt," *Jpn. J. Appl. Phys.*, vol. 2, pp. 212, 1963.

[29] A. G. Cullis, H. C. Webber, and N. G. Chew, "Correlation of the Structure and Electrical Properties of Ion-Implanted and Laser-Annealed Silicon," *Appl. Phys. Lett.*, vol. 36, pp. 547-550, 1980.

[30] P. L. Liu, R. Yen, N. Bloembergen, and R. T. Hodgson, "Picosecond Laser-induced Melting and Resolidification Morphology on Si," *Appl. Phys. Lett*, vol. 34, pp. 864, 1979.

[31] R. Tsu, R. T. Hodgson, T. Y. Tan, and J. E. Baglin, "Order-Disorder Transition in Single-Crystal Silicon Induced by Pulsed uv Laser Irradiation," *Phys. Rev. Lett.*, vol. 42, pp. 1356-1358, 1979.

[32] J. M. Poate, "High Speed Crystal Growth and Solidification using Laser Heating," *Journal of Crystal Growth*, vol. 79, pp. 549-561, 1986.

[33] M. O. Thompson and P. S. Peercy, "Anomalous Behaviour during the Solidification of Silicon in the Presence of Impurities," presented at Mat. Res. Symp. Proc., San Francisco, CA, 1985.

[34] R. F. Wood, "Modeling of Nonequilibrium Melting and Solidification in Laser-irrradiated Materials," *Physical Review B*, vol. 34, pp. 2606-2620, 1986.

[35] K. S. Jones, E. Kuryliw, R. Murto, M. Rendon, and S. Talwar, "Boron Diffusion upon Annealing of Laser Thermal Processed Silicon," *IEEE*, pp. 111-114, 2000.

[36] P. A. Packan and J. D. Plummer, "Transient Diffusion of Low-concentration B Due to ^{29}Si Implantation Damage," *Appl. Phys. Lett.*, vol. 56, pp. 1787-1789, 1990.

[37] H.-J. Gossmann, G. H. Gilmer, C. S. Rafferty, F. C. Unterwald, T. Boone, and J. M. Poate, "Determination of Si Self-interstitial Diffusivities for the Oxidation-enhanced Diffusion in B Doping-superlattices: The Influence of the Marker Layer," *J. Appl. Phys.*, vol. 77, pp. 1948-1951, 1995.

[38] A. Claverie, L. Laanab, C. Bonafos, and C. Bergaud, "On the Relation Between Dopant Anomalous Diffusion in Si and End-of-Range Defects," *Nuclear Instruments and Methods in Physics Research B*, vol. 96, pp. 202-209, 1995.

[39] Y. Takamura, P. B. Griffin, and J. D. Plummer, "Physical Processes Associated with the Deactivation of Dopants in Laser Annealed Silicon," *J. Appl. Phys.*, vol. 92, pp. 235-244, 2002.

[40] Y. Takamura, S. H. Jain, P. B. Griffin, and J. D. Plummer, "Thermal Stability of Dopants in Laser Annealed Silicon," *J. Appl. Phys.*, vol. 92, pp. 230-234, 2002.

[41] F. A. Trombore, "Solid Solubility of Impurity Elements in Germanium and Silicon," *Bell. Syst. Tech. J.*, vol. 39, pp. 205-233, 1960.

[42] C. W. White, S. R. Wilsion, B. R. Appleton, and J. F. W. Young, "Supersaturated Substitutional Alloys Formed by Ion Implantation and Pulsed Laser Annealing of Group-III and Group-V Dopants in Silicon," *J. Appl. Phys.*, vol. 51, pp. 738-749, 1980.

[43] S. M. Sze, *Physics of Semiconductor Devices*, 2nd ed. New York: Wiley, 1981.

[44] P. Ostoja, S. Solmi, and A. Zani, "Optical and Electrical Characterization of High-dose Ion Implanted, Laser-annealed Silicon Solar Cells," *Journal of Applied Physics*, vol. 52, pp. 6208-6213, 1981.

[45] A. Lietoila, J. F. Gibbons, and T. W. Sigmon, "The Solid Solubility and Thermal Behavior of Metastable Concentrations of As in Si," *Applied Physics Letters*, vol. 36, pp. 765-768, 1980.

[46] N. Natsuaki, M. Tamura, and T. Tokuyama, "Nonequilibrium Solid Solutions Obtained by Heavy Ion Implantation and Laser Annealing," *J. Appl. Phys.*, vol. 51, pp. 3373-3382, 1980.

[47] P. M. Rousseau, P. B. Griffin, W. T. Fang, and J. D. Plummer, "Arsenic Deactivation Enhanced Diffusion: A time, Temperature, and Concentration Study," *Journal of Applied Physics*, vol. 84, pp. 3593-3601, 1998.

[48] A. N. Larsen, F. T. Pedersen, G. Weyer, R. Galloni, R. Rizzoli, and A. Armigliato, "The nature of Electrically Inactive Antimony in Silicon," *Journal of Applied Physics*, vol. 59, pp. 1908-1917, 1986.

[49] W. Hume-Rothery, "Atomic Diameters, Atomic Volumes and Solid Solubility Relations in Alloys," *Acta Metallurgica*, vol. 14, pp. 17-20, 1966.

[50] B. C. Larson, C. W. White, and B. R. Appleton, "Unidirectional Contraction in Boron-implanted Laser-annealed Silicon," *Applied Physics Letters*, vol. 32, pp. 801-803, 1978.

[51] J. Sardela, M. R., H. H. Radamson, J. O. Ekberg, J.-E. Sundgren, and G. V. Hansson, "Growth, Electrical Properties and Reciprocal Lattice Mapping Characterization of Heavily B-doped, Highly Strained Silicon-molecular Beam Epitaxial Structures," *Journal of Crystal Growth*, vol. 143, pp. 184-193, 1994.

[52] H.-J. Herzog, L. Csepregi, and H. Seidel, "X-Ray Investigation of Boron- and Germanium-Doped Silicon Epitaxial Layers," *J. Electrochem. Soc.*, vol. 116, pp. 2969, 1984.

[53] H. Hirayama, T. Tatsumi, and N. Aizaki, "Stress Reduction and Doping Efficiency in B- and Ge-doped Silicon Molecular Beam Epitaxy Films," *Appl. Phys. Let.*, vol. 52, pp. 1335-1337, 1988.

[54] A. Ferreiro, A. M. Papon, and B. Biasse, "Strain Compensation Effects on the Annealing of Ge+ -B+ -implanted Silicon," *Materials Science and Engineering*, vol. B4, pp. 217-222, 1989.

[55] W. P. Maszara and T. Thompson, "Strain Compensation by Ge in B-doped Silicon Epitaxial Films," *Journal of Applied Physics*, vol. 72, pp. 4477-4479, 1992.

[56] B. Tillack, P. Zaumseil, G. Morgenstern, D. Kruger, B. Dietrich, and G. Ritter, "Strain Compensation in Ternary Si(1-x-y)Ge(x)B(y) Films," *J. of Crystal Growth*, vol. 157, pp. 181-184, 1995.

[57] A. Rodriguez, T. Rodriguez, A. Kling, J. C. Soares, M. F. d. Silva, and C. Ballesteros, "Determination of the Strain Depth Profile in Solid-Phase Epitaxially Grown SiGe Layers using RBS/Channeling," *Nucl. Instrum. Methods B*, vol. 136-138, pp. 395-399, 1998.

[58] K. A. Gable, L. S. Robertson, K. S. Jones, and M. E. Law, "Strain Compensation for Boron Ultra-Shallow Juntion Formation Following Laser Theramal Processing of Ion Implanted Silicon," presented at Ultra Shallow Junctions, Santa Cruz, CA USA, 2003.

[59] R. F. Wood and J. F. W. Young, "Semiconductors and Semimetals," vol. 23, 1984, pp. 283.

[60] R. Murto, K. Jones, M. Rendon, and S. Talwar, "Activation and Deactivation Studies of Laser Thermal Annealed Boron, Arsenic, Phosphorus, and Antimony Ultra-Shallow Abrupt Junctions," *IEEE*, pp. 155-158, 2000.

[61] E. A. Kuryliw, "Analyzing the Thermal Annealing Behavior of Laser Thermal Processed Silicon," in *Materials Science and Engineering*. Gainesville: University of Florida, 2003, pp. 160.

[62] K. A. Gable, L. S. Robertson, K. S. Jones, and M. E. Law, "Strain Compensation for Boron Ultra-shallow Junction Formation Following Laser Thermal Processing of Ion Implanted Silicon," presented at Ultra Shallow Junctions, Santa Cruz, 2003.

[63] S. Earles, M. Law, R. Brindos, K. Jones, S. Talwar, and S. Corcoran, *IEEE Tran. On Elec.*, vol. 49, pp. 1118, 2002.

[64] A. G. Cullis, H. C. Webber, and P. Bailey, "A Device for Laser Beam Diffusion and Homogenisation," *J. Phys. E: Sci. Instrum.*, vol. 12, pp. 688-689, 1979.

[65] *Encyclopedia of Materials Characterization*. Boston: Butterworth-Heinemann, 1992.

[66] L. G. Valdes, presented at I. R. E., 1954.

[67] M. A. Logan, *Bell Sys. Tech. J.*, vol. 46, pp. 2277, 1967.

[68] P. Smith and D. Hoglund, "Simulation of One-dimensional Heat Flow During Pulsed Laser Melting of Thin Films," 4.01 ed, 1999.

[69] *Handbook of Optical Constants of Solids*. New York: Academic Press, 1985.

[70] J. C. Bean, H. J. Leamy, J. M. Poate, G. A. Rozgoni, J. P. v. d. Ziel, and J. S. Williams, "Substrate and Doping Effects upon Laser-Induced Epitaxy of Amorphous Silicon," *J. Appl. Phys.*, vol. 50, pp. 881-885, 1979.

[71] H. B. Banisaukas, "Residual Damage from Laser Thermal Processing of Ion Implanted Silicon," in *Materials Science and Engineering*. Gainesville: University of Florida, 2000, pp. 120.

[72] K. A. Gable, K. S. Jones, M. E. Law, L. S. Robertson, and S. Talwar, "Electrical and Structural Characterization of Boron Implanted Silicon Following Laser Thermal Processing," presented at MRS Fall Meeting, Symposium C, 2002.

[73] R. E. Hummel, *Electronic Properties of Materials*, 2 ed. New York: Springer, 1985.

[74] *Binary Alloy Phase Diagrams Second Edition*: W. W. Scott Jr., 1990.

[75] F. N. Rhines, *Phase Diagrams in Metallurgy*. New York: McGraw-Hill, 1956.

[76] R. E. Hummel, "Differential Reflectance Spectroscopy in Analysis of Surfaces," in *Enchyclopedia of Analytical Chemistry*, R. A. Meyers, Ed. Chichester: John Wiley & Sons Ltd, 2000, pp. 9047-9071.

[77] R. Jones, S. Oberg, F. B. Rasmussen, and B. B. Nielson, "Identification of the Dominant Nitrogen Defect in Silicon," *Physical Review Letters*, vol. 72, pp. 1882-1885, 1994.

[78] F. B. Rassmussen and B. B. Nielsen, "Microstructure of the Nitrogen Pair in Crystalline Silicon Studied by Ion Channeling," *The American Physical Society*, vol. 49, pp. 16353-16360, 1994.

[79] G. Verma, S. Talwar, and J. C. Bravman, "Creating Process Margin in Laser Thermal Processing: Application to Formation of Titanium Silicide," *Appl. Phys. Lett.*, vol. 78, pp. 925-927, 2001.

[80] S. Yang and M. O. Thompson, "Laser Thermal Induced Crystallization for 20 nm Device Structures," presented at Mat. Res. Soc. Symp. Proc., 2001.

[81] J. J. P. Bruines, R. P. M. v. Hal, B. H. Koek, M. P. A. Viegers, and H. M. J. Boots, "The Transient Between Amorhpous Regrowth and Explosive Crystallization," presented at Mat. Res. Soc. Symp. Proc., 1987.

[82] S. U. Campisano, P. Baeri, M. G. Grimaldi, G. Foti, and E. Rimini, "Surface Accumulation of Te Atoms in Laser Melted Te-Implanted Silicon," *J. Appl. Phys.*, vol. 51, pp. 3968-3970, 1980.

[83] P. Baeri, J. M. Poate, S. U. Campisano, G. Foti, E. Rimini, and A. G. Cullis, "Dependence of Trapping and Segregation of Indium in Silicon on the Velocity of the Liquid-Solid Interface," *Appl. Phys. Lett.*, vol. 37, pp. 912-914, 1981.

[84] P. Baeri, B. Foti, J. M. Poate, S. U. Campisano, and A. G. Cullis, "Orientation and Velocity Dependance of Solute Trapping in Si," *Appl. Phys. Lett.*, vol. 38, pp. 800-802, 1981.

[85] P. A. Stolk, H.-J. Gossman, D. J. Eaglesham, D. C. Jacobson, C. S. Rafferty, G. H. Gilmer, M. Jaraiz, J. M. Poate, H. S. Luftman, and T. E. Haynes, "Physical Mechanisms of Transient Enhanced Dopant Diffusion In Ion-Implanted Silicon," *J. Appl. Phys.*, vol. 81, pp. 6031-6050, 1997.

[86] S. C. Jain, P. A. Stolk, S. Decoutere, M. Willander, and H. E. Maes, "Transient Enhanced Diffusion of Boron in Si," *J. Appl. Phys*, vol. 91, pp. 8919-8941, 2002.

[87] J. D. Plummer, M. D. Deal, and P. B. Griffin, *Silicon VLSI Technology*. Upper Saddle River, New Jersey: Prentice Hall, Inc., 2000.

[88] J. M. Jacques, L. S. Robertson, K. S. Jones, M. E. Law, M. Rendon, and J. Bennett, "Fluorine-enhanced boron diffusion in amorphous silicon," *Applied Physics Letters*, vol. 82, pp. 3469-3471, 2003.

[89] X. Lu and N. W. Cheung, "Synthesis of SiGe and SiGeC Alloys Formed by Ge and C Implantation," *Appl. Phys. Lett*, vol. 69, pp. 1915, 1996.

[90] G. S. Kar, A. Dhar, L. K. Bera, S. K. Ray, S. John, and S. K. Banerjee, "Effect of Carbon on Lattice Strain and Hole Mobility in Si(1-x)Ge(x) Alloys," *J. Mat. Sci.*, vol. 13, pp. 49-55, 2002.

[91] B. G. Cohen, "X-ray Measurement of Elastic Strain and Lattice Constant of Diffused Silicon," *Solid State Electron.*, vol. 10, pp. 33, 1967.

[92] W. D. Truner, D. C. Elrod, and I. I. Siman-Tov, Oak Ridge National Laboratory, Oak Ridge ORNL/CSD/TM-15, 1977.

[93] R. F. Wood, C. W. White, and R. T. Young, "Pulsed Laser Processing of Semiconductors," in *Semiconductors and semimetals*, vol. 23, R. K. Willardson and A. C. Beer, Eds. Orlando: Academic Press, Inc., 1984, pp. 693.

[94] L. A. Lompre, J. M. Liu, H. Kurz, and N. Bloembergen, "Time-Resolved Temperatue Measurement of Picosecond Laser Irradiated Silicon," *Appl. Phys. Lett.*, vol. 43, pp. 168-170, 1983.

[95] G. A. Geist and R. F. Wood, "Modeling of Complex Melting and Soldification Behavior in Laser-irradiated Materials," Oak Ridge National Laboratory, Oak Ridge ORNL-6242, 1985.

[96] R. P. Raman, "Effect of End-of-Range Dislocation Loop Depth on the Evolution of {311} Defects and Loops," in *Electrical and Computer Engineering*. Gainesville: University of Florida, 1998, pp. 74.

BIOGRAPHICAL SKETCH

Mark Harold Clark was born on April 8, 1973, in Rigby, Idaho. He received his B.S. in metallurgical engineering in 1998 at the University of Idaho. In 2001, he received his M.S. degree in materials science and engineering at the University of Florida. During the summer of 2002, he interned at Matrix Semiconductor where he worked in process development, contributing to the fabrication of a three-dimensional memory matrix. Subsequently, he interned eight months with Philips Semiconductor studying ultra-shallow, highly-doped, hyper-abrupt source/drain extensions formed by laser thermal annealing. His current research interest is focused on medical application of materials.